

UC Berkeley

UC Berkeley Electronic Theses and Dissertations

Title

Scalable nanomanufacturing of semiconducting van der Waals monolayers

Permalink

<https://escholarship.org/uc/item/8899c0x0>

Author

Gramling, Hannah

Publication Date

2019

Peer reviewed|Thesis/dissertation

Scalable nanomanufacturing of semiconducting van der Waals monolayers

by

Hannah Marie Gramling

A dissertation submitted in partial satisfaction of the
requirements for the degree of
Doctor of Philosophy

in

Engineering-Mechanical Engineering

in the

Graduate Division
of the
University of California, Berkeley

Committee in charge:

Professor Hayden Taylor, Chair
Professor Daryl Chrzan
Professor Liwei Lin

Spring 2019

Scalable nanomanufacturing of semiconducting van der Waals monolayers

Copyright 2019
by
Hannah Marie Gramling

Abstract

Scalable nanomanufacturing of semiconducting van der Waals monolayers

by

Hannah Marie Gramling

Doctor of Philosophy in Engineering-Mechanical Engineering

University of California, Berkeley

Professor Hayden Taylor, Chair

Van der Waals solids are a class of materials made up of loosely-bound, molecularly-thin layers. These layers can be readily detached from one another due to their weak interlayer van der Waals bonds, giving the materials their name. In 2004, the isolation of graphene, a single-atom-thick layer of carbon, from graphite, a bulk van der Waals material, prompted a surge of research interest in the nearly two-dimensional layers making up these materials. Their mechanical strength, stability in ambient conditions, flexibility, and near-transparency are intriguing for the production of flexible electronics. Meanwhile, their ultimate thinness opens an avenue for exploring extreme physics, offering the possibility of new kinds of devices, and making these materials intriguing to researchers in the short term. Graphene, the most famous, is a conductor. However, some van der Waals materials are semiconductors, which are necessary to produce electronic switches and light-emitting diodes (LEDs), while other van der Waals materials are insulators. There is considerable potential in combining these different van der Waals materials to produce so-called heterostructures, which can re-create existing functionality, such as light emission, or produce new devices with unique capabilities.

The difficulty of manipulating atomically-thin semiconductors has prevented them from achieving commercial application. Existing processes for manipulating van der Waals semiconductors do not offer control over the shape or size of the single-layer features produced.

By interrogating the role of stamp mechanics in the success of producing single layers, this thesis develops a method that enables the creation of van der Waals heterostructure arrays. After an introduction to the current state of the art in scalable manufacture of van der Waals monolayers and its tradeoffs in Chapter 1, Chapter 2 demonstrates a new process for creating patterned arrays of semiconducting monolayers from a bulk source. In order to measure the effectiveness of the method, this work introduces yield metrics relevant to nanomanufacturing of 2D material patterns. To further understand the role of the stamp in the process of exfoliation, Chapter 3 presents a finite element model bridging macroscale and nanoscale physics to understand the interaction between van der Waals layers and an elastic stamp. The results from this model carry implications for nanomanufacturing process design.

Chapter 4 then concludes with discussion of the usefulness and limitations of the methods developed in this work, and considers future directions that will enable high-yield mass production of van der Waals heterostructures.

For Ben and Daniel.

Contents

List of Figures	iv
List of Tables	xi
1 Mechanical approaches to nanomanufacturing of van der Waals monolayer arrays	1
1.1 Background	3
1.2 Processing challenges	5
1.2.1 Transfer methods	5
1.2.2 Monolayer isolation	10
1.3 Leveraging mechanical phenomena	21
1.4 Analysis and conclusions	27
1.4.1 Paradigms in two-dimensional material production	27
1.4.2 The need to augment mechanical understanding	28
1.4.3 Final remarks	29
2 Producing arrays of semiconducting van der Waals monolayers from bulk	31
2.1 Introduction	32
2.2 Handle design	33
2.2.1 Analytical derivation of handle height	34
2.2.2 Contact mechanics confirmation	37
2.2.3 Mechanical properties of thermal release tape	39
2.2.4 Mechanical properties of photoresist	39
2.3 Methods	41
2.3.1 Photolithography	41
2.3.2 Process flow	42
2.3.3 Device fabrication	44
2.4 Results	44
2.4.1 Optical and optoelectronic characterization	44
2.4.2 Electrical characterization	53
2.4.3 Yield characterization	54

2.4.4	Atomic force microscopy	61
2.4.5	X-ray photoelectron spectroscopy (XPS) characterization	62
2.4.6	Confirmation of heterostructure fabrication compatibility	62
2.4.7	Theory of metal film assisted exfoliation	66
2.5	Conclusions	68
3	Finite element modeling of van der Waals layers in contact with an elastic stamp	70
3.1	Introduction	71
3.2	Methods	72
3.2.1	Previous approaches to van der Waals finite element modeling	72
3.2.2	Assumptions	76
3.2.3	Defining interlayer interactions	78
3.2.4	Interlayer interaction derivation	79
3.2.5	Model definition in Abaqus	84
3.2.6	Validation with molecular dynamics	92
3.3	Results	93
3.3.1	Displacement of layers as a function of stamp modulus	93
3.3.2	Displacement of layers as a function of interfeature spacing	94
3.4	Conclusions	95
4	Conclusions and Future Work	99
4.1	Contributions of this work	100
4.2	Future directions	100
4.2.1	Future fabrication of van der Waals monolayer arrays	100
4.2.2	Further study of van der Waals material-stamp mechanics	102
	Bibliography	103
A	Derivation of van der Waals body force	116

List of Figures

1.1	Possible routes to achieving patterned, precisely-layered (including monolayer) two-dimensional material arrays on a target substrate, a prerequisite of mass heterostructure device fabrication. Process flows that will not interfere with existing material on a target substrate, and are thus compatible with heterostructure fabrication, use a dashed blue arrow.	6
1.2	A comparison of size scales demonstrated with exfoliation methods on multilayer MoS ₂ and graphene, illustrating the inability to achieve large-area, patterned monolayers. Refs. [1, 2, 3, 4, 5, 6, 7, 8, 9, 10, 11, 12, 13].	12
1.3	Biasing of stamp/substrate for electrostatically assisted exfoliation (Liang <i>et al.</i> 2008 [3]).	15
1.4	Roller style exfoliation (Liang <i>et al.</i> 2010 [2]).	17
1.5	Nanoimprint-assisted shear exfoliation (NASE) of MoS ₂ (Chen <i>et al.</i> 2015 [8]).	18
1.6	a) Typical exfoliated monolayer MoS ₂ (Radisavljevic <i>et al.</i> 2011 [14], scale bar length added). b) Most uniform reported result of (non-monolayer) MoS ₂ produced by nano-imprint shear exfoliation (NASE) (Chen <i>et al.</i> 2015 [8]). c) Monolayer MoS ₂ produced using the gold-assisted exfoliation method of Magda and co-authors [9]. d) Monolayer MoS ₂ produced using the gold-assisted exfoliation method of Desai and co-authors [11].	22
1.7	a) Paper, and b) graphene kirigami structure, unstretched, and c) stretched. Scale bars 10 μm (adapted from Blees <i>et al.</i> 2015 [15]).	24
1.8	Solvent driven conformity of two-dimensional materials onto textured substrate (Choi <i>et al.</i> 2015 [16]).	26
2.1	When a pressure-sensitive adhesive is brought into conformal contact with a patterned array of features in a van der Waals material, the depth of these features is important. If the features are shallow, the pressure applied to the adhesive will allow it to deform into contact with unpatterned regions, to which it will then adhere.	34

2.2	Attempts to create microns-deep trenches in bulk MoS ₂ . a) A CF ₄ etch, one of six etch chemistries applied, damages the material to create non-planar sidewalls before a sufficient etch depth is achieved. b) A nanosecond pulsed laser creates deep trenches, but oxidizes the material at the sidewalls, binding the layers together. c) Focused ion beam milling achieves an etch rate below 1 μm per hour.	35
2.3	Dimensions of the photoresist handle layer are designed to prevent unwanted adhesive contact outside the handles. Dimensions of the handle layer pattern (grey), which could be create using photoresist, and of the transfer medium (thermal release tape), in green, are shown. For a given far-field applied stress σ_{∞} , and adhesive layer material properties, a certain minimum height h is needed to prevent unwanted, direct contact between the transfer medium and the unmasked vdW-bonded, layered material.	37
2.4	Expected stamp deflection under the minimum applied load, calculated by prescribing a stamp deflection and reverse-engineering the pressure needed to cause this deflection using the deformation kernel of stamp (derived from ref. [17]). (a) Stamp deformation profile as a function of lateral position, resulting from the contact regions prescribed, (b) the prescribed locations where contact is made, either between the stamp and the photoresist handles or between the stamp and the layered material's surface, (c) the pressure in the stamp at each location, resulting in an average back pressure of 297 kPa.	40
2.5	The process for producing patterned van der Waals monolayers. The process uses standard photolithography techniques. It relies on the use of a thick handle layer (here, photoresist, in step 2) to pattern the gold and the underlying layered bulk material, as well as to offset the adhesive transfer medium from the bulk, thus permitting transfer of only the patterned regions.	45
2.6	(a) Cross-section and optical micrograph of six fabricated back-gated MoS ₂ transistors with channel width up to 40 μm, defined by the patterning process, and a gate length of 10 μm defined by the Ni contacts. (b) Switching behavior of one of the devices fabricated from transferred monolayer MoS ₂ material. (c) Drain current as a function of drain-source bias, measured at eight gate-source biases, up to 60 V, on a single 10 μm gate length monolayer MoS ₂ transistor. The device did not enter saturation mode at any gate-source bias tested. These curves are representative of all transistors measured, using both MoS ₂ and WS ₂ as channel materials; all exhibited only linear behavior.	46

2.7	Optical and optoelectronic WS ₂ monolayer characterization. (a) White-light reflectance image of a set of transferred WS ₂ features on 260 nm thermal SiO ₂ on Si; (b) photoluminescence image of part of the same region as in (a): orientation is the same as (a), and the outline corresponds to that of the region imaged in (a); (c) photoluminescence spectra from 13 regions of WS ₂ on 260 nm thermal SiO ₂ on Si, confirming that monolayer WS ₂ has been transferred to the substrate; (d) the result of treating a WS ₂ monolayer with a superacid, showing more than a twenty five-fold increase in quantum efficiency.	47
2.8	Optical and optoelectronic MoS ₂ monolayer characterization. (a) White-light reflectance image of a set of transferred MoS ₂ features on 260 nm thermal SiO ₂ on Si; (b) photoluminescence image of the region; (c) photoluminescence spectra associated with the numbered locations in (a), confirming that monolayer MoS ₂ has been transferred to the substrate; (d) the results of treating MoS ₂ monolayers with a superacid, showing more than a one hundred-fold increase in quantum efficiency.	48
2.9	(a) Raman map of the E _{2g} and A _{1g} peak separation, indicative of material thickness, over a monolayer chevron of transferred MoS ₂ . (b) Optical image of the region measured in (a). (c) Spectra from two different regions, <i>a</i> and <i>b</i> , labeled in the map, showing two inter-peak differences below the expected bilayer peak difference of 22 cm ⁻¹ . (d) Optical image of the feature mapped with Raman spectroscopy in (a), with points labeled whose photoluminescence spectra were measured. (e) Unnormalized photoluminescence spectra from the three points labeled in (d).	51
2.10	(a) Raman map of the E _{2g} and A _{1g} peak separation, indicative of material thickness, over two monolayer chevrons of transferred WS ₂ . The extent of the map scale is the same as in Figure 2.9. (b) Optical image of the region measured in (a). (c) Spectra from three different regions, <i>a</i> , <i>b</i> , and <i>c</i> , labeled in the map, showing inter-peak differences below the expected bilayer peak difference of 64 cm ⁻¹ . (d) Photoluminescence image (left) and optical image (right) of the same features mapped with Raman spectroscopy in (a). The readily observed luminescence across both features indicates their monolayer composition. (e) Unnormalized photoluminescence spectra from the three points labeled in (d), showing the consistent luminescence across the features.	52
2.11	Switching characteristics of back-gated MoS ₂ devices fabricated on two separate chips, using transferred monolayer MoS ₂ channels from two separate initial mined MoS ₂ sources. Chip 1 and Chip 2 are from different sources of material; five devices were measured on Chip 1 and 15 devices on Chip 2. All devices demonstrate an on/off current ratio > 10 ³ , with some devices achieving a ratio as high as 10 ⁷	55

2.12	Switching characteristics of six back-gated WS ₂ devices fabricated from monolayer WS ₂ , transferred from a synthetic bulk source. With a source/drain bias of 1V, some devices demonstrated on/off current ratios > 10 ⁴	56
2.13	Two approaches to yield characterization of transferred monolayer material. Feature yield (left) tabulates the binary appearance of monolayer material within the bounds of expected transferred features in the pattern. This metric is dependent on aspects of the transfer process, like applied exfoliation pressure, exfoliation peel rate, adhesion of the feature to the substrate (substrate pre-processing and transfer pressure and temperature), and forces applied during post-processing, including liquid processing for photoresist and gold removal. Area yield (right) tabulates the mean area of contiguous monolayer material within a transferred feature, as a percentage of the total area of the intended feature, among features including monolayer material. This metric captures aspects of the initial flake quality and the number of exposed layers.	58
2.14	Yield results of the exfoliation method. Histograms (blue bars) showing the distributions of the areas of regions of continuous monolayer material transferred to three separate substrates patterned with WS ₂ (a–c) and three substrates patterned with MoS ₂ (d–f). Samples were all created using the process flow of Figure 2.5, with the exfoliated material being the only variable. The red dashed line indicates the area that would be occupied in a pattern by a full, perfect feature; the yellow dashed line shows the average area of continuous material obtained from many samples using the prior, unpatterned, gold-mediated ‘CoBEx’ method [11].	60
2.15	(a) White light optical image of the MoS ₂ monolayer region measured with atomic force microscopy; (b) topographical map measured by atomic force microscopy in tapping mode, with an averaged trace shown below indicating a ~6 Å step height between the substrate and the transferred monolayer; (c) AFM phase lag map and (d) friction map of the same region.	63
2.16	(a) White light optical image of the WS ₂ monolayer region measured with atomic force microscopy; (b) topographical map measured by atomic force microscopy in tapping mode, with an averaged trace shown below indicating a ~6 Å step height between the substrate and the transferred monolayer; (c) AFM phase lag map and (d) friction map of the same region.	64
2.17	(a) XPS characterization of residual particles on WS ₂ , indicating the presence of expected substrate elements (Si, O), TMDC elements (W, S), and calibration elements (C). The remaining identified element is Au, which may comprise the residual particles. (b) AFM topography map of the particles. The height of the region in the white dashed box is plotted in the accompanying line-scan, showing that the particles are ~50 nm wide and ~5 nm tall.	65

2.18	(a) Raman map of two crossed MoS ₂ monolayer features, whose overlap forms a fabricated MoS ₂ bilayer. The inter-peak difference is consistent with monolayer MoS ₂ , except in the region where a natural bilayer is present, highlighted in (b). (c) Spectra from several points on the Raman map, indicating both monolayer and bilayer material are present. (d) Raman map of two overlapped MoS ₂ monolayers, creating a fabricated bilayer, after a brief annealing step. The overlapping region now behaves as an MoS ₂ bilayer, as indicated by the increased E _{2g} -A _{1g} peak difference (in cm ⁻¹). (e) The region mapped in (d). (f) Spectra from identified points of the region mapped in (d).	67
3.1	Two interacting layers of MoS ₂ . Each layer consists of two chalcogen sublayers (sulfur atoms) and one transition metal sublayer (molybdenum atoms). The interlayer distance D used throughout this chapter is $D_{S_2-S_1}$, the distance between the nearest sublayers of sulfur atoms in adjacent layers. . . .	75
3.2	The traction produced as a result of the interlayer interaction is the sum of the tractions produced by atoms in the adjacent layer, at interlayer distance D , whose individual contributions can be determined by summing the contributions from atoms within an annulus of increasing radius x and infinitesimal width dx	80
3.3	The differences in interlayer distance as the number of interlayer interactions considered, in a model which minimizes the sum of S-S, Mo-S, and Mo-Mo interaction energies as flat van der Waals layers move apart. The orange bars show the interlayer distances in the case where all fifteen interlayer interactions are considered (complete case). Two limited cases are calculated: (1) one in which only the five nearest-neighbor layer interactions considered (green bars), and (2) one in which both first- and second-nearest-neighbor layer interactions are considered, for a total of nine interactions (blue bars). Case (2) shows an order of magnitude closer match to the complete case, relative to case (1), even when the layers experience a 1 GPa load and undergo displacement.	81
3.4	The force on an edge region is decomposed into two contributions: one from the semi-infinite radius of atoms towards the center of the layer, shown in blue, and one from the finite radius R of atoms from the region to the boundary of the layer, shown in orange.	83
3.5	(a) The van der Waals potential energy between two sulfur atoms as a function of their distance, as described by a Lennard-Jones (LJ) potential. (b) The interlayer force per unit area as a function of the interlayer distance between two MoS ₂ layers, left axis, and the van der Waals force between two sulfur atoms as a function of their distance, right axis.	87

3.6	(a) The changing pressure that an edge region experiences as it interacts with an increasing radius of atoms in the adjacent layer. The different lines correspond to different interlayer displacements, starting from the equilibrium separation of 6.1 Å Mo-Mo = 2.9 Å S-S. Negative pressures are repulsive, while positive forces are attractive. (b) The same data shown in (a), here shown as a percentage of the pressure that a non-edge atom, interacting with a radius of atoms of $R = \infty$, experiences. In all cases, the force on an edge interacting with a circle of atoms of radius $R = 2.02$ nm has achieved 99.99% of the force on a central atom. Note that at interlayer S-S displacements of equilibrium + 0.3 Å and equilibrium + 0.4 Å, the directionality of the pressure switches from repulsive to attractive as additional atoms are considered.	88
3.7	Meshes on the van der Waals layer (top) and the underside of the stamp (bottom). The mesh density is increased at the edge of the van der Waals layer so that rapidly varying forces may be resolved over the short (~2 nm) region which may be considered the edge. The mesh on the stamp mimics the mesh on the layer in this region to prevent warping—the top van der Waals layer is tied to the stamp.	89
3.8	Interlayer interactions included in the model. Between a given pair of superlayers, all four chalcogen sublayer interactions are considered (left). Each superlayer interacts with up to four other layers, two above and two below, depending on the position of the layer (right). The top superlayer, for instance, only interacts with the two layers below it.	90
3.9	Dimensions and boundary conditions of the model. Individual subsections of the model are tiled (a) to mimic periodic strips of multilayer van der Waals stacks. The tiling is achieved by prescribing boundary conditions (b) that ensure continuity at the edges of the model. Further, the bottom van der Waals layer is fixed in its initial position, as a mounted piece of bulk material would be in experimental conditions. The top van der Waals layer is fixed to the stamp (in other words, perfect adhesion is assumed).	91
3.10	Exfoliation interface selectivity as a function of the Young's modulus of the stamp. In each case, the top layer/second layer interface had the largest interlayer distance, at the edge of the layer. The selectivity, then, is the difference between this (largest) interlayer distance, and the interlayer distance of the second-largest layer-layer gap. In all case, this second-largest gap occurred between the second-to-bottom and bottom van der Waals layers. Across all interfeature spacings, a softer stamp offers the greatest selectivity and is thus preferable.	96
3.11	Exfoliation interface selectivity as a function of the lateral spacing between features in the van der Waals layers. The variation in selectivity is clearly miniscule for both 100 kPa and 1 MPa modulus stamps (blue and yellow lines), though larger interfeature spacings offer slightly more selectivity.	97

3.12 Van der Waals interlayer distances, when the top of the stamp is displaced 5 nm, as a function of both the spacing between features and the modulus of the stamp, plotted on both (a) absolute and (b) relative scales. The discrepancy in center interlayer distances is negligible. In all cases, the top layer/second layer interface experiences the largest interlayer distance, and the bottom layer/second-to-bottom layer interface experiences the second-largest displacement.	98
---	----

List of Tables

1.1	Comparison of top-down and bottom-up sources of monolayer van der Waals sheets.	11
2.1	Values used for the inputs to Eqn. 2.1, used to calculate the necessary offset height to prevent roof collapse of the stamp.	38
2.2	Photoresist spin parameters to achieve a 15 $\mu\text{m}+$ thickness, photo-patternable layer using AZ P4620.	42
2.3	Raman characteristics of mono- and bilayer MoS_2 and WS_2 , from ref. [18]. All entries in units of cm^{-1} unless noted otherwise.	50
2.4	Feature and areal yield calculations for eight representative MoS_2 and three WS_2 substrates, processed using the technique detailed in Figure 2.5. These substrates include those described by the histograms in Figure 2.14; where applicable, the corresponding histogram label in Figure 2.14 is given in the rightmost column of this table.	59
3.1	Lennard-Jones parameters for interatomic interactions in MoS_2	76
3.2	Initial forces and stiffnesses between two nearest-neighbor MoS_2 molecules in adjacent layers. Positive forces are attractive, while negative forces are repulsive. Atom layer labels are shown in Figure 3.1. Stacking order is considered. Of note, the values listed are interatomic forces for select atoms, not interlayer forces, and thus do not sum to zero. For instance, the S_2 - S_1 force appears disproportionately large compared to the positive forces; considering a given S_2 atom, only the interaction with its nearest S_1 atoms will be negative, whereas the contributions from additional S_1 atoms will be attractive, as they are further away.	77
3.3	Within-layer elastic constants used for shell elements of MoS_2 , originally reported in N/m , from ref. [19]. Values were converted to GPa using a single-layer thickness value of 6.1 \AA , and ultimately implemented in units of $\text{J}/\mu\text{m}^3$. All unlisted constants are zero.	77
3.4	Dimensions of the model components.	85
3.5	Parameters tested. Each combination of modulus and interfeature spacing was modeled.	95

Acknowledgments

The work in this thesis was supported by a National Science Foundation Graduate Research Fellowship under Grant DGE 1106400, as well as National Science Foundation Award 1636256: SNM: Scalable Nanomanufacturing of 2D Electronic Materials and Devices Using Automated Exfoliation. The modeling work presented in Chapter 3 was supported by an International Consortium on Nanotechnologies studentship.

I would like to acknowledge a number of people who contributed to the scholarly success of the work presented in this thesis. I gratefully acknowledge my academic advisor, Hayden Taylor, for his guidance throughout. Professor Taylor held us to a high scientific standard, and was a constant model of the healthy skepticism needed to part the canopy of received wisdom and find sunlight for new approaches. This work was risky and slow-going; Professor Taylor's conviction that it was worthwhile enabled its eventual success.

I am thankful to Eric Yeatman for his collaboration and encouragement. Throughout my graduate work, Professor Yeatman was a generous teacher, and as a collaborator, he was at once enthusiastic and patient. I feel privileged to have had such a knowledgeable sounding board.

Fellow attendees of weekly Nanomeetings were the source of numerous helpful conversations, plentiful feedback, and continual encouragement. Thanks in particular to Daryl Chrzan, Joel Ager, Clarissa Towle, and Haoye Sun.

The instruction I received from Sujay Desai was invaluable in learning the processes and techniques for working with 2D materials. Without him, this research would have taken far longer and been considerably less successful.

I enjoyed the support of my fellow members of the Design for Nanomanufacturing group and was lucky to work with several talented undergraduates: thank you to Amrita Srinivasan, Wing Tak Fung, Gradey Wang, Evan Cole Lewis, and Yunsu Park.

It was a joy to have a desk between Brett Kelly and Hossein Heidari, both of whom are hardworking researchers, deeply kind humans, and constant sources of positivity.

The baristas at Peet's Qualcomm Cafe had my order memorized from 2014-2017. They reckoned this deserved a line in my dissertation. I agree.

I have spent these years in the company of a formidable collection of humans. Thank you to the confidantes, fellow grad students, roommates, and climbing partners who saw me through grad school. I look forward to finding better ways to thank you than a bit of text.

I tried for a long time to find the words to thank Nolan McPeck, Amrita Srinivasan, and Daniel Gramling for what they have done and continue to do for me. While I've failed on that count, it's easy enough to point out that their sharp wits and their thoughtfulness have become altogether indispensable to me.

Of the countless good fortunes I've had, the greatest has always been my family. I am buoyed, constantly, by their love and their friendship.

Chapter 1

**Mechanical approaches to
nanomanufacturing of van der Waals
monolayer arrays**

Since the isolation of single-atomic-layer graphite, or graphene, in 2004 [20], a vast research enterprise has developed around graphene and its fellow two-dimensional van der Waals materials. These van der Waals materials are composed of molecularly-thin layers, covalently bonded in the plane, and held together by van der Waals bonds. Because the covalent in-plane bonds are much stronger than the interlayer van der Waals bonds, the layers can be peeled apart with relative ease. Once the layers have been isolated, as a single layer (monolayer) or a few layers, they display interesting and novel properties. Not only are they flexible and nearly transparent; semiconducting van der Waals materials, including transition metal dichalcogenides like molybdenum disulfide, possess a direct band gap only in their monolayer form [21].

However, despite it being nearly a decade and a half since the initial isolation of so-called two-dimensional materials, only graphene has found its way into a commercialized mass-manufacturing process, geared towards flexible electronics. Moreover, the vast majority of devices published in the extensive two-dimensional materials research space rely on *ad hoc* preparation, using processes that cannot readily scale-up to achieve high repeatability at low cost, and which generate negligible yields. Mechanical exfoliation is one such method: by applying normal or shear force to a many-layered van der Waals crystal, typically using a solid interface material, like adhesive tape, the individual van der Waals layers can be separated from one another. This process is capable of isolating monolayers after many exfoliation steps, but does not offer control over the shape or size of the monolayer regions it produces. On the other hand, certain approaches geared towards manufacturing, such as the use of liquid-phase exfoliation, create suspensions of few-layer material which fail to utilize certain unique properties of two-dimensional materials, such as their transparency at low thicknesses and the direct bandgap of some two-dimensional semiconductors in single-layer form. Furthermore, liquid-phase exfoliation produces low percentages of single-layer (monolayer) material, which can have distinct and desirable properties in contrast with its bulk counterpart, as a fraction of the particles in the final suspension.

In contrast to these top-down methods, bottom-up approaches allow practitioners to create two-dimensional materials, ideally in a desired thickness, at will. While chemical vapor deposition (CVD) processes and its variants have made significant strides in recent years increasing the grain size and thus the electronic quality in monolayer growth, these methods continue to face daunting challenges including long growth times, limited substrate options, and imperfect layer control [22, 23].

It is therefore little surprise that few two-dimensional materials have made it to market, including exhaustively-studied platforms like semiconducting molybdenum disulfide (MoS_2). There are two primary explanations: first, that no visionary application has provided sufficient economic incentive to accelerate research into mass-manufacturing; second, that the challenges of working with these materials at scale have failed to tilt the economic calculus towards their adoption into existing engineering frameworks.

This work will examine the progress and paradigms around top-down two-dimensional materials manufacturing, and attempt to illuminate viable paths forward for researchers

and technologists eager to develop processes to deploy these exotic materials at scale.

Graphene manufacturing can be considered mature and economically viable. Graphene has been incorporated into consumer products, including headphones and skis, to improve mechanical properties. Roll-to-roll CVD graphene is being mass-produced for consumer electronics. At the research level, chemical vapor deposition (CVD) on a variety of substrates—as well as complementary methods, like precipitating graphene out of nickel deposited on diamond¹ [24]—make graphene production accessible with a variety of methods. A perspective from Park lays out the pathway to commercialization for graphene and the associated engineering challenges, which applies equally to other two-dimensional materials [25]. Thus, we focus our attention on materials whose manufacturability has prevented them from entering the market altogether. Transition metal dichalcogenides are a compelling and instructive case, both because of the existing body of knowledge gained from the attention they have received in the research community, and the variety of applications they could enable as a result of their semiconductivity, in contrast to graphene’s conductivity.

In this chapter, we identify roadblocks preventing two-dimensional material mass manufacturing, and attempt to determine which methods are promising for the future. To do so, we establish the requirements for a mass manufacturing process, examine prior approaches, and assess their fitness for scalable manufacturing (Section 1.1). We illuminate paradigms that we find dominate thinking around two-dimensional material manufacturing, and probe their validity. We then investigate two specific challenges that we feel are not adequately addressed elsewhere: the issue of material transfer between different surfaces, and methods for attempting to produce deterministic two-dimensional material shapes from multilayer sources (Section 1.2). We explore promising approaches to mechanical manipulation, which could potentially play a role in future manufacturing processes (Section 1.3). This analysis also highlights the interplay between the mechanical manipulation of materials and their ultimate device functions. Finally, in Section 1.4 we summarize our main insights regarding the state of scalable two-dimensional material production.

1.1 Background

Van der Waals materials which have been thinned to their atomic limit show a range of useful properties, which have been detailed exhaustively elsewhere [26, 27, 28]. These properties, and the properties that arise when two-dimensional materials are combined into heterostructures, make them compelling for applications in a variety of fields. When two layers of graphene are combined with a 1.1° interlayer twist, they exhibit superconductivity [29]. Some van der Waals semiconductors, in monolayer form, have a direct

¹The authors deposit a 300 nm thick layer of nickel (along with a thin layer of titanium to promote adhesion) atop a diamond substrate. When heated, carbon atoms in the diamond diffuse into the nickel, then precipitate into graphene on the nickel’s exposed surface during cooling.

band gap, meaning they can emit light when excited [21]. Two layers of these different semiconductors can be combined to make two-molecule-thick p - n junctions [30].

Van der Waals materials may be obtained in two ways: either they are extracted from the earth, or synthesized. Each source presents advantages and disadvantages (Table 1.1). In the case of MoS₂, naturally-sourced material offers large grain sizes and correspondingly high electron mobilities [14]. Moreover, the (large, multilayer) sources are cheap: bulk molybdenite rocks on the order of 20 cm³, for example, can be obtained for under \$10 on eBay. However, there are limitations to using natural sources: new two-dimensional materials, many of which are being computationally uncovered (*e.g.* [31, 32, 33]) are not necessarily naturally occurring; scale-up of extraction (*i.e.*, mining) may ultimately be limited by environmental considerations; and the extracted sources are necessarily multilayer, requiring a further exfoliation step to separate the layers and extract monolayer material. Moreover, naturally occurring crystals generally contain inclusions, impurities, and discontinuities in their structure. Lab-grown material, in contrast, may be directly synthesized as an impurity-free monolayer. However, a new growth process must be devised and tuned for each new material and substrate combination; producing material with large grains and high mobilities is an ongoing challenge [34]; even small amounts of high-quality material requires a growth time as long as 26 hours [35]; and the high temperatures required for growth are incompatible with polymeric substrates, such as polyimide, which may be desired to produce flexible electronics, necessitating transfer of the grown material from the growth substrate to a target substrate [36].

Despite their considerable promise, most two-dimensional material device concepts have only been demonstrated as lab-scale prototypes, with only one material (graphene) having achieved commercialization for mass deployment. Manufacturability is the hurdle. Yield of usable two-dimensional monolayers suffers at several stages: initial material production, transfer to a target substrate, and device fabrication. There has been rapid progress in device innovation, without commensurate progress in manufacturability. Given the demonstrated promise of two-dimensional materials, issues of manufacturability must now be addressed such that these devices may be obtained in an affordable way. Despite advances in CVD and ALD, mechanically exfoliated material continues to be the platform of choice for the highest device performance when naturally occurring sources of material are available. However, mechanical exfoliation is generally perceived to be ill-suited to automation and thus to scaling up for mass-production. Most exfoliation methods yield material with stochastic distributions of shape and thickness, and provide relatively small areas of material in unpredictable locations on a substrate. These sources of variation have made it impracticable so far to build arrays of devices or complex circuits from exfoliated material. In contrast, the possibility for creation of multiple devices simultaneously has been demonstrated with CVD material, although the tradeoff between material quality and growth time needs to be more fully addressed. However, even work which has demonstrated high-yield arrays of two-dimensional material devices on a single chip manages extremely low wafer-level yield, only a few percent [37].

An important part of the promise of two-dimensional materials lies in the creation and

deployment of heterostructures, or stacks composed of different van der Waals materials, which can offer unique and useful properties [38]. We therefore approach our analysis of techniques and requirements with an eye toward the particular demands of heterostructure fabrication. Ultimately, the fabrication of arrays of heterostructure devices requires a means of creating a patterned layer of a two-dimensional material on a target substrate. There are several routes to achieving this end, depending on the sequence of layer isolation (exfoliation), patterning, and transfer to the final substrate (Figure 1.1). While we are particularly interested in the case of MoS₂ and its fellow transition metal dichalcogenides, much of the pioneering work in the field was conducted on graphene. We therefore analyze methods developed for graphene, which may inform the processing of other two-dimensional materials.

1.2 Processing challenges

To achieve pristine patterned monolayers on a target substrate, a candidate mass-manufacturing process must meet several requirements. The process must be able to exert layer selectivity. The layer selectivity may be inherent to the process—for instance, by growing source material with a predetermined desired number of layers—or may be woven into the process by using monolayer-selective methods. A scalable method must offer the ability to multiplex in time or in space to create arrays of deterministic shapes of the two-dimensional material. It must limit residue and contamination damage, which includes avoiding direct contact between the two-dimensional material and a polymers, which have proven difficult to fully remove [39]. Finally, it must avoid strain damage to the two-dimensional material, which means capping the applied strain at 6-11%, the breaking strain of monolayer MoS₂ [40, 41]. Strain may arise from a number of sources, including thermal expansion and contraction, especially of a substrate; from epitaxial lattice mismatches; from surface tension effects in contact with liquid; and from mechanical deformation of a substrate or transfer medium. A candidate process must also impart a pattern to the two-dimensional layers. Two-dimensional materials are amenable to patterning using standard CMOS techniques, and photolithography in conjunction with both wet and plasma etching is widely employed to selectively remove regions of a van der Waals material layer. Imparting a pattern to a van der Waals crystal is not a limiting factor in two-dimensional material manufacturing; therefore, we focus our attention on the issues of transfer and monolayer isolation. We examine those critical challenges here, as well as existing approaches to surmounting them.

1.2.1 Transfer methods

Transfer methods for two-dimensional materials have been reviewed elsewhere (*e.g.*, [42]). Ultimately, transfer from a growth substrate or source crystal to a target substrate

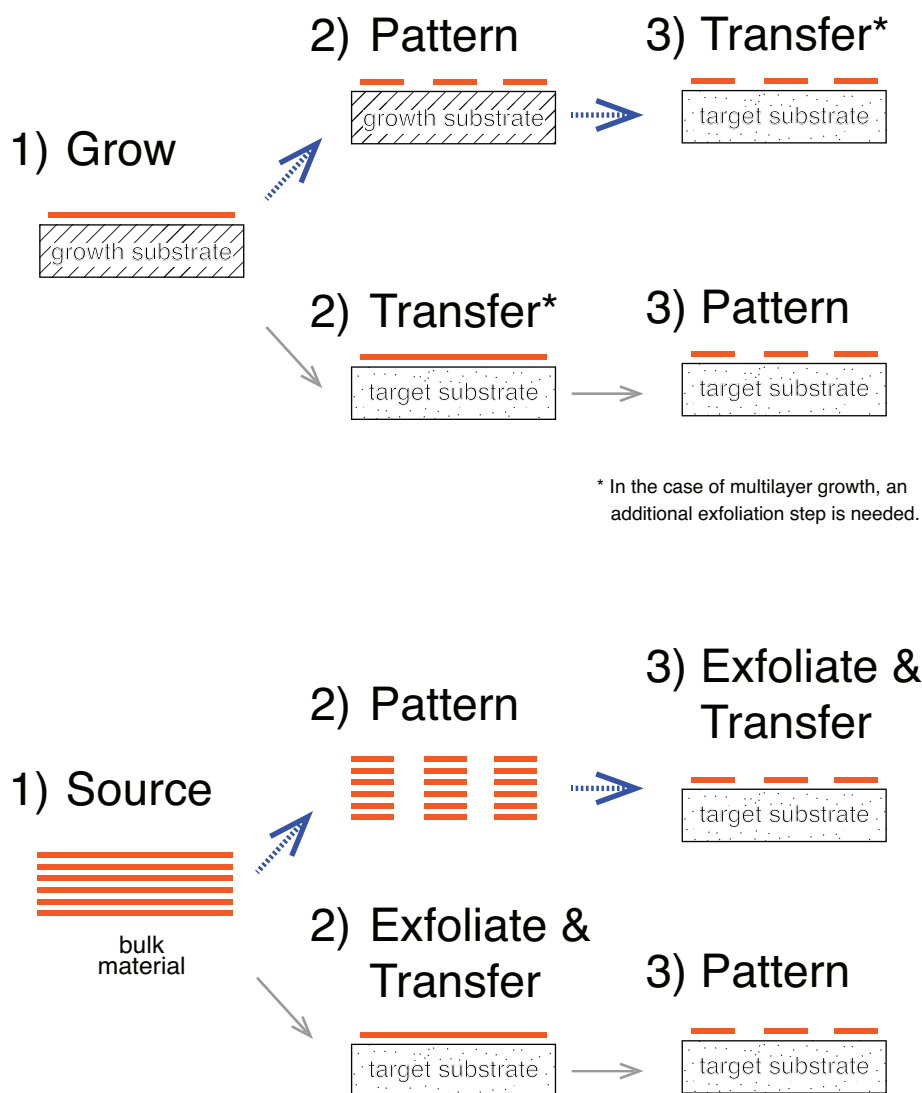


Figure 1.1: Possible routes to achieving patterned, precisely-layered (including monolayer) two-dimensional material arrays on a target substrate, a prerequisite of mass heterostructure device fabrication. Process flows that will not interfere with existing material on a target substrate, and are thus compatible with heterostructure fabrication, use a dashed blue arrow.

is a matter either of carefully engineering surface energies², or of switchable adhesion: the two-dimensional material sheet in question must be picked up and removed at will, with high yield. When fabricating heterostructures, a layer will need to be deposited on an existing two-dimensional material layer on the target substrate. In this case, there is limited opportunity to engineer relative surface energies, and a stamp which can be removed or which can release the two-dimensional layer becomes crucial. Achieving successful transfer is further complicated by the extreme fragility of monolayer films and typical aspect ratios as high as $10^5:1$. In order to achieve conformal contact and thus high yield at the initial pick-up step, polymers have been the transfer media of choice for their low elastic modulus. Polymers, including silicones, acrylates, and ethylenes, maintain their solid phase at temperatures near room temperature and are able to act as structural supports for the sheets. Polydimethylsiloxane (PDMS) and poly(methyl methacrylate) (PMMA) have proven particularly popular for their ease of deposition by pouring or spin-coating, ability to be patterned, common use in microfabrication, and ability to conform at small size scales. PDMS is further desirable for its stability in a large range of environments, and PMMA is attractive for its solubility in a large range of solvents.

Once a polymeric layer is adhered to the film for transfer, the film must be released from its initial substrate. In cases where the bond between the film and substrate is weak, this could be accomplished directly by peeling. Typically, release of as-grown layers onto polymer transfer layers is accomplished by destruction of the initial substrate, removing the substrate/film interface and releasing the film. Potassium hydroxide (KOH) etching of SiO_2 layers is a standard approach. Salts [43] and other water-soluble media [44] have been employed as growth substrates to avoid wet chemical removal of SiO_2 , improving speed and limiting contaminants during the substrate delamination process. However, all these methods continue to rely on pick-up of a film suspended in liquid. This approach is prone to inducing wrinkles in the picked-up film as a result of imperfect initial contact, and liquid material can be trapped at the film/substrate interface (*e.g.*, [45]). One approach attempts to minimize degradation of the substrate during PMMA removal by relying on cavitation between the PMMA and two-dimensional material layer for release [46]. Though the cavitation bubbles produced are on the order of micron-sized, they nonetheless damage the two-dimensional material layer.

Critically, both PDMS and PMMA transfer processes leave residue that affects the electronic and optoelectronic performance of transferred layers [47]. Lin and co-authors suggest that no satisfactory method can exist for completely removing PMMA from the graphene surface, and thus the ultimate performance of films transferred using PMMA will necessarily be limited [39]. Indeed, more recent reports of ultrahigh-mobility graphene, produced by CVD, use transfer methods which avoid direct contact between polymers and graphene, for instance by using an intermediate layer of hexagonal boron nitride [48]. With both graphene and TMDCs, polymeric residue prevents the use of these standard

²For example, an ideally engineered setup may consist of a stamp to which a two-dimensional material adheres, in preference to its growth substrate or bulk form, followed by a target substrate to which the two-dimensional layer adheres, in preference to the stamp.

transfer methods to create van der Waals heterostructures with the pristine interfaces needed for electronic coupling between materials.

The aim of switchable adhesion can, alternatively, be accomplished by the sublimation of small-molecule polymers, which exploit phase change to enhance release of the selected two-dimensional material. Large-molecule thermoplastics simply melt when heated, which is undesirable for the controlled release of material onto a substrate. Surface tension may distort the polymer and deform the affixed two-dimensional material, applying strain and impeding the relative arrangement of a pattern of two-dimensional material pieces. Small molecules, however, may sublime directly to a gaseous phase and diffuse away from the two-dimensional material, effectively releasing the two-dimensional material layer(s) with minimal distortion. In particular, polycyclic aromatic hydrocarbons (PAHs), including naphthalene and anthracene, are readily available, and sublime at easily accessible temperatures which do not damage the two-dimensional material. Naphthalene has been demonstrated as a transfer medium for CVD graphene grown on copper foil [49]. With graphene, this process is enhanced by the fundamental similarity in structure and composition between naphthalene and graphene, enabling initial bonding via strong π - π interactions and perhaps facilitating residue-free release of the graphene [49, 50]. Though leveraging π - π interactions is not possible with other two-dimensional materials, the application of non-destructive phase change that applies limited force to the two-dimensional material is still both achievable and desirable. While, to our knowledge, sublimable PAHs have not been used to transfer TMDCs, molecules based on PAHs have been used to separate and disperse MoS₂ sheets in a form of liquid exfoliation [51]. These results indicate that the concept of noncovalent aromatic interactions (which Matsumoto and co-authors describe as S - π interactions, for the case of MoS₂ interacting with their anthracene-based molecules) can be leveraged to bind PAHs to TMDCs.

Notably, work on small molecule transfer is recent, appearing to have begun in 2017, indicating that the field is turning an eye towards scalable production, and in doing so has begun to appreciate the significant hurdle that material transfer presents.

Small molecule approaches are not a perfect solution. While Chen and co-authors report that naphthalene-transferred graphene retains no residue from the transfer process [49], other work examining the use of PAHs as sublimable adhesives for thin silicon membranes reports the deposition of a hydrophobic residue on the transferred silicon [52]. This residue may be removed with brief exposure to plasma; however, plasma exposure poses an inherent and unacceptable risk of destroying the underlying atomic monolayer. Thus, in applications where a single two-dimensional material is desired, and may be deposited on circuitry without a need for a perfect interface to subsequent layers, PAH transfer mechanisms may be a suitable choice. The process's ability to deliver high-yield release of material without subjecting the transferred material to excessive stress is desirable. However, the imperfect resultant surface may disqualify PAH-assisted transfer as a candidate process for production of van der Waals heterostructures, which require pristine material interfaces.

Using materials other than PMMA as a support layer can also limit material damage

due to strain during PMMA removal. Gold has been used as an intermediate layer, between grown graphene and a PDMS stamp, during transfer [53]. Removal of gold in liquid KI/I₂ etchant can be accomplished without causing the PDMS to swell, which would induce cracks in the attached graphene layer.

Several methods (*e.g.*, [53, 54]) have accomplished transfer of a pre-patterned monolayer onto a target substrate (typically SiO₂/Si). These methods typically pattern the layer on its initial substrate, then transfer the patterned monolayer onto a target. While such an approach is theoretically compatible with heterostructure fabrication, as no subsequent patterning steps which may affect material already present on the target substrate are needed, these methods require that the initial material is itself the desired thickness (typically monolayers) or that only the desired thickness is transferred. All methods discussed thus far are not directly compatible with transfer from multilayers: if the multilayer source is patterned, the transfer medium will contact the entire available area, including unpatterned regions, and offer no layer selectivity.

In principle, tuning the adhesion energies of each interface in the transfer process could yield a technique where the material in question adheres to a transfer medium in preference to its initial substrate, then binds to the target substrate in preference to the transfer medium. In fact, the adhesion energy of MoS₂ to gold exceeds the interlayer binding energy of MoS₂, which is functionally equivalent to the exfoliation energy, by a factor of four [55, 56]. The gold shares a lattice structure with the exposed sulfur atoms, but has a smaller lattice constant. Through the gold-sulfur bond, the gold is able to impose a compressive strain on the exposed MoS₂ layer, weakening the binding of the first layer to the second layer. This weakened interlayer binding suggests a straightforward means of removing an MoS₂ monolayer. Though Magda and co-authors demonstrated such a technique, the use of multiple transfer steps introduced considerable microcracking and wrinkling in the monolayer film on the final substrate [9].

As transfer becomes widely recognized as a limiting factor in two-dimensional material production, a proliferation of recent work has attempted to find elegant solutions to the problem. The trend is towards fewer steps, and the use of very accessible materials. One approach, offered by Ma and co-authors, modifies the standard viscoelastic stamping method—relying on the relative adhesion energies of the transferred layer with the stamp versus with the substrate—by using water as a switchable transfer medium on a PDMS stamp [57]. A thin film of water on the stamp grabs the two-dimensional layer using capillary force. Once the water evaporates, the two-dimensional layer adheres to the stamp less strongly. As with PMMA and PDMS transfer methods, this approach benefits from a transparent layer which is easily made optically smooth, for location and alignment of the to-be-transferred layers. The method is demonstrated to be effective with both graphene and MoS₂. While the authors suggest the use of other organic solvents like ethanol for compatibility with films which are more fragile than graphene and MoS₂, the effectiveness of those other liquids is not tested.

1.2.2 Monolayer isolation

Two-dimensional material exfoliation finds its origins in the Nobel Prize-winning micromechanical cleavage method, using adhesive tape to repeatedly exfoliate graphite until what remained was monolayer graphene [20]. However, few-layer graphene flakes achieved with this method are too small in area for engineering applications, have stochastic spatial distributions, and often have significant imperfections (e.g. inconsistent thickness over flake, material folded onto itself, *etc.*), both within a given flake and between flakes themselves. Similar exfoliation methods have been applied to other naturally-occurring vdW materials, including TMDCs such as MoS₂ and WS₂. Although CVD research has made significant progress in addressing small grain sizes in these TMDCs, its continued deficiencies suggest a place for mechanical exfoliation among an arsenal of methods for mass-manufacturing of two-dimensional materials. However, especially as CVD has matured for graphene, research into mechanical exfoliation and manipulation of two-dimensional materials has diminished.

Bottom-up (growth) methods and top-down (exfoliation) methods each offer benefits and drawbacks, depending on the material(s) in question and the aim of the process (summarized in Table 1.1). It is up to the researcher, or, eventually, the manufacturing engineer, to determine which is more suitable. Initial work on two-dimensional material production focused on top-down methods, with early work aimed at improving few-to-monolayer two-dimensional material yield by optimizing the process of mechanical exfoliation. There remains significant room for additional research to improve upon existing methodologies. However, once CVD methods for graphene were reliably able to produce large areas with few defects, top-down methods for producing any two-dimensional material were written off as ill-suited to scale. Until very recently, the field had shifted to focus almost exclusively on bottom-up methods, to the detriment of important science that could allow top-down methods to enable rapid creation of high-quality devices. Figure 1.2 summarizes existing top-down removal (“exfoliation”) processes in the literature.

Because many methods for manipulating graphene are equally applicable to the manipulation of TMDCs, and several manipulation methods were initially pioneered on graphene, we examine methods originally demonstrated on graphene and/or TMDCs. (Notably, most of the methods pioneered on graphene pre-date 2010, implying that mechanical exfoliation was in the running as manufacturing process for graphene until CVD became clearly dominant.) In 2007, Liang, Fu, and Chou showed the use of a rigid SiO₂/Si stamp to transfer-print 15 μm -diameter graphene flakes onto a SiO₂/Si substrate by applying the rigid stamp normal to bulk graphite [1]. The normal exertion of force appeared to translate to high shear stresses at the edges of the pillars, allowing them to “cut” out pillars, thereby removing an adhered flake directly in contact with the bottom of the stamp surface. The method produced flakes with diameters between 1.8 and 20 microns, while individual flakes’ thicknesses varied by 1.2 nm, and the average thicknesses for flakes ranged from 0.9 to 5 nm (~ 3 to ~ 16 layers). Additionally, Liang and co-authors tested the effects of oxygen plasma treating the substrate to enhance adhesion between

Table 1.1: Comparison of top-down and bottom-up sources of monolayer van der Waals sheets.

	Bottom-up	Top-down
Benefits	Straightforward control of the number of layers	Applicable to arbitrary sources
	Feasible for materials which are not known to occur naturally	Includes natural materials, which typically have larger grain sizes and better electronic quality than synthetic sources
	Avoids irregularities of working with natural materials	Some natural sources (for instance, molybdenite) can be procured for 3 orders of magnitude lower cost than synthetic sources
Drawbacks	Sources must be produced synthetically	Must start with multilayer source: need for layer-selective removal methods
	Typically higher defect density than natural sources	Multilayer sources are not readily available for all van der Waals materials
	Growth recipe must be created and refined for each new material and substrate combination	Requires transfer to target substrate
	Recipes are substrate-specific: still requires transfer to a target substrate	

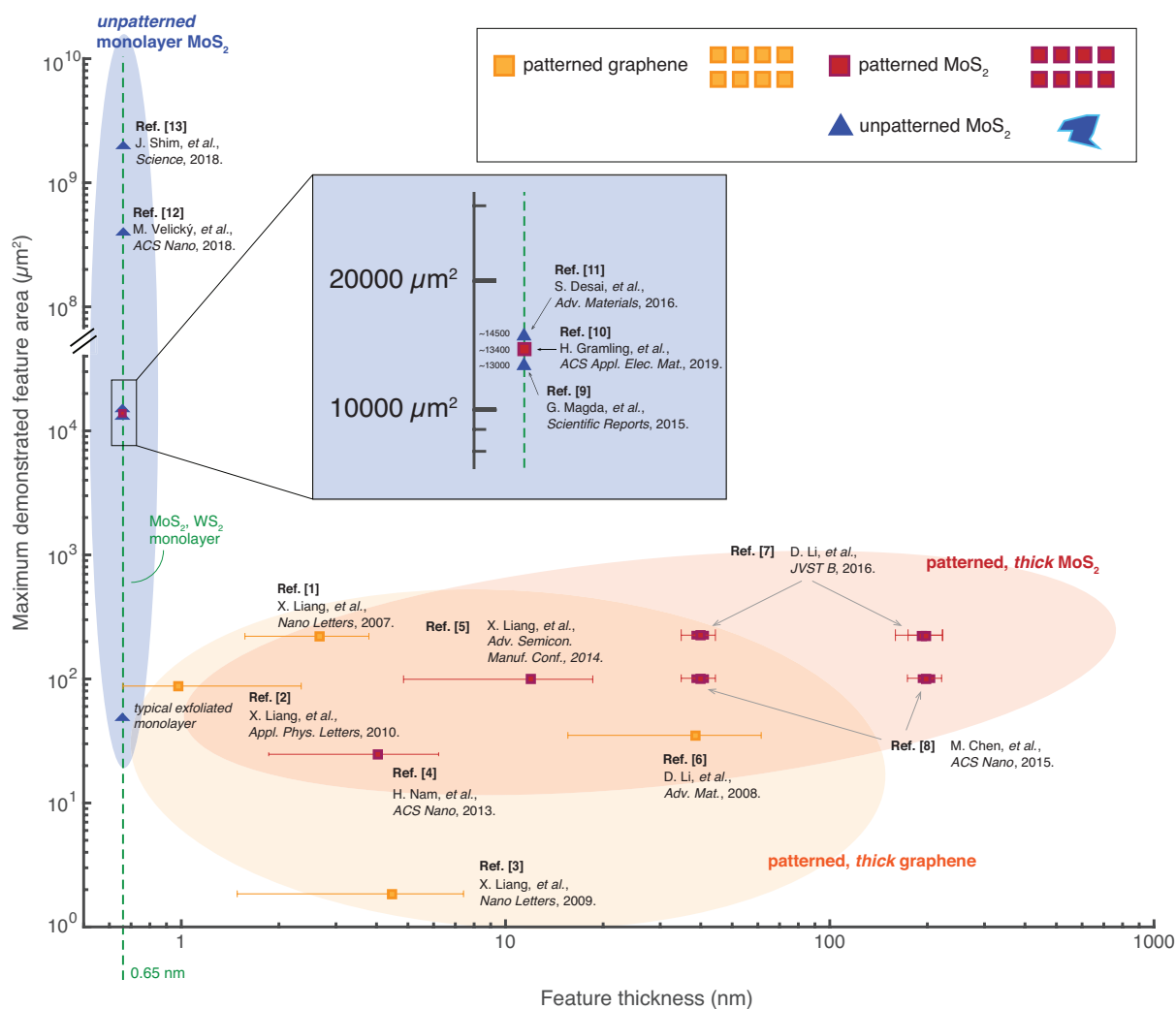


Figure 1.2: A comparison of size scales demonstrated with exfoliation methods on multilayer MoS₂ and graphene, illustrating the inability to achieve large-area, patterned monolayers. Refs. [1, 2, 3, 4, 5, 6, 7, 8, 9, 10, 11, 12, 13].

the picked-up graphene and the receiving surface, but their results suggested that the oxygen plasma treatment diminishes electron and hole mobility with questionable increases in flake transfer efficacy. The tradeoffs involved in plasma treatment of substrates is currently an area that demands further investigation, especially given the prevalence of this method and the lack of agreement surrounding its best practices. For two-dimensional materials' envisioned applications, this work would need to address issues, such as rippling and incomplete transfer of a given flake, that would impede ultimate device performance. Improved consistency in their chosen metrics—the inter- and intra-feature variations in layer thickness—would be critical before this method could be deployed at scale.

One important area of research surrounds the optimization of transfer printing parameters, especially the stamping process. Density functional theory (DFT), a computational method of simulating the electronic structure of materials at the molecular level [58], was used by Li and co-authors in total energy calculations within the local-density approximation, and their accompanying experimental measurements confirmed that few-layer graphene (FLG) stamping is energetically favorable (as opposed to no cleavage, or leaving behind many layers) without needing to use interfacial layers [6]. While Li's work demonstrated the feasibility of using a patterned bulk graphite stamp in transfer printing, the transferred pillars demonstrated a substantial range of thicknesses, while other quantitative data that could be used to indicate success were not reported, such as mean and standard deviation of thicknesses, suggesting that either the assumptions used in DFT and/or the patterning process of graphite stamps are additional areas worthy of investigation for optimization.

Chen, Reddy, and Padture effectively build on Li's and co-authors' work by investigating the use of flexible stamps as an intermediate step between bulk patterned graphite and the final substrate [59]. They posit that this intermediate step will not only facilitate freshly cleaved graphene surfaces (and therefore cleaner surfaces) for better substrate adhesion but also more even pressure distribution for the printing process. Their results qualitatively demonstrate higher levels of consistency between and within individual flakes than were achievable with stiff stamps, but the lack of quantitative data surrounding the distribution of number of layers, and a lack of control of applied pressure when stamping, make it difficult to assess how different process parameters impact yield. Further work to optimize the mechanical properties of exfoliation stamps would be valuable.

Electrostatic forces have also been experimented with to aid van der Waals material exfoliation, and have reliably improved results. Research into the implementation of electrostatic forces has taken two broad approaches: (1) biasing the stamp relative to the substrate by using two electrodes (one on the stamp and the other on the substrate), and (2) simply plasma treating the intended substrate, as Liang and co-authors demonstrated in 2007 [1], to produce dangling bonds that are more strongly attracted to the intended exfoliation material. Sidorov and co-authors explored the former approach, and, by adjusting the voltage across the electrodes, managed to exfoliate a small monolayer, along with thicker regions, from a bulk, unpatterned highly-ordered pyrolytic graphite (HOPG) stamp [60]. They do not report the mean or maximum thickness of the exfoliated flakes.

Notably, they also find an increase in the step height of the monolayer from 0.35 nm to 0.8 nm over 45 days, which the authors suggest is due to a strong initial electrostatic adhesion force that decays over time. The increase could also be due to the adsorption of molecules to the surface of the layers. Both of these values are consistent with other values of monolayer step heights, given that monolayers in other papers are typically ~ 0.3 – 0.4 nm in thickness and that imperfect adhesion with the substrate typically results in marginally higher step heights. Additionally, a fold observed by Sidorov in this monolayer suggests the need for greater control of the electrostatic attraction because even relatively insignificant differences in angle between the normal of the stamp and the normal of the substrate can cause flakes to exfoliate at angles, rather than normally, as intended. The authors do not quantify the areas of transferred flakes.

Similar results were achieved by Liang and co-authors, who took a comparable approach but with a pre-patterned bulk graphite stamp [3]. Liang and co-authors used simulations to determine the minimum field strength necessary to exfoliate a monolayer. They applied this voltage to a patterned “stamp” of HOPG in contact with a silicon/SiO₂ substrate (Fig. 1.3), and found similar thickness variability to that of Sidorov, with thicknesses within a particular flake varying between about one and five atomic layers, with an average flake thickness of about four atomic layers. Over an array of 135 flakes in a single processing cycle, the total thickness range was one monolayer to 87 atomic layers with a mean thickness of 12 layers and a most likely value of seven layers. The large thickness range suggests that potentially excessive electrostatic force may have been applied, or that the force was not applied completely normal to the interface, resulting in different force components being experienced by each pillar. The sparsity of actual monolayer regions suggests that there is room to optimize the applied force and its spatial uniformity.

Further work by Liang and co-authors combines the same biasing of two electrodes—one connected to the stamp and the other to the substrate—with a pre-patterned HOPG film, which is rolled onto a conductive cylinder to form a roller-style graphite template. Throughout the rolling process, a voltage is applied between the roller template and the substrate. This approach combines rolling friction with electrostatic attraction, yielding promising results, with 70% of exfoliated flakes being trilayer or thinner. However, like all previous work, they experienced problems with consistency of thicknesses, within and between flakes. Additionally, the procedure of this work is difficult to scale, as precise uniformity in wrapping the film around the cylinder is required. Of the works assessed herein, this effort presented by far the best results in achieving few layer graphene, so the results of this investigation would warrant deeper research into the optimization of the parameters used (*e.g.* voltage difference, substrates, rolling speed, and rolling pressure) [2].

Plasma treating the substrate to create the potential difference between the deposited material and the substrate surface has also been explored as a means of using electrostatic forces to preferentially exfoliate few-layer two-dimensional materials and has become a standard method of improving adhesion between two-dimensional materials and their substrates in recent years. Advantages to this method, as opposed to the aforementioned

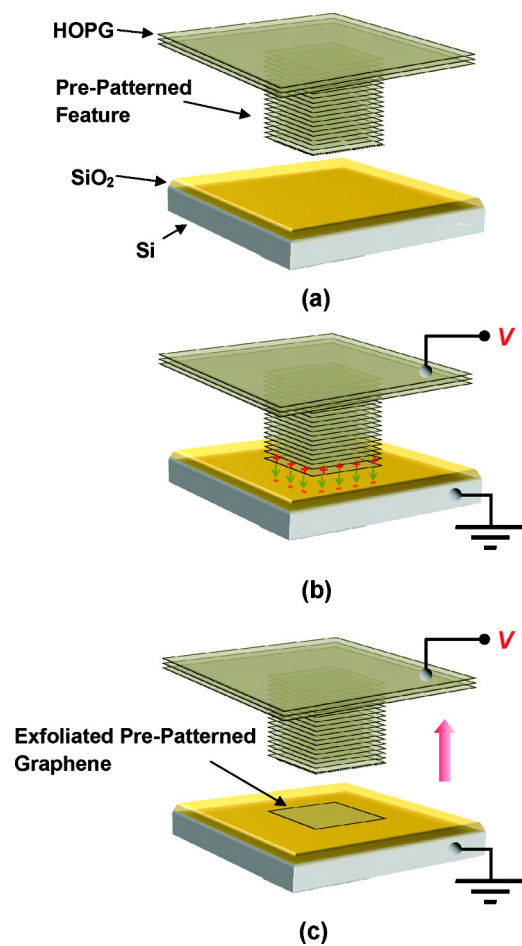


Figure 1.3: Biasing of stamp/substrate for electrostatically assisted exfoliation (Liang *et al.* 2008 [3]).

voltage-generated method, include its accommodation of a wide variety of substrates, and its even distribution of charge across the entire substrate, allowing for better printing by achieving reproducibility and reduction of variance between flakes. Nam and co-authors explore this method by prepatterning an MoS₂ stamp and stamping it normally against a plasma treated SiO₂/Si substrate. Their results, however, indicate a pattern where the outer edges undergo stronger exfoliation due to the electrostatic attraction, leading to “donuts” that prevent uniform exfoliation of individual flakes. The authors explain this phenomenon using Maxwell stress tensor calculations which indicate that the surface charge densities were higher on the outside edge of exfoliated flakes. They achieved an overall average thickness of outer edge ribbons of 17 nm (~26 monolayers) with a standard deviation of 3 nm (~5 monolayers), whereas the overall average thickness of inner films was 3 nm (~5 monolayers) with a standard deviation of 1.9 nm (~3 monolayers). About 90% of inner flakes of MoS₂ pixels printed on a plasma-charged SiO₂ substrate were thinner than 5 nm (~8 monolayers) [4]. The high field effect mobilities here suggest that plasma treating may not be bad for mobilities, which is in disagreement with Liang and co-authors’ 2007 work, further indicating the necessity of additional research. The results of Liang and co-authors’ roller-style electrostatic printing achieved promising results and implied that shear force can help not only with uniformity but also with achieving fewer layer flakes. Shear is inherently preferential for the exfoliation of two-dimensional materials because of their molecular structure: the atoms within sheets are strongly covalently bonded in the plane, but the van der Waals bonds between sheets are significantly weaker. Nanoimprint-Assisted Shear Exfoliation (NASE) is a burgeoning method that builds on this fundamental idea by explicitly using shear exfoliation as opposed to normal exfoliation in the transfer printing process. Chen and co-authors demonstrated the first NASE system by taking a bulk patterned MoS₂ stamp and shearing laterally while the stamp is indented in a polymeric fixing layer that covers a substrate (Fig. 1.5). There are disadvantages to this procedure that should be addressed in future work: the use of polymer fixing layers (as opposed to simply plasma treating the surface) leaves residues which are difficult to remove in post-processing. In their careful work, the authors only achieved 50-60% yield of exfoliated flakes suitable for FETs. The authors were unable to produce flakes of consistently high quality below thicknesses of 40 nanometers, and managed a flake transfer success rate of 80% and the same types of inconsistencies between and within flakes’ thicknesses as Liang and co-authors’ original 2007 work. The primary value of Chen and co-authors’ development of NASE was in the explicit exploration of shear force as a means of preferentially exfoliating few-layer TMD³ materials, including analysis of the force regime in which layers will slide apart without rippling [8]. The introduction of a fixing layer, while offering the potential to achieve better consistency, fundamentally opposes one of the primary goals of two-dimensional material production by introducing a > 1 layer floor on the number of layers removed. The ability to remove

³The group had previously demonstrated use of shear force in exfoliating graphene, in their work on HOPG rollers [2].

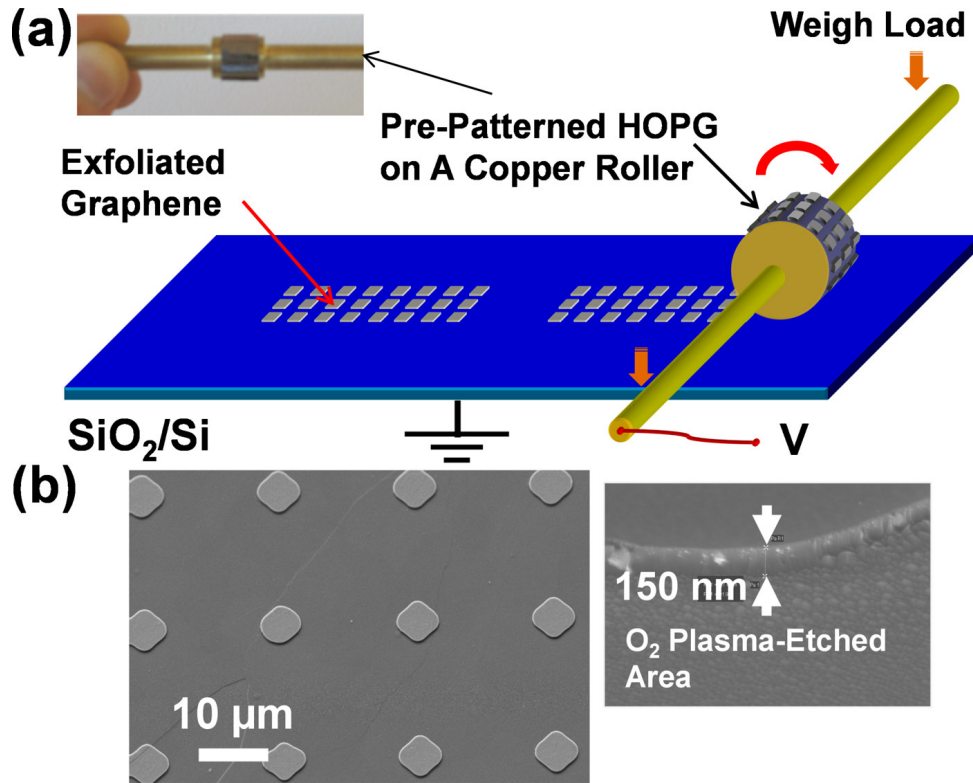


Figure 1.4: Roller style exfoliation (Liang *et al.* 2010 [2]).

a small number of layers is now dependent on the deformability of the fixing layer, and the tradeoff between achieving fine control of deformability resolution and generating sufficient force to remove layers. The inability to achieve control of the number of layers removed is a considerable limitation of the work. Most importantly, however, the fixing layer makes post-processing significantly more complex and adds additional steps by which imperfections can be introduced to otherwise potentially pristine material.

Li and co-authors extended the development of NASE and forwent the polymeric fixing layer by instead starting with a bulk, patterned MoS₂ stamp, pressing it into a soft PDMS stamp, shearing the patterned mesas on the bulk MoS₂ relative to the PDMS surface, then using the PDMS stamp with embedded MoS₂ pillars as a transfer printing stamp. The presumption is that by shearing into the PDMS stamp, the exposed surfaces of the transferred pillars will be cleaner than the exposed surfaces of a directly patterned bulk MoS₂ stamp and therefore adhere to the intended substrate more effectively, in addition to having fewer layers compared to a bulk MoS₂ stamp. This line of logic is contrary to the reported results of aforementioned papers: the motivation behind using friction is to reduce the number of layers on the substrate, and not to reduce the number of layers on the stamp. Li and co-authors' own results offer evidence on why this use of friction may not be the most promising: they achieved a mean thickness of 91 nm,

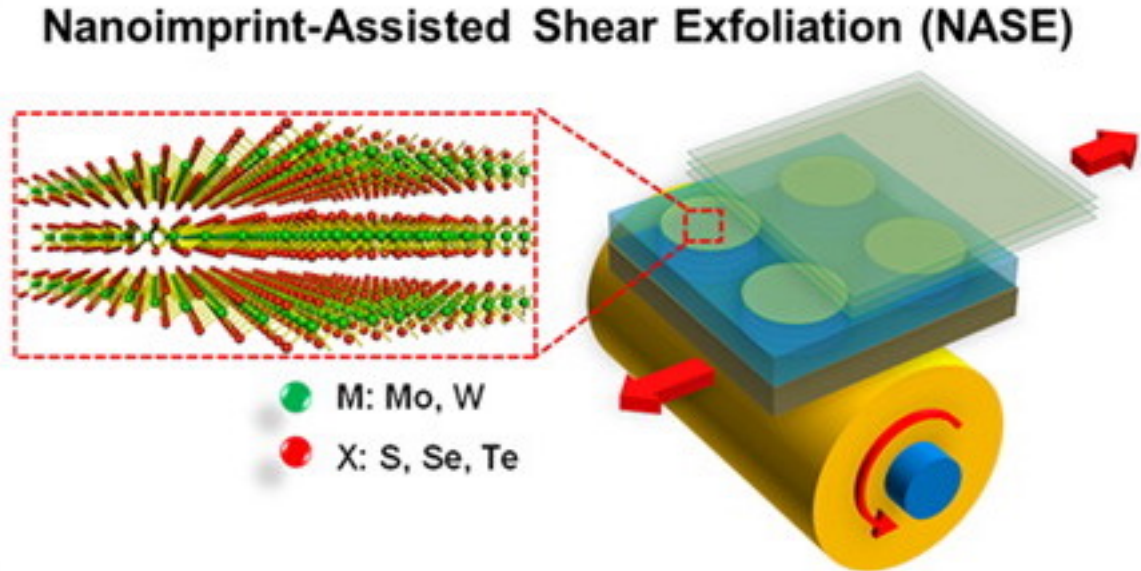


Figure 1.5: Nanoimprint-assisted shear exfoliation (NASE) of MoS₂ (Chen *et al.* 2015 [8]).

with 80% of transferred flakes between 80 and 120 nm. The percent variance can be considered relatively low (though likely still not to mass-manufacturing standards) though the high mean thickness disqualifies this approach entirely as a means of monolayer-to-few-layer heterostructure fabrication, without significant further work. It is unclear whether the relative variance will scale to lower (more desirable) produced thicknesses [7]. The authors later attempted to devise a scaling law for production of patterned TMD layers [61]. The authors posit that below a critical thickness as a function of lateral dimension (for instance, below a thickness of 10 nm for features 10 μm in lateral extent), no features can be produced without significant damage. Indeed, the thinner structures they demonstrate resulting from this process are consistently damaged, with low yield of features, and considerable thickness variation and missing material within transferred regions. Ultimately, they assert that achieving monolayer material using a stamping method requires the features' lateral extent to be smaller than 10 nm. While these relationships may hold in the absence of surface modification, work on metal-assisted exfoliation—which offers monolayer selectivity, while maintaining the electronic quality of the TMD material, as discussed further below—largely nullifies the relevance of this scaling relationship.

From a fracture mechanics perspective, the transfer printing method introduced by Liang and co-authors in 2007 utilizes a Mode I fracture, propagating a crack by separating graphene sheets perpendicularly to the faces of the sheets. NASE then utilizes a Mode II fracture, propagating cracks between graphene sheets by sliding them over each other. From an energy perspective, exfoliation is best viewed as competing forces of adhesion (between a two-dimensional material layer and the substrate) and cohesion (between

individual layers of the two-dimensional material). As explored by Li, Dongsheng, and Padture [6], normal force exfoliation is capable of few-layer exfoliation. Shear exfoliation processes, like NASE, exploit the increased energy barrier imposed by the friction between the outermost vdW flake and the substrate, which the cohesive force attaching the vdW flake to the stamp cannot overcome. (One method, mentioned in passing, for increasing the adhesive force between the vdW flake and the substrate is to increase conformity of the vdW material to the substrate). Huang and co-authors improved upon the sticky tape method by experimenting with the effects of annealing on the transferred area of two-dimensional materials [62]. Surface area yield increased 20-60x with their annealing, relative to surface area produced without annealing, with the authors positing that the annealing allowed for better conformity between the graphene flake and the substrate by allowing for the release of gas trapped between the transferred material and the substrate. The optimization of temperature and anneal time were constrained by the need to minimize the adhesive left on the flake/substrate while maximizing the effect of the annealing in enhancing the conformity. The authors speculate about a physical explanation for why annealing works. Yuan and co-authors explored the limits of tape exfoliation by testing the effects of exfoliation speed [63]. At their empirically determined optimal speed, 22.2% of exfoliated graphene flakes are 20-30 μm thick and 50% of exfoliated WSe_2 flakes are 10-20 μm thick. They claim there is limited tearing and little residue left behind, but do not report electronic measurements that would validate this claim. Additionally, many few-layer regions are still attached to thicker flakes, and the authors did not report any compelling figures for the regularity of flake areas. The effect of angles of removal other than 180° would have been interesting to investigate and report.

Gold has also proven to be a highly effective intermediate transferring substrate for exfoliating two-dimensional materials: it is inert while still exhibiting strong affinity to sulfur, which makes it particularly useful for manipulating sulfide TMDCs. Both sputtering and evaporation have been explored as means of gold deposition. Song and co-authors experimented with sputtering a gold film onto HOPG patterns, peeling off the gold film and any attached graphite using thermal release tape, pressing the thermal release tape onto a substrate, then releasing the tape and etching away the gold [64]. Typical imperfections associated with this exfoliation method included broken flakes and incomplete transfer. However, $> 50\%$ of flakes were ~ 1 nm or thinner, suggesting that gold bonds to graphene very preferentially. The authors speculate that the broken transferred flakes were likely a result of the thermal release tape or the oxygen plasma etching. Magda and co-authors explored the use of gold in exfoliating monolayers by first peeling off flakes from bulk MoS_2 using thermal release tape, placing tape onto freshly cleaved gold, and releasing the MoS_2 from the tape onto a SiO_2/Si substrate [9]. Ultrasonic treatment in acetone was experimentally determined to exclusively leave monolayer MoS_2 attached to the gold, which is an indication of strong MoS_2/gold adhesion. Then tape is placed onto gold and then the gold is etched away using potassium iodide. The tape is placed back onto an SiO_2/Si substrate and heated to release the monolayers. The resulting areas are reported to have lateral sizes up to the order of hundreds of microns (Fig. 1.6c). The

authors claim that the process is reversible because Raman spectroscopy indicates lack of significant structural damage to the flakes. The authors applied this method with success to other layered chalcogenides, including tellurides and selenides. While additional testing of electronic properties would provide more compelling evidence that the process maintains the integrity of the materials, these results suggested that the use of gold as an enabling layer merited further investigation. In combination with Song and co-authors' 2009 work, this suggested that development of transfer methods using gold is a promising avenue for scalable manufacturing of two-dimensional materials. Notably, the NASE process detailed by Li and co-authors uses pre-patterned Au or Ti layers on the substrate. Though these are nominally meant to serve as contacts for electronic devices, they refer to these metal strips as "fixing layers," implying their utility in improving the adhesion of TMDC layers to the substrate. However, as discussed, this work does not demonstrate monolayer selectivity. Subsequent work by Desai and co-authors demonstrated the effectiveness of deploying the gold-sulfur bond in a different process flow [11]. By first evaporating gold onto TMDCs, then peeling the gold-TMDC stack away from the bulk TMDC crystal using thermal release tape, the authors were able to place large-area ($> 13,000 \mu\text{m}^2$) monolayers of MoS_2 (Fig. 1.6d), WS_2 , and WSe_2 on an SiO_2/Si substrate. Arguably the contribution of this work is not in having demonstrated, again, the potential of gold to preferentially extract monolayers, but rather their generation of large sample sizes leading to preliminary statistical analysis. To our knowledge, this effort marks the first time that exfoliated TMDC monolayers were produced in sufficient quantities to merit statistical analysis in a publication. With scalability in mind, repeatability in these quantities implies the approach is not being treated as an *ad hoc* laboratory-scale production method.

A spate of follow-on work, including several recent publications, attempts to flesh out the underlying science of metal-assisted exfoliation methods and demonstrates their applicability to synthesized sources. Zhou and co-authors first explore the concept of epitaxial growth on a compliant substrate, wherein the growth process itself induces strain in the substrate as a stiffer layer (with equivalent lattice structure, but different lattice constants) is deposited [65]. Sun and co-authors elaborate on why this mechanism could preferentially induce separation between the top and second layer of the vdW material, resulting in monolayer exfoliation. They show both that shear strain is not transferred to the second layer, and that the resultant lattice de-registration between the top and second layers decreases the interlayer bond energy per unit area [66]. From a fracture mechanics point of view, this means the energy release rate of crack propagation will be smallest when the first and second layers are separated; in other words, as energy (in the form of normal displacement) is added to the system, the most energetically favorable means of accommodating the normal strain in the system is to decouple the first and second vdW layers. Shim and co-authors manipulate the energy release rate to achieve spalling-style fracture between layers [13]. Velický and co-authors found that the roughness of the gold surface which contacts the TMDC governs the yield of exfoliated monolayer, with a smooth surface performing better [12]. Thus, a 100 nm thick gold layer, which is rougher

than a 7.5 nm thick layer, offers nearly 90% lower monolayer yield than the 7.5 nm thick layer. This inverse correlation between the thickness of the gold layer and the monolayer selectivity of the process does not hold when the gold layer is deposited directly onto the multilayer TMDC surface; a 100 nm thick gold layer can select TMDC monolayers with a yield well above the 10% reported by Velický and co-authors [10].

In a bottom-up approach, the selective oxidation of an ultrathin layer has been used to synthesize monolayer material. Carey and co-authors used the oxidation of liquid gallium to selectively remove all but an ultrathin skin of gallium oxide on a target substrate, which they then converted to the two-dimensional semiconductor gallium sulfide [67].

Interestingly, a tradeoff between patternability and material quality emerges. In the work of Carey and co-authors, the fact that the initial template layer is put down as a liquid makes it amenable to patterning; the authors accomplish this by using a screen-printing-like technique. However, because the technique involves fragile solid-state layers, microcracking is a concern: the synthesis process for this material yields electron mobilities two to three orders of magnitude smaller than that of monolayer TMDCs produced by any current method. In the case of metal-enabled exfoliation, the technique is applied to as-formed bulk material, including natural sources. Introducing heterostructure-fabrication-friendly patterning (*i.e.*, before the layer of interest has been placed on the final substrate) presents engineering challenges. However, the approach can produce monolayers of material from sources with maximum mobility (mined sources are the gold standard for mobility and grain size, and historically provided the measure to which synthesis methods are compared).

Usefully, the requirement for monolayer selectivity lends itself to schema that take advantage of surface interactions. More granular layer tunability—for instance, the ability to select one, two, or four layers on demand—presents a greater challenge. Multiple techniques for using surface interactions and mechanics to differentiate and decouple a single layer have been demonstrated in the literature. Though the approaches are material-specific, the underlying principles may be applicable to multiple materials. There are undoubtedly all kinds of clever means of manipulating the surfaces of vdW materials, and careful understanding of the surface properties of materials of interest, as well as of their target substrates, could yield an elegant, scalable, and perhaps even low-cost means of producing non-random monolayers.

1.3 Leveraging mechanical phenomena

Future methods of transfer and patterning could take advantage of the mechanical behavior of two-dimensional materials. For instance, one could impart a pattern to a transferred layer by preferentially bringing predetermined regions of a two-dimensional layer into contact with a substrate. Preferential contact could be achieved by shaping the layer using kirigami, a method for achieving three-dimensional shapes via a series of cuts and folds in two-dimensional layers, which researchers have applied to two-dimensional

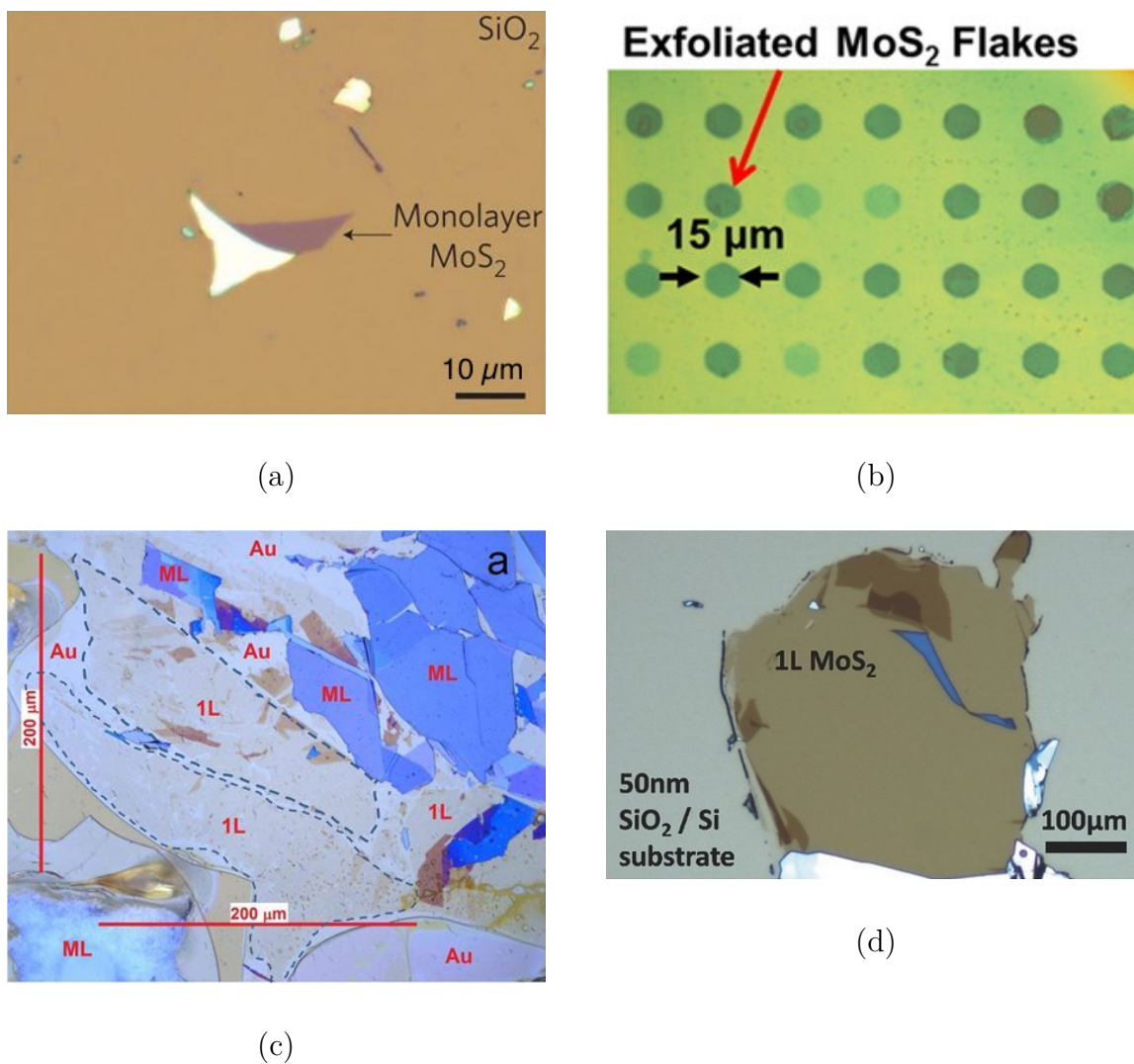


Figure 1.6: a) Typical exfoliated monolayer MoS₂ (Radisavljevic *et al.* 2011 [14], scale bar length added). b) Most uniform reported result of (non-monolayer) MoS₂ produced by nano-imprint shear exfoliation (NASE) (Chen *et al.* 2015 [8]). c) Monolayer MoS₂ produced using the gold-assisted exfoliation method of Magda and co-authors [9]. d) Monolayer MoS₂ produced using the gold-assisted exfoliation method of Desai and co-authors [11].

materials in order to investigate new device concepts. A similar effect could be achieved by controlled rippling. Though these approaches are merely speculative, we survey ongoing work into mechanical manipulation of two-dimensional materials, in the hopes it may stimulate further research to better quantify the mechanics of two-dimensional materials, or even inspire new manufacturing approaches.

Two-dimensional materials intrinsically exhibit anisotropic mechanical behavior. Graphene has theoretical values of 1 TPa and 130 GPa for its elastic modulus and strength, respectively, indicating high potential as a structural material if manipulated properly, and has already proven its strength in limited instances such as water filters and sensors today. Large grain two-dimensional materials are necessary for applications in semiconductors, medical devices, energy generation and storage devices, etc. Previously investigated phenomena include superlubricity and graphene’s negative coefficient of thermal expansion. One promising area of research is in manipulating two-dimensional materials to impart functionality in three-dimensions. While metamaterials have existed as an area of research for over a century, advances in nanomanufacturing offer exciting new opportunities that address current deficiencies in metamaterials by creating functionally new materials continuous at the atomic level. Bles and co-authors utilized the idea of kirigami, from the Japanese art of cutting and folding paper, to create graphene structures at the microscale with tuned elastic moduli (Fig. 1.7) [15]. With molecular dynamics (MD) simulations, Hanakata and co-authors [68] as well as Han and co-authors [69] confirm the viability of intelligently placed cuts as a means of increasing the extensibility of the additional two-dimensional materials MoS₂ and hexagonal boron nitride (hBN), respectively. Mortazavi and co-authors extended Bles and co-authors’ work, finding in their MD simulations of graphene kirigami that the cuts enabled tunable thermal conductivity [70]. Additionally, Zhao and co-authors used MD to simulate how kirigami cuts in an idealized carbon nanotube’s walls could confer the nanotube extensibility to address CNTs’ relative brittleness [71]. However, the differing geometries simulated in each of these works indicates the need for a standardized simulation geometry and chirality (much like the ubiquitous transistor offered a standard geometry for testing material conductivity and on/off ratios). Of note, recent work by Hanakata and co-authors [72] using machine learning to generate new cut guidelines for kirigami hints at the usefulness of computation for both prototyping at the nanoscale and for eliding the need for analytical theory, though here computational brute force stands in for first-principles design guidelines. The authors explicitly note that their findings offer a method which requires no “prior knowledge of the fundamental physics.” Nonetheless, it would be interesting to see this technique applied to kirigami objectives beyond maximizing stretchability—would a different physical objective require an entirely new neural net? A method that allows designers to create a system to their specifications would be a powerful tool in the nanomanufacturing space.

The lack of additional experimental achievement of kirigami applied to two-dimensional materials (despite the multiple simulations) indicates that the kirigami may be more difficult to achieve than Bles and co-authors documented. Bles and co-authors themselves indicate that their polycrystalline graphene samples exhibited unexpected stiffness and

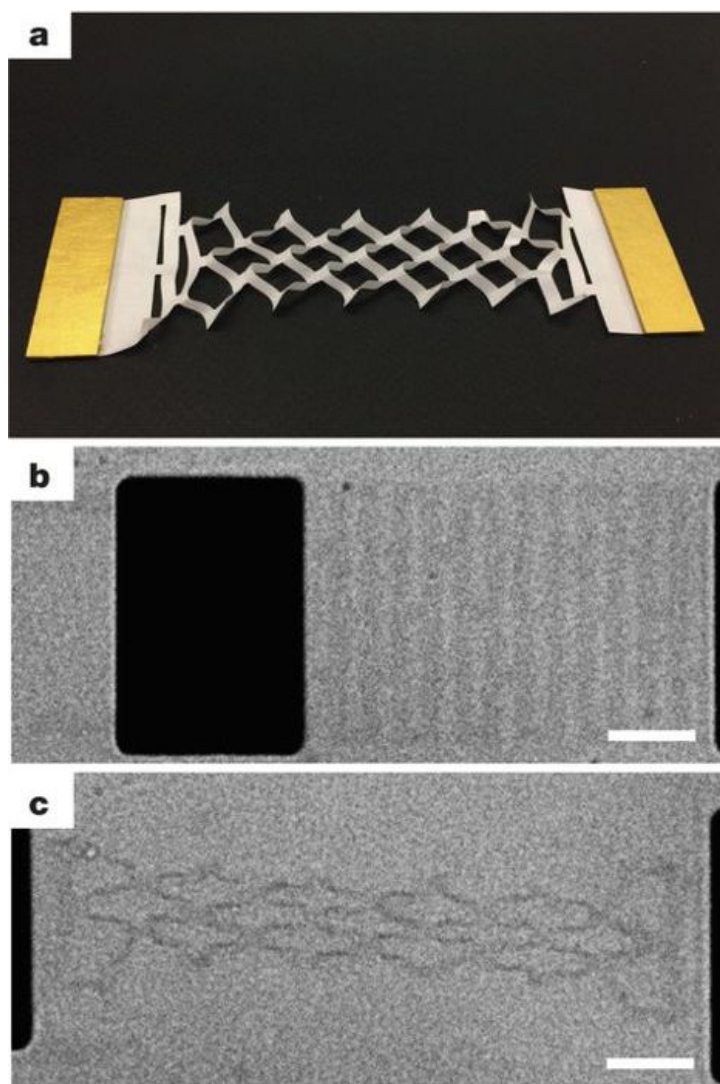


Figure 1.7: a) Paper, and b) graphene kirigami structure, unstretched, and c) stretched. Scale bars $10\ \mu\text{m}$ (adapted from Bles *et al.* 2015 [15]).

posits that it may have been linked to the wrinkling in their samples. Given the prevalence of wrinkling as a defect, its impact on the material properties of two-dimensional materials, and the high variance of other papers' wrinkled samples' material properties, additional investigation into generating a unifying theory on the effects of wrinkling may be necessary. The deep interrelation of mechanical and electrical properties signifies that the eventual understanding of these defects will lead to controlling rippling which could further expand mass manufacturing capabilities and other potential usages across the span of structural and electronic uses of two-dimensional materials.

The mechanical properties of 3D structures composed of two-dimensional materials is also of great concern, and is an obstacle that needs to be better understood for the design of future manufacturing processes. Qin and co-authors simulated 3D graphene structures using molecular dynamics, normalized them with the actual (invariant) mechanical properties of graphene, and created a scaling law based solely on their own simulations [73]. While these results were somewhat aligned with experimental values of graphene aerogels of other papers (the authors show no error bars), it casts a shadow on the legitimacy of using significantly scaled-up 3D printed structures, where a different set of forces dominate behavior. Because of the difficulty of precisely manufacturing these 3D structures consistently, the idea of self-assembly, where clever cuts can be made into two-dimensional materials then thermally activated, has gained traction [74]. Micromanipulators and gold pads may damage the structural integrity of graphene. Using non-contact methods, such as magnetic manipulation [75], could offer higher yield. Solvent-driven structural patterning of two-dimensional materials, demonstrated in Choi and co-authors' work integrating layers of graphene onto surfaces with out-of-plane features, also provides a promising avenue to heterostructure formation because it facilitates the conformation of layers of two-dimensional materials onto substrates (Fig. 1.8) [16]. The authors have also demonstrated the effectiveness of the method with MoS₂ [76]. This process faces the challenge of requiring a substrate that is able to be "swelled" using some liquid.

Fabrication difficulties arise as a result of rippling. As follow-on work has sought to understand the provenance of rippling, the possibility of leveraging controlled rippling to modify the electronic and optoelectronic properties of TMD devices has been investigated. It has been shown that rippling can be caused by differential thermal expansion [77], be it a thermal gradient between the material and the substrate it is processed on, or thermal gradients within the material itself during growth. Wang and co-authors build on this idea with large-scale "crumples" induced by localized heating of a polystyrene substrate upon which they placed graphene [78]. Because of the difficulty in controlling thermal fluctuations, it is necessary to understand how important rippling is to electronic and mechanical properties, before attempting to use induced heating to produce wrinkling at scale. Two works from 2007 investigate wrinkling in graphene in more detail. Meyer and co-authors offer that the existence of ripples in suspended graphene suggests that ripples are, in fact, substrate-independent [79], while Fasolino and co-authors used Monte Carlo simulations to argue that ripples are intrinsic to graphene's stability [80]. Ultimately, however, inducing rippling is simply a matter of controlling strain mismatches in the material,

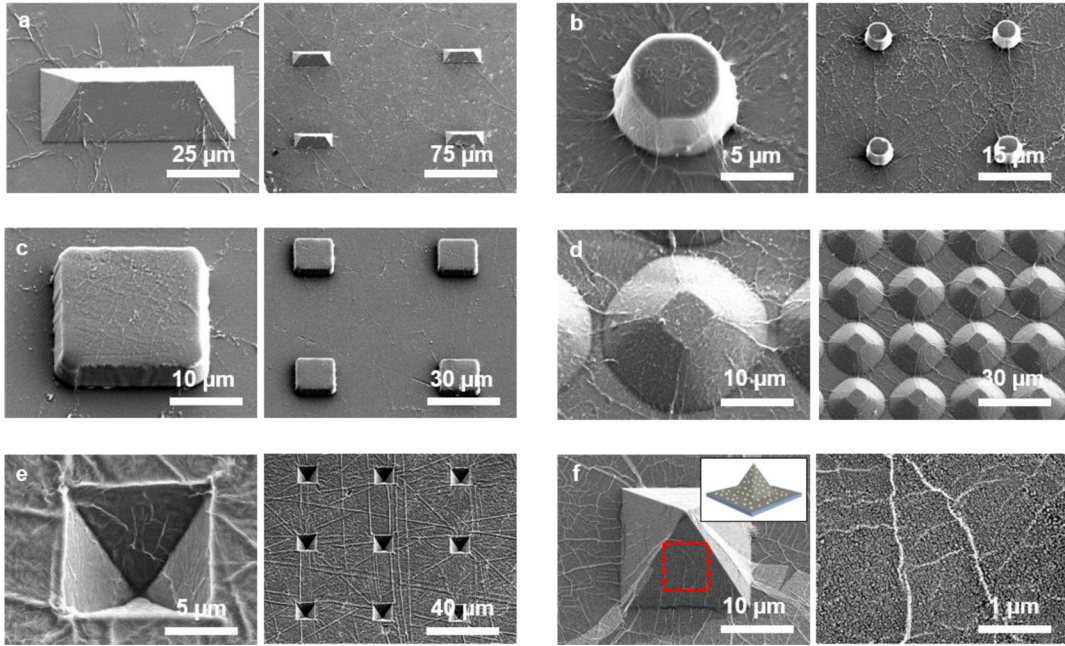


Figure 1.8: Solvent driven conformity of two-dimensional materials onto textured substrate (Choi *et al.* 2015 [16]).

whether those mismatches are induced thermally or otherwise [81]. Large-scale ripples in two-dimensional materials could find applications in stretchable sensors and electronics (*e.g.*, [82]), while nano-to-microscale ripples can be used to induce optical anisotropy (*e.g.*, [83, 84]) and increase surface areas for sensing applications, the importance of which has been noted for MoS₂ [85] and demonstrated in phosphorene [86]. While micron-scale and larger ripples may be achieved using transfer onto a manipulable substrate, nanoscale rippling techniques require growth onto a pre-rippled substrate (such as rippled SiO₂ [83]) or nanoscale lithography techniques (such as ion milling [87]). Further information about fabrication for quantum confinement in two-dimensional materials may be found in a recent review by Stanford and co-authors [88].

Piezoelectricity has also risen as an alternate power generation application for two-dimensional materials, opening the door to port device concepts pioneered as microelectromechanical systems (MEMS) to nanoelectromechanical systems (NEMS) embodiments. According to Chandratre and Sharma, graphene is non-piezoelectric due to its centrosymmetric crystal structure. In order to become piezoelectric, graphene must be in an insulating or semi-conducting state. By considering a variety of non-symmetric holes in graphene, they induce piezoelectricity [89]. Zhu and co-authors analyzed the piezoelectric effect in MoS₂ by measuring piezoelectrically-generated membrane stress combined with a laterally-applied electric field and nanoindentation (AFM) [90]. They conclude that a piezoelectric effect in MoS₂ is only achievable with an odd number of layers. Interestingly, they also found that MoS₂'s piezoelectricity exhibits angular dependence, which

could potentially be applied to determine orientation of the crystals. These results, however, warrant skepticism given the fact that authors appeared to ignore noisy data. Given that electronic properties and small size are what has made graphene such a worthy area of research, the ability of piezoelectricity to combine its electrical properties with its size makes it a worthy area of research for applications such as flexible electronics and nanodevices which can be actuated.

Inducing superlubricity, a regime of near-frictionless motion between two solid-state surfaces, has been shown to be possible with graphite and MoS₂. The regime has been demonstrated computationally [91, 92], and empirically observed coefficients of friction on the order of 10^{-4} have been reported [93, 94]. Superlubricity is highly sensitive to imperfect experimental setups, suggesting that it may not be easily scalable for mass-manufacturing. However, Liang’s early work using sliding HOPG rollers refers to the glissile motion of graphene planes under sufficient pressure and shear stress [2]. Their promising results suggest that exploitation of this phenomena by treating two-dimensional material manufacturing like the manufacturing of non-Newtonian fluids (shear-thinning) could prove fruitful, and their subsequent work on nanoimprint-assisted shear exfoliation shows preliminary evidence that clever manipulation of shear could push two-dimensional material production towards manufacturing scale. Of course, achieving superlubricity in ambient conditions would also enable new device concepts.

1.4 Analysis and conclusions

We emphasize two takeaways regarding the state of investigation into scalable manufacture of van der Waals materials. First, we identify several paradigms which have not previously been highlighted. We believe that naming and questioning these paradigms and their origins could yield fruitful new approaches to mass-manufacturing van der Waals materials. Second, we note the *ad hoc* approach to mechanical manipulation, wherein experiments largely lead theory.

1.4.1 Paradigms in two-dimensional material production

Some assumptions undergird popular thinking within the community of two-dimensional materials researchers. It is widely held that exfoliation-style production methods are inherently incapable of achieving scalability; thus, synthesis methods (primarily CVD and its variants) will be the manufacturing route for mass-implementation of two-dimensional materials. A more subtle assumption is that monolayer devices will be fabricated from monolayer growths. In a research setting, where the absolute time cost is low because of the small number of devices being fabricated, the long growth times required for high-quality monolayer material (~ 26 hours, for MoS₂) are acceptable. However, this approach does not scale favorably. While the CVD research community works to devise improved growth processes that more rapidly deliver high quality material, other approaches may be

viable. Van der Waals epitaxy has been demonstrated as a viable alternative for growth of a given two-dimensional material on a different two-dimensional material substrate [95, 96, 97, 98]; it is reasonable to expect such an approach to be capable of generating multilayers of a single material, given an initial layer. If such a process achieved true epitaxy, then an initial investment layer, requiring long growth time, could be used as a template for rapid growth of additional layers, driving down the marginal time cost per layer. In tandem with a monolayer-selective transfer process, such an approach could offer significantly higher throughput than a process which uses a separate monolayer growth for each set of devices. Of course, issues of yield and transferred material quality must be considered.

Moving past this paradigm sheds light on other manufacturing paradigms woven into the literature: for instance, devices that are arrayed on the final substrate often occupied the same relative positions on their initial substrate, and were transferred *en masse*. Heterostructure fabrication deviates from this paradigm, in that different materials must be picked up from different initial substrates. An alternative would be the patterning of a single, multi-layer region on an initial stack of material, from which (patterned) layers were sequentially removed and placed in the correct position on a target substrate. Monolayer-selective processes are required in order to imagine such an approach; these exist, albeit not for patterned material, a deficit which is addressed in Chapter 2.

Finally, plasma treatment is used nearly universally to enhance adhesion between a van der Waals material and a SiO₂/Si substrate. However, the low adhesion energy between SiO₂ and TMDCs means yield still suffers due to substrate adhesion. Devising alternate means of fixing the transferred layers without interfering with their functional (*e.g.*, electrical or optical) properties could prove a fruitful area for exploration towards improving transfer yield.

1.4.2 The need to augment mechanical understanding

Critical understanding and technology around manipulation of high aspect ratio, flexible, atomically thin films is largely missing. The metal-assisted exfoliation technique, discussed in Section 1.2.2, was pioneered experimentally and later followed by attempts at theoretical explanation. The lack of conceptual understanding makes it difficult to contextualize results; entire spaces may be un(der)explored because we lack a theoretical framework to guide us there. For instance, a robust understanding of how shear strain is transmitted between layers could have directed work into metal-assisted exfoliation, as the particular affinity between gold and sulfur has long been known (*e.g.* [99], further detail in [100]). Instead, empirical observation of alignment of Au nanowires on a TMD surface [101] prompted investigation [65] and reduction to practice [11] of metal-assisted exfoliation for TMDs.

Theoretical understanding that could inform manufacturing practices is nascent. Empirical observation has been used to derive some physical understanding. Hoffman and Marks used transmission electron microscopy to elucidate slip mechanisms during frac-

ture in MoS₂, confirming physical intuition that failure, or fracture, occurs at the weakest interface between layers [102]. Because no naturally-occurring multilayer source is composed of perfectly aligned layers, this mechanism could override more subtle physics that dominate in an ideal stacking scenario. Moreover, they were able to use this observation to establish a hierarchy of weak interfaces. While useful, such an insight did not lead to an analytical model. In a similar manner, Shim and co-authors exploit the weakest-interface approach to create their “layer-resolved splitting” technique, a spalling-esque method, and use a cursory surface energy analysis to explain their process for large-area film delamination [13]. It is unclear whether they used the energy analysis as a design tool, especially given their use of nickel as a “nanoscale adhesive” in previous work on other two-dimensional materials. In other cases, empirically-derived design guidelines have not held up in later experiments. Chen and co-authors, the creators of nanoimprint-assisted shear exfoliation, posited a critical aspect ratio between thickness and lateral dimension of $1:47\pm 30$. At a minimum of this large range, this means monolayer features produced by exfoliation may be at largest 50 nm across. They argue this rule “can serve as a generic methodology for determining the critical aspect ratios of various layered materials generated via different exfoliation methods.” Underpinning their analysis is the assumption that exfoliation techniques are limited by the rigidity of high aspect ratio features, and the authors fail to account for the possibility of stiffening mechanisms, such as adhesion to a metal film. Gold- and nickel-assisted exfoliation (*e.g.*, [11],[13]) are able to produce much larger monolayer films than predicted by this scaling rule.

Given the low cost of computation, and the maturation of machine learning (ML) methods which take advantage of vast data sets to generate new “ideas,” this lack of physical theory may not preclude the ability to design for nanomanufacture. However, such an approach relies on the existence of sufficient example data for a neural net to ascertain patterns. If examples may be computationally generated, this does not provide a hurdle, though computational generation must rely on some analytical model. Computational examples could come from computationally expensive, first-principles approaches like MD and DFT, then fed into neural nets to amortize the initial cost of the MD/DFT simulations over future “experiments” by using insight gained from the ML model. Where examples must be experimentally generated, however, the volume of data needed to create a useful neural net may be time- and cost-prohibitive.

1.4.3 Final remarks

True nanomanufacturing for arbitrary van der Waals materials is not yet possible. Existing approaches to creating monolayer arrays of van der Waals materials in the lab offer a tradeoff between time, quality, yield, and heterostructure compatibility. Growth methods tend to require long times and produce material of lower quality than non-synthetic material, though this is rapidly changing. Growth methods present restrictions in terms of substrate choice that could limit heterostructure fabrication possibilities, and induce yield loss during transfer steps. Exfoliation methods, meanwhile, currently rely on

a multilayer material source for their high-quality monolayers. While these high-quality bulk sources exist for some materials, not all van der Waals materials of interest are naturally-occurring. Moreover, natural sources may be uneven and difficult to pre-treat for high-yield manufacturing processes. In the future, exfoliation methods could be needed to select monolayers from multilayer growth methods, which may provide advantages in terms of the time needed to grow large amounts of high quality material. In the mean time, there is ample space for enterprising researchers to develop new processes and physically-informed design guidelines to enable eventual high-yield, scalable production of arbitrary van der Waals monolayer patterns.

Chapter 2

**Producing arrays of semiconducting
van der Waals monolayers from bulk**

2.1 Introduction

A current challenge in the processing of 2D materials, or van der Waals (vdW) solids, is the transfer of 2D layers from source crystals and growth substrates onto target substrates. Transfer—as opposed to direct growth and patterning on the target—enables low-temperature processing of the target as well as the use of diverse target materials. These two attributes will allow the assembly of vdW heterostructures to realize devices exploiting the unique properties of vdW materials. However, no effective method exists for transferring regions of monolayer material of controlled shape from a multilayer source. Such a method is introduced here, its use in the spatially-controlled transfer of arrays of single-layer MoS₂ and WS₂ sheets from multilayer crystals onto SiO₂ substrates is demonstrated. These sheets have lateral sizes exceeding 100 μm and are electronically continuous. The method offers a scalable route to parallel manufacturing of complex circuits and devices from vdW materials.

To fabricate multi-material 2D structures through sequential vapor-phase deposition, lithography, and etching steps on a single substrate—as in conventional semiconductor manufacturing—is fraught with difficulties. Firstly, although single-layer vapor-phase deposition techniques such as chemical vapor deposition are now maturing [103, 35], the development of processes to deposit one specific 2D material on top of another, while possible [95, 96], is time-consuming. Continuous layers of uniform thickness may prove impractical to produce because of lattice mismatches or chemical incompatibilities. While some fabrication flows actually exploit selective deposition characteristics to form overlap junctions ($<1 \mu\text{m}$) at pattern edges [104, 98], many applications such as LED displays will demand larger ($\geq 10 \mu\text{m}$) planar junctions between sheets of material. Secondly, when a particular layer of a heterostructure needs to be patterned without destroying those underneath—e.g. to enable electrical contact—extremely high etch selectivity is needed. Thirdly, the high temperatures of typically 400-1000 $^{\circ}\text{C}$ required for vapor-phase deposition [103, 96] impose challenging thermal budgets and preclude the use of polymeric substrates, which are highly desirable for flexible electronics and would truly take advantage of 2D materials’ inherent flexibility [105]. Attention has therefore turned to transfer-based assembly methods. Techniques using the surface tension of liquids to maneuver 2D monolayers into position offer limited spatial precision, are prone to wrinkling and folding [91], and introduce residues at the monolayer—substrate interface [103]. Dry transfer (exfoliation) techniques have harnessed normally-applied [106], shearing [8], and mixed-mode [107] mechanical stresses to separate material from naturally-occurring and synthetic sources. Several of these methods provide some within-layer dimensional precision, but layer thickness selectivity when exfoliating from multi-layer sources has often been limited (Chapter 1, Figure 1.2). Yet atomic monolayers are generally essential, *e.g.* for achieving a direct bandgap in MoS₂ [21, 108]. What is needed is a technique with precision in all three dimensions, that can handle continuous sheets with lateral dimensions of many tens of micrometers or larger. Such large lateral sheet dimensions are needed for at least two possible purposes:

1. to provide material on which can be created integrated circuits with many sub-micron devices in a pre-defined spatial arrangement; or
2. to define the boundaries of, e.g., powerful individual visible light emitters or sensitive detectors requiring dimensions in the tens of microns or larger.

Moreover, a process which simultaneously achieves shape selectivity and monolayer selectivity is desirable for forming arrays of heterostructures, by enabling the deposition of a patterned monolayer array at the final substrate (which may already have patterned monolayer arrays on its surface). Recently, the prospects for monolayer exfoliation to be used as a manufacturing process have improved markedly with the discovery that a thin Au film can be used to mediate the single-step exfoliation of large-area monolayers ($>10^4 \mu\text{m}^2$) from multilayer sources [9, 11]. These works did not achieve precise control of monolayer shape or position (Chapter 1, Figure 1.2), meaning a user was still required to comb over a target substrate for viable material. Recent work leveraging the same principle has demonstrated the transfer of larger-area sheets [13], though subsequent patterning of material deposited on the substrate is necessary to form devices. Although the principles underlying this behavior are just now becoming understood [66, 12, 13], it does point towards the development of exfoliation-based transfer of patterned vdW monolayer materials.

The manufacturing process that introduced here (Figure 2.5, details in Section 2.3.2) uses gold-mediated exfoliation in conjunction with a lithographically patterned handle layer to transfer arrays of monolayer regions with controlled shape, size, and separation. Our approach delivers a far higher areal density of usable, continuous monolayer material than unpatterned exfoliation [12, 9, 11], and does so in predictable relative locations so that arrays of devices can subsequently be created in a systematic way.

2.2 Handle design

Removing a patterned array of van der Waals materials, rather than a single large area (as is typical; *e.g.*, [9, 11]), introduces processing challenges. Pressure-sensitive adhesives, including Scotch[®] tape and thermal release tape, include a layer which flows under pressure to make conformal contact to a surface. When a large region of a van der Waals material is being exfoliated, this conformal contact between the adhesive and the van der Waals layer is ideal. However, the conformal contact presents issues when attempting to exfoliate patterned features from a bulk crystal. The van der Waals layers are sub-nanometer thickness. Features etched only a few layers deep in the material are insufficiently high to prevent the adhesive medium from deforming and contacting unpatterned material under the application of back-pressure (Figure 2.1).

Thus, some means of preventing contact between the adhesive and the unpatterned material must be introduced. Etching deeper trenches into the material, either chemically, by extending the reactive ion etching time during photolithography (Figure 2.2(a));

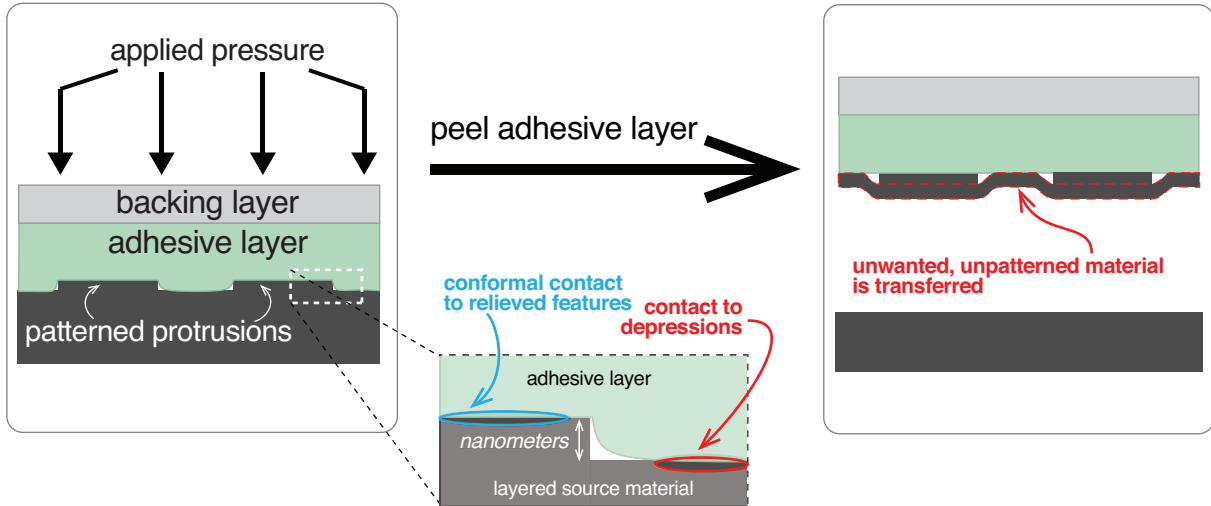


Figure 2.1: When a pressure-sensitive adhesive is brought into conformal contact with a patterned array of features in a van der Waals material, the depth of these features is important. If the features are shallow, the pressure applied to the adhesive will allow it to deform into contact with unpatterned regions, to which it will then adhere.

mechanically, by applying focused ion beam milling (Figure 2.2(c)); or by ablation, using laser energy (Figure 2.2(b)), proved unsuccessful. These methods either achieved too slow an etch time to create sufficiently deep trenches, or, in doing so, oxidized and damaged the material, preventing the exfoliation of a pristine monolayer.

2.2.1 Analytical derivation of handle height

Several authors have tackled the issue of deflection in an elastic stamp leading to undesired contact between stamp and substrate. This concern has been addressed in the context of microcontact printing by Hui and co-authors [109] and in the context of microfluidics by Huang and co-authors [110]. The authors of both papers developed a set of equations governing the out-of-plane deformation of a stamp surface, or roof, across a cavity. This phenomenon is known as “roof collapse”.

The analysis by Hui and co-authors assumes a stamp whose roof and pillars are contiguous and composed of the same material. In the case of a transfer material (stamp) contacting photoresist pillars, the stamp and pillar are dissimilar materials joined by the application of pressure. Moreover, Hui and co-authors’ analysis assumes that the elastomeric stamp is bonded to a stiff (*e.g.*, glass) backing, several orders of magnitude stiffer than the stamp itself, to which pressure is applied. The primary effect of this backplane is to limit and nearly extinguish lateral strain in the stamp due to Poisson’s ratio effects. Thermal release tape is composed of an adhesive layer bonded to a stiff polymeric backing, therefore the calculations from Hui and co-authors may be reasonably applied to the case of thermal release tape. Future stamp designs, potentially composed of elastomeric

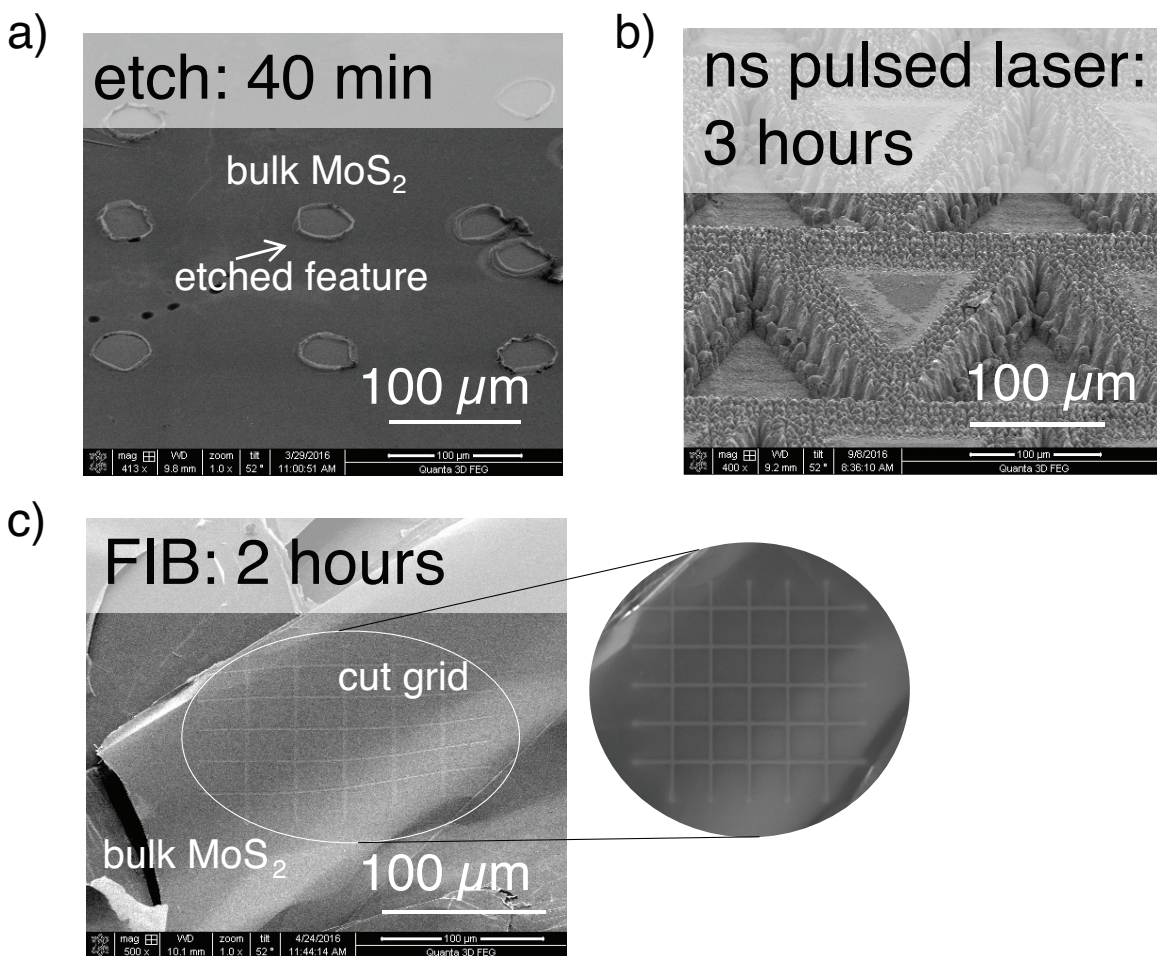


Figure 2.2: Attempts to create microns-deep trenches in bulk MoS₂. a) A CF₄ etch, one of six etch chemistries applied, damages the material to create non-planar sidewalls before a sufficient etch depth is achieved. b) A nanosecond pulsed laser creates deep trenches, but oxidizes the material at the sidewalls, binding the layers together. c) Focused ion beam milling achieves an etch rate below 1 μm per hour.

material, should nonetheless be rigidly bonded to a glass backing in order to ensure even distribution of pressure from a source (*e.g.*, a weight) even when the stamp is affixed to an uneven substrate.

Because purely normal, evenly distributed force is applied at the interface, the nature of the load transfer at the stamp/pillar interface is ignored. Due to the high surface energy of the stamp and its nature as a pressure-sensitive adhesive, the relative lateral position of the stamp and the pillars is assumed to be constant once contact is made. However, compression or buckling of the pillars would limit the safe stamp back-pressure by reducing the distance between the stamp and the substrate (here, unpatterned TMDC material). Because the concern is the behavior of the stamp in compression, the nature of the pillar/substrate binding is momentarily ignored¹.

Since the pillars are a means of contacting and removing the van der Waals layer, they act as a handle between the stamp and the layer. We are concerned with any contact between the stamp and the “substrate”—unpatterned TMDC material, which is not masked by a handle. Incidental between the stamp and unwanted material may result in insufficient binding to remove any material, but even this limited initial contact can be detrimental: the stamp is drawn into a larger contact region by surface forces [111], and can then delaminate and remove large regions. We are interested in finding the condition which assures absolutely no contact between the stamp and the unpatterned TMDC material.

Despite the fact that the stamp is finite in lateral extent, its lateral dimension is much larger than its height. Thus, the stamp/pillar system is treated as an infinite series of equally spaced, collinear gaps, formed by the negative space bounded laterally by the pillar edges and vertically by the stamp and substrate (Figure 2.3). The gaps have width $2w$ (spacing between pillars), spacing $2a$ (width of pillars), and height h (height of pillars). Each gap is considered infinite in depth.

Following the analysis of Hui and co-authors [109] based on Muskhelishvili’s treatment of an infinite series of collinear gaps in an elastic medium [112], the maximum vertical displacement v_{\max} of the roof of a stamp (gap) subject to a far-field compressive stress of σ_{∞} is:

$$v_{\max} = \frac{4\sigma_{\infty}}{\pi E^*} (w + a) \cosh^{-1} \left[\sec \left(\frac{w\pi}{2(w + a)} \right) \right] \quad (2.1)$$

where E^* is the bulk modulus, $E^* = \frac{E}{3(1-2\nu)}$. To ensure this maximum displacement does not reach the substrate, $v_{\max} < h$, thus v_{\max} acts as a lower bound on the height of the offset pillars. The theoretical upper bound is the maximum height under which the pillar is safe from buckling under the given load (see Section 2.2.4). Functionally, a further

¹Eventually, it will be critical that the pillars adhere strongly to the substrate. The crack formed during stamp removal will propagate at the weakest interface; in order to successfully execute monolayer exfoliation, this weakest interface must be between the van der Waals-bonded first and second TMDC layers, rather than between the pillar and the gold, or between the gold and the first TMDC layer.

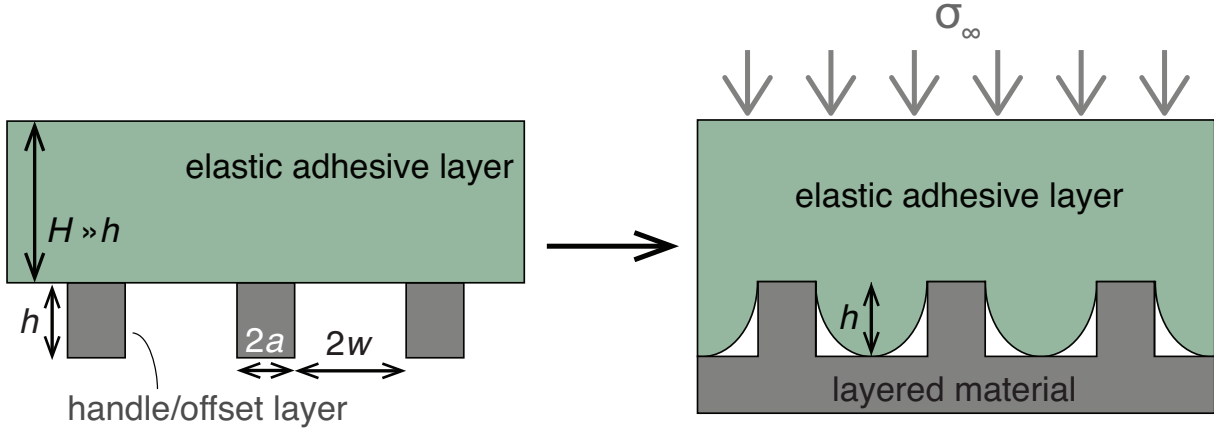


Figure 2.3: Dimensions of the photoresist handle layer are designed to prevent unwanted adhesive contact outside the handles. Dimensions of the handle layer pattern (grey), which could be create using photoresist, and of the transfer medium (thermal release tape), in green, are shown. For a given far-field applied stress σ_∞ , and adhesive layer material properties, a certain minimum height h is needed to prevent unwanted, direct contact between the transfer medium and the unmasked vdW-bonded, layered material.

bound is the manufacturability of a handle of the given aspect ratio, and the processing steps to which the van der Waals flake will be subject during the fabrication of such a handle.

For an exemplar system, we use experimentally relevant values (Table 2.1) to arrive at a necessary offset handle height of $13 \mu\text{m}$. Allowing for a factor of safety and variation in the fabrication process, we seek a process which generates a target handle height of $15 \mu\text{m}$. Such a process is described in 2.3.1.

2.2.2 Contact mechanics confirmation

A contact mechanics approach was used to verify the lower limit on resist height. In this case, the back-pressure on the stamp which would cause the stamp to deflect into contact with the resist was calculated. An existing script determines deformation of elastic bodies in contact with stiff patterned media [113], based on an approach described by Nogi and Kato [17]. The method involves creating an impulse-response kernel for the elastic body which is convolved with the impulse (here, feature) pattern in phase space to determine the elastic deflection at each impulse, and then converted back to real space. In order to confirm the minimum offset feature height required, a stamp deflection profile was prescribed (Figure 2.4(b)) and the stamp average back-pressure causing this deflection was calculated (Figure 2.4(c)).

While the pitch of the features and their spacing match those listed in Table 2.1 used to derive the minimum $13 \mu\text{m}$ handle height, the offset height was set to $15 \mu\text{m}$, the

Table 2.1: Values used for the inputs to Eqn. 2.1, used to calculate the necessary offset height to prevent roof collapse of the stamp.

Quantity	Meaning	Value	Source
σ_∞	Far-field applied stress (<i>i.e.</i> , back-pressure on stamp)	300 kPa	Pressure-sensitive adhesive threshold adhesion pressure
w	Half inter-feature spacing	50 μm	Mask feature spacing
a	Half feature width	20 μm	Mask feature width
E^*	Plane strain modulus of deformable stamp material	3 MPa	Thermal release tape adhesive modulus (measured, Section 2.2.3)
		0.5	Thermal release tape adhesive Poisson's ratio (estimated)

conservative minimum limit on handle height determined in Section 2.2.1. Despite the increased height, the stamp average back-pressure needed to make contact was determined to be 297 kPa—1% lower than the minimum design pressure, indicating that 15 μm is in fact too small a lower bound on handle height. A factor of safety should be added in order to determine a safe lower bound, as the calculation performed here assumed contact between the stamp and the unpatterned material over a width equivalent to the pitch/resolution of the simulation (in this case, 1.25 μm). In a real system, any stamp-material contact should be avoided: in order to minimize surface energy, even minimal contact between the stamp and substrate could pull further stamp material into contact [114], which is undesirable.

2.2.3 Mechanical properties of thermal release tape

The mechanical properties of the adhesive transfer medium are also necessary to determine the correct handle geometry. The thermal release tape operates in two regimes: an adhesive regime, below the release temperature, at which the tape is engineered to behave as a pressure-sensitive elastic solid, and a release regime, in which either activation of foaming agents or heat-induced loss of a plasticizer reduces the adhesion strength of the tape [115]. Because the tape contacts to-be-exfoliated material in its solid, below-release-temperature regime (specifically, at room temperature and pressure), its behavior was characterized at room temperature. While the deformation mechanics of the as-released tape impact the yield of the process—material which is not rejected from the face of the tape is not deposited on the substrate, harming yield—the design of the handle layer depends only on the pre-release properties of the tape.

The modulus of the adhesive face of thermal release tape (Nitto Denko, 160 °C release temperature) was measured in a Hysitron Nanoindenter (TI-950). To attempt to limit adhesion of the surface to the nanoindentation tip, a Kimwipe was applied to the surface and then removed before testing. Forty-eight indentations were performed, and Oliver-Pharr theory [116] was used to extract a reduced modulus of 3 MPa under a maximum applied load of 30 μN . Though the material is nominally an adhesive, there was insufficient evidence of adhesive behavior between the tip and sample to warrant modifying the calculation (for instance, by applying Johnson-Kendall-Roberts theory) to account for adhesion of the tip.

2.2.4 Mechanical properties of photoresist

While the mechanical properties of photoresist as-received are well-documented—notably, viscosity is critical to determine spin rates to achieve a given final thickness—the as-cured properties are not readily available. Thus, the properties of photoresist features were measured using the same Hysitron Nanoindenter used to measure the thermal release tape. Photoresist chevrons (AZ P4620 resist, MicroChemicals GmbH) were fabricated on a glass slide, following the same protocol used to fabricate features on the van der Waals

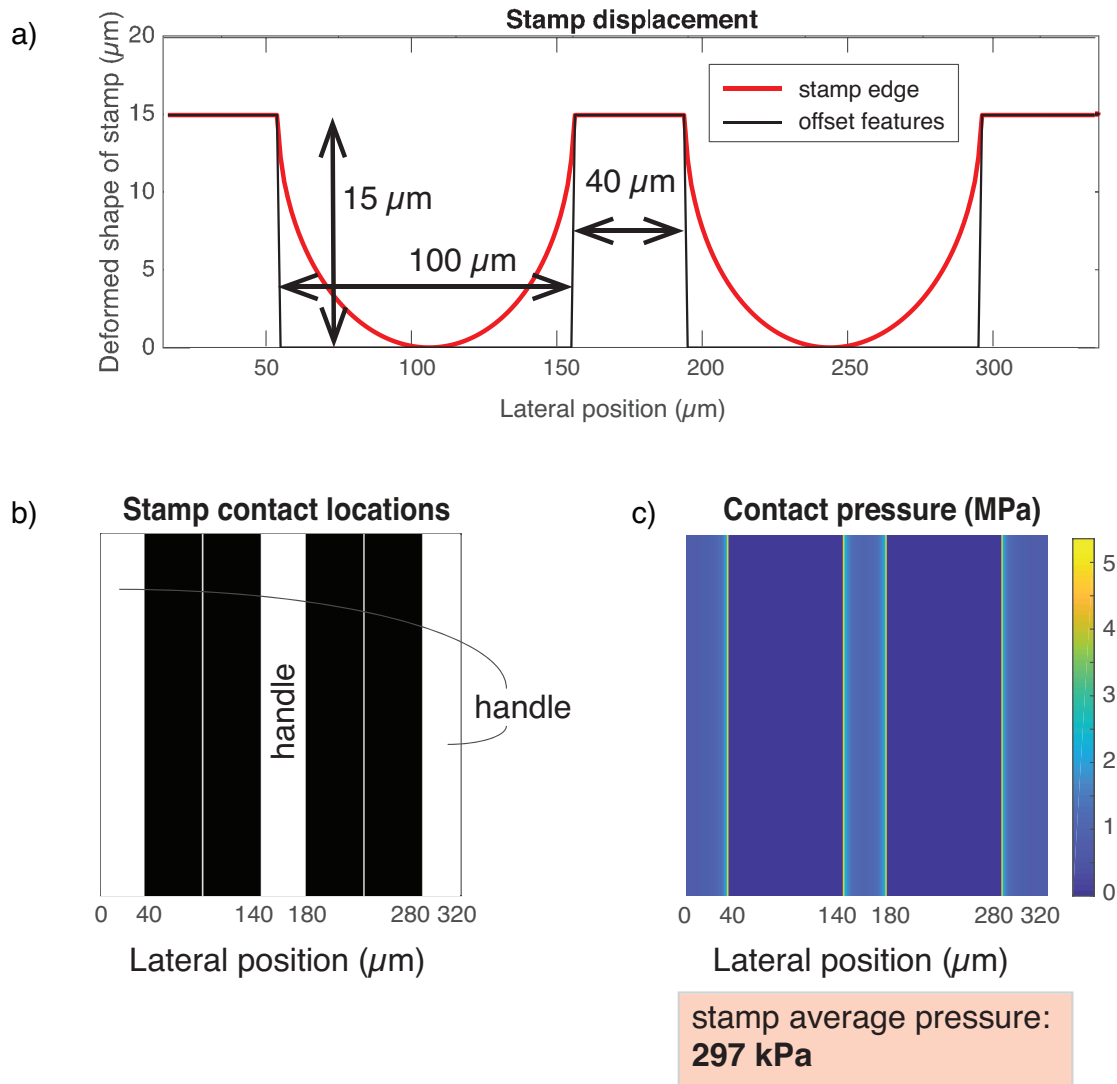


Figure 2.4: Expected stamp deflection under the minimum applied load, calculated by prescribing a stamp deflection and reverse-engineering the pressure needed to cause this deflection using the deformation kernel of stamp (derived from ref. [17]). (a) Stamp deformation profile as a function of lateral position, resulting from the contact regions prescribed, (b) the prescribed locations where contact is made, either between the stamp and the photoresist handles or between the stamp and the layered material's surface, (c) the pressure in the stamp at each location, resulting in an average back pressure of 297 kPa.

flakes (Section 2.3.1). The properties were measured with a conical, 20 μm radius fluid cell tip with a 90° indentation angle (normal indentation). The system was calibrated using 20 kPa agarose gel as a reference.

The measured stiffness of the as-cured photoresist was 40 MPa. The cured photoresist is at least an order of magnitude stiffer than the deformable adhesive on the face of the tape. Under the applied load necessary to ensure adhesion between the tape and the photoresist, the cured photoresist features can be expected to deform 0.75%. With an offset thickness of 15 μm , the total photoresist deformation is 110 nm, which is smaller than the expected variation in the as-spun resist height.

Buckling of tall, thin features is also a concern. Following, again, the math of Hui and co-authors [109], the condition to prevent buckling of features in contact with an elastic stamp is:

$$\frac{12\sigma_\infty h^2}{\pi^2 E_{\text{pillar}}^* a^2} < \frac{1}{1 + w/a}$$

$$h < \sqrt{\frac{\pi^2 E_{\text{pillar}}^* a^2}{12(1 + w/a)\sigma_\infty}} \quad (2.2)$$

For the exemplar system described in Table 2.1, with the measured plane-strain modulus of the resist $E_{\text{pillar}}^* = 40$ MPa, $h < 112$ μm . This threshold is roughly an order of magnitude larger than the desired resist height found using Eqn. 2.1, thus buckling can be safely ignored in resist height design for this system, and higher photoresist features within the range of process variation from the target height are strictly more desirable.

2.3 Methods

2.3.1 Photolithography

In order to generate sufficiently thick handles, a method for generating 15-20 μm thick photoresist features is needed (detailed in Section 2.2.1). A single patterning step was desirable to avoid alignment issues between photoresist exposure rounds. Positive photoresist was chosen for its ability to create thick features, and a recipe was developed which produced a sufficiently thick handle layer and was able to achieve complete pattern transfer into the resist without overexposure, which would result in incorrect feature sizes.

Spin speeds and times used are given in Table 2.2. The resist was baked at 110 °C for three minutes following each spin. The resist was exposed with a chrome/glass contact transparency mask for 10 seconds at approximately 20 mW/cm² and subsequently developed for at least four minutes in AZ 400K developer pre-diluted 1:3 with deionized water. During development, the bath was agitated at approximately 1 Hz. The sample was then removed from the developer bath and placed immediately in a bath of DI water

Table 2.2: Photoresist spin parameters to achieve a 15 $\mu\text{m}+$ thickness, photo-patternable layer using AZ P4620.

	Ramp 1	Speed 1	Time 1	Ramp 2	Speed 2	Time 2
Spin 1	100 rpm/s	500 rpm	10 s	500 rpm/s	2400 rpm	60 s
Spin 2	100 rpm/s	500 rpm	10 s	500 rpm/s	1600 rpm	60 s

(room temperature), then rinsed under a stream of DI water and blown dry using N_2 . The results of the photolithography were verified optically: in the case of insufficient photoresist development, the sample was placed in a new bath of AZ 400K developer.

2.3.2 Process flow

The entire process developed for generating patterned arrays of TMDC monolayers on an SiO_2 substrate is as follows (shown in Figure 2.5):

1. The multilayer source material (in this work, MoS_2 or WS_2) is prepared. The flattest available sections of material are used. In the case of MoS_2 , natural, mined crystals were obtained (eBay) and were manually cleaved to create a flake several mm in diameter and a fraction of a millimeter thick. Both WS_2 and additional MoS_2 samples were obtained as a multi-layer sample fabricated by chemical vapor transport (CVT), $\sim 0.2\text{-}0.3$ mm thick (HQ Graphene). Using CVT sources, source flakes were manually separated to create child flakes for processing. In either case, the flake was mounted to a glass slide using double-sided Kapton tape for subsequent processing. The prepared source material is coated with a 100 nm-thick layer of gold (Kurt Lesker, Inc.) by thermal evaporation (Torr International, Inc.).
2. The source material is coated with AZ 4620 photoresist (MicroChemicals GmbH) which is then patterned (details in Section 2.3.1).
3. Without removing the photoresist layer, the exposed gold is etched for 1 minute in KI/I_2 (Gold Etchant TFA, Transene Company, Inc.; used undiluted). This step exposes the MoS_2 or WS_2 that is not to be transferred, while the to-be-transferred material remains masked by gold and photoresist. The sample is rinsed in DI water.
4. The patterned flake is then exposed to a 30-second etch in CF_4 plasma (20 sccm, 100 W, Plasma Equipment Technical Services, Inc.) to remove at least one atomic layer of the MoS_2 or WS_2 from unmasked regions. Initially, a one minute etch time was used to ensure the removal of the top layer (per [117]); however, the longer etch time was correlated with large amounts of organic residue on the sample, and was adjusted down. As an alternative to a plasma etch, an argon ion milling step may be used².

²Ion milling (Pi Scientific 6" system) was conducted using Argon ion (5 sccm RF neutral, 15 sccm ion

5. Thermal release tape (REVALPHA, Nitto) is brought into contact with the remaining photoresist pattern. Light manual pressure is applied by brushing rubber-tipped tweezers against the back side of the tape, and the tape, loaded now with the pattern, is peeled by hand from the bulk flake. The peeling rate has a considerable observable impact on yield, which merits further investigation in the context of patterned peeling. A more rapid peel rate results in many more removed monolayers, which is desirable. A similar effect has been reported and studied elsewhere (*e.g.*, [118]).
6. The silicon wafer target substrate with 260 nm silicon oxide is treated in O₂ plasma for 5 minutes (120 W, Diener Electronic Nano). It is then placed on a hot plate at 80 °C for at least five minutes, where an infrared gun is used to verify the substrate has reached 80 °C. The tape, loaded with the patterned material, is placed onto the heated target substrate and pressure is applied to the tape/substrate stack for 5 minutes using a 6.8 kg weight atop a rubber stopper (area: 11 cm², thickness: 2.54 cm (1")). The purpose of the rubber is to distribute the load uniformly over the uneven micro-topography of the patterned tape's surface. The applied pressure is approximately 60 kPa.
7. The target substrate, carrying the loaded tape, is moved to a hot plate at 160 °C to trigger the release of the thermal tape. Upon release the tape whitens, indicating the micro-beads embedded in the adhesive have expanded [115]. Shortly (~3 seconds) after the whitening is observed, the tape is removed with tweezers to prevent motion of the tape from removing or damaging transferred features.
8. The transferred stack is now adhered to the silicon/silicon oxide substrate and is placed in room temperature acetone for at least four hours to remove the photoresist.
9. Because the photoresist was exposed to a fluorinated etch, some organic material typically remains after the acetone exposure. Thus the substrate is ashed in O₂ plasma (3 minutes, 20 sccm, 300 W, Plasma Equipment Technical Services, Inc.) to remove any organic residue on the surface. During the ashing step, the remaining gold layer protects underlying MoS₂ or WS₂ monolayers from damage or removal.
10. Finally, the remaining gold is stripped in KI/I₂ (1 minute, room temperature) and the sample is rinsed in DI water³. The result is monolayer TMDC material on the

source), with 100 mA beam current, 500 V beam voltage and 20 degree incidence angle. The duration of the mill was 7 minutes and the pressure was 1.9×10^{-4} Torr.

³It is critical the liquid processing is carried out immediately following O₂ plasma exposure. Plasma treatment renders the SiO₂ surface temporarily hydrophilic. Absent this hydrophilicity, monolayers on the surface are removed or severely damaged during liquid processing. One possibility is that liquid atop the monolayers beads at the edges because it is not energetically favorable to contact the less-hydrophilic SiO₂ surface next to the monolayers. The weak bond between the SiO₂ substrate and the monolayer could be decoupled by the surface tension of the droplet, peeling the monolayer away from the substrate and flushing the monolayer when the substrate is rinsed.

silicon/silicon oxide substrate.

2.3.3 Device fabrication

Back-gated MOSFET devices were fabricated using transferred material. The transferred monolayer material was used as the channel, evaporated nickel electrodes served as source and drain contacts, and the p-type silicon substrate and SiO₂ functioned as a back gate and a gate dielectric, respectively. Source and drain electrode geometries separated by 10 μm -long channels were defined via photolithography using AZ 4620 photoresist (MicroChem), or using LOR/i-line resist (MicroChem) patterned by electron-beam lithography, followed by 40 nm of nickel evaporation and liftoff of the underlying photoresist in acetone (for AZ 4620) or Remover PG (MicroChem, for LOR). Several devices patterned on one monolayer of MoS₂ are shown in Figure 2.6(a).

2.4 Results

2.4.1 Optical and optoelectronic characterization

White light optical reflection micrographs, recorded using standard laboratory microscopes, are commonly used to identify monolayers and few-layer regions of van der Waals materials on silicon wafers. By depositing an oxide with a thickness engineered to maximize contrast with single-layer material, van der Waals material locations and thicknesses can be determined with high fidelity [119, 120]. These observations may be confirmed using optoelectronic methods, including photoluminescence spectroscopy, which is particularly sensitive to the difference between monolayer and multi-layer material, and Raman spectroscopy. These measurements also provide insight about the quality of the transferred material.

Monolayer regions within an array of ≥ 100 transferred WS₂ features are identified from white-light optical reflection micrographs (Figure 2.7(a)).

These micrographs show that features printed using the method are predominantly composed of monolayer material and include substantial continuous monolayer areas. The monolayer nature of these regions is confirmed with photoluminescence imaging [21, 108] (WS₂: Figure 2.7(b); MoS₂: Figure 2.8(b)). The optical micrographs are then used to calculate yield, using approaches detailed in Section 2.4.3.

Photoluminescence spectroscopy

Because MoS₂ and WS₂ possess a direct bandgap only as atomic monolayers[21] (where each monolayer is composed of three covalently-bonded chalcogen-metal-chalcogen layers), techniques which leverage this direct band gap are a simple assessment of whether the

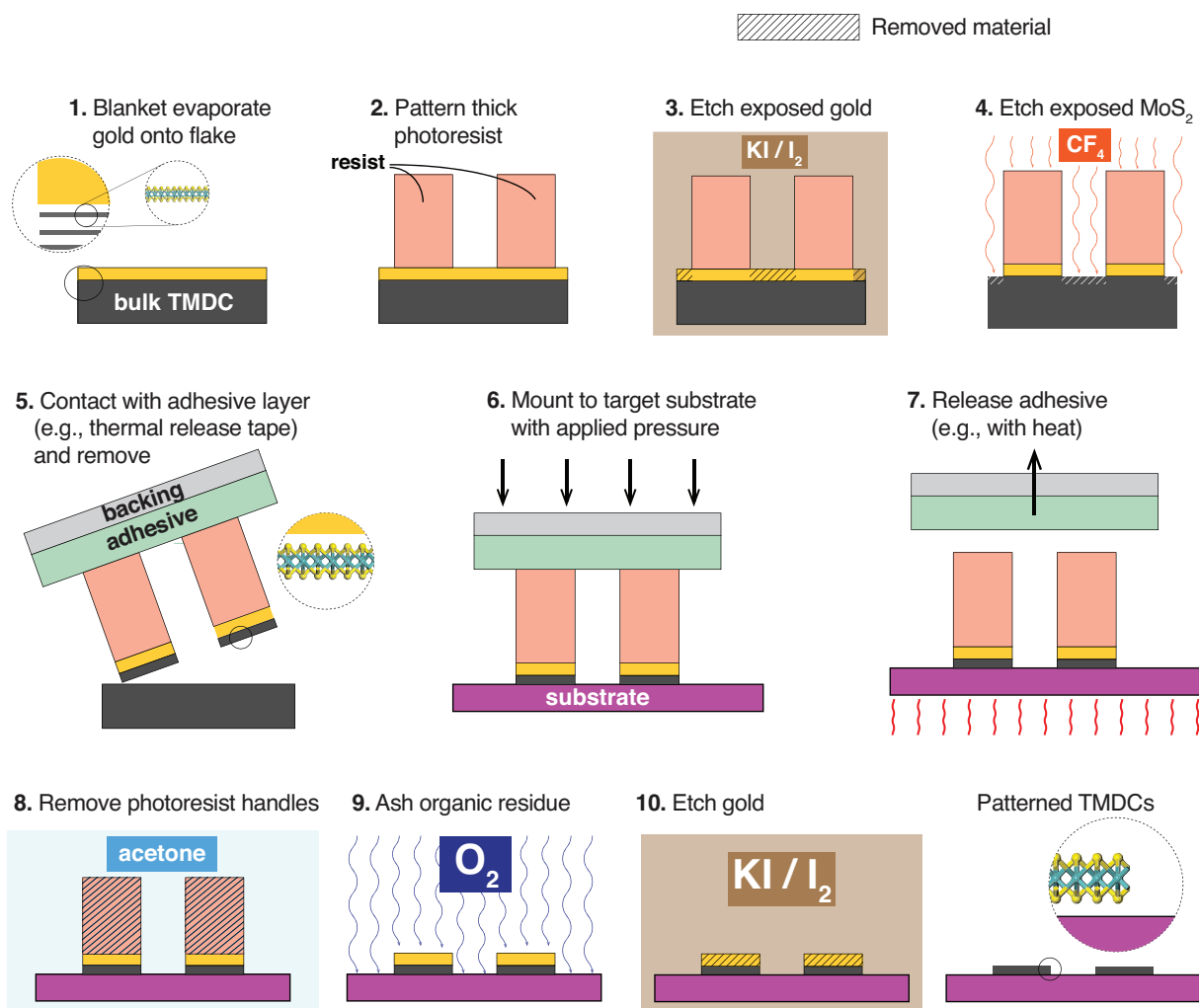


Figure 2.5: The process for producing patterned van der Waals monolayers. The process uses standard photolithography techniques. It relies on the use of a thick handle layer (here, photoresist, in step 2) to pattern the gold and the underlying layered bulk material, as well as to offset the adhesive transfer medium from the bulk, thus permitting transfer of only the patterned regions.

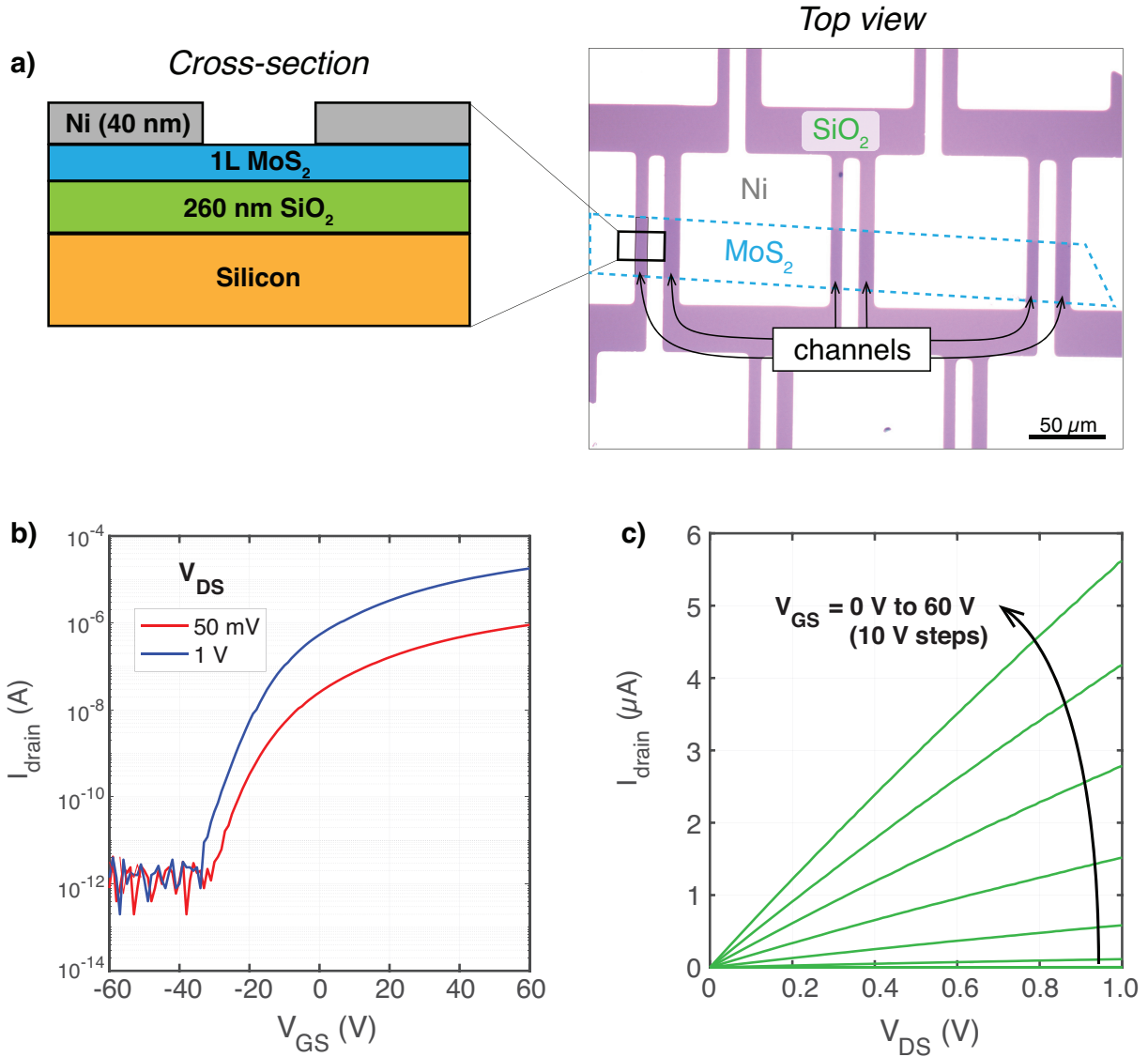


Figure 2.6: (a) Cross-section and optical micrograph of six fabricated back-gated MoS₂ transistors with channel width up to 40 μm, defined by the patterning process, and a gate length of 10 μm defined by the Ni contacts. (b) Switching behavior of one of the devices fabricated from transferred monolayer MoS₂ material. (c) Drain current as a function of drain-source bias, measured at eight gate-source biases, up to 60 V, on a single 10 μm gate length monolayer MoS₂ transistor. The device did not enter saturation mode at any gate-source bias tested. These curves are representative of all transistors measured, using both MoS₂ and WS₂ as channel materials; all exhibited only linear behavior.

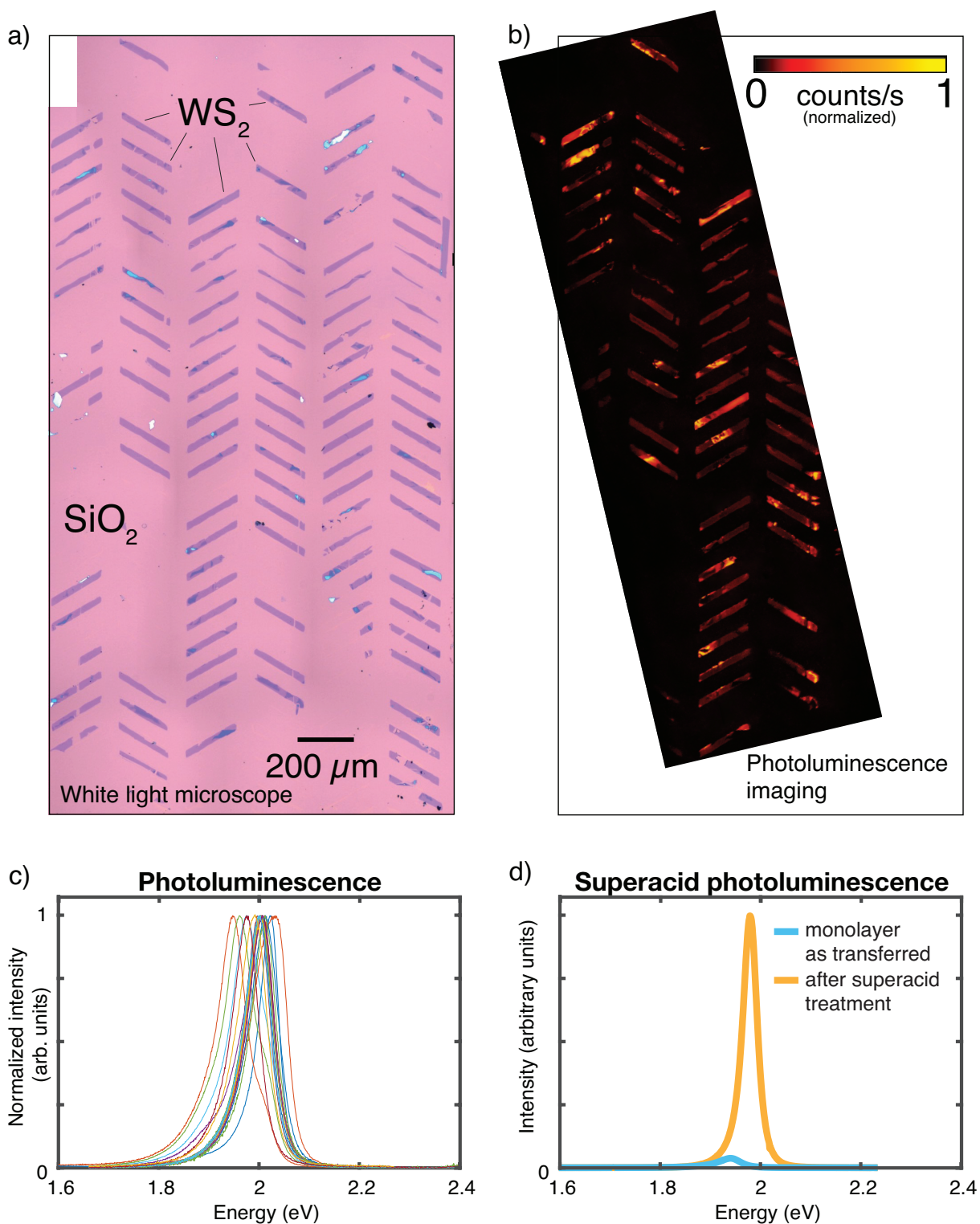


Figure 2.7: Optical and optoelectronic WS₂ monolayer characterization. (a) White-light reflectance image of a set of transferred WS₂ features on 260 nm thermal SiO₂ on Si; (b) photoluminescence image of part of the same region as in (a): orientation is the same as (a), and the outline corresponds to that of the region imaged in (a); (c) photoluminescence spectra from 13 regions of WS₂ on 260 nm thermal SiO₂ on Si, confirming that monolayer WS₂ has been transferred to the substrate; (d) the result of treating a WS₂ monolayer with a superacid, showing more than a twenty five-fold increase in quantum efficiency.

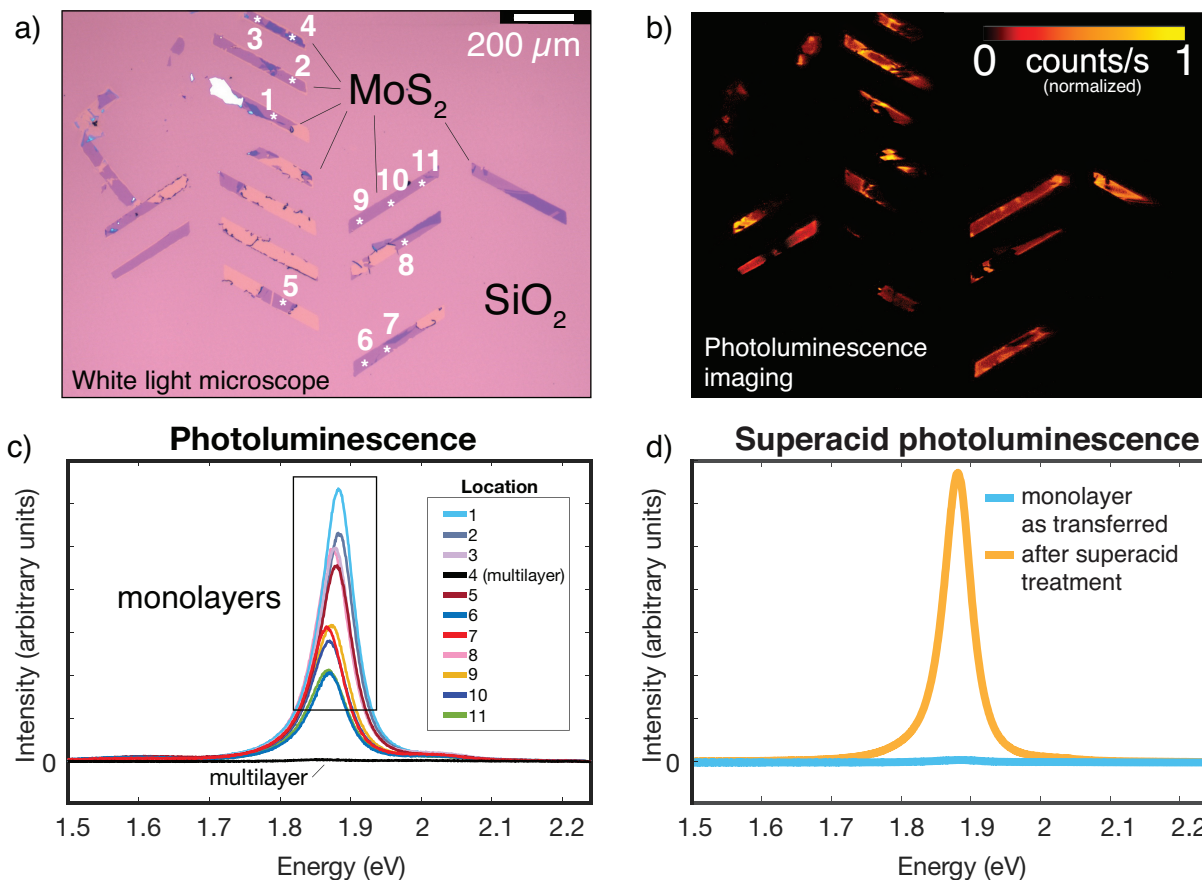


Figure 2.8: Optical and optoelectronic MoS₂ monolayer characterization. (a) White-light reflectance image of a set of transferred MoS₂ features on 260 nm thermal SiO₂ on Si; (b) photoluminescence image of the region; (c) photoluminescence spectra associated with the numbered locations in (a), confirming that monolayer MoS₂ has been transferred to the substrate; (d) the results of treating MoS₂ monolayers with a superacid, showing more than a one hundred-fold increase in quantum efficiency.

material present is a single monolayer. Thus photoluminescence measurements allow rapid differentiation of monolayer MoS₂ and WS₂ from their bi- and multilayer counterparts.

Photoluminescence measurements were used both to verify that optically identified monolayer material was, in fact, monolayer in nature, and to rapidly determine the consistency in quality of the transferred material by assessing the variation in quantum yield using wide-field photoluminescence imaging.

Substrates carrying transferred WS₂ or MoS₂ were characterized using photoluminescence spectroscopy in a custom micro-PL system (Lexel 95 argon ion laser, power: 0.35–0.37 μ W; λ : 514.5 nm; NA: 0.8; spot size: 1.1 μ m²; filter: 550 nm long-pass). The power of the excitation beam was calibrated at high illumination intensity using a photodiode power meter (ThorLabs S120C). For the duration of the measurement, the excitation beam power was found to be 20 times the incident power on the sample. For PL spectra collection, the laser beam was focused onto the sample using a 50x objective lens (NA = 0.8) which resulted in a measured spot size of 1.1 μ m² full-width half-maximum. PL imaging data were collected through a 10x objective lens (NA = 0.3) using excitation from a GaInN LED (λ : 450 nm, power: 170 μ W at sample) with the illumination distributed over a spot of diameter 1.8 mm, giving a power density of 65 μ W/mm². Outgoing counts from the samples were collected through same microscope objective, passed through a 550 nm dielectric long-pass filter to remove the excitation signal, dispersed by an $f = 340$ mm spectrometer with a 150 g/mm grating, and detected by a Si CCD camera (Andor iDus BEX2-DD). Prior to measurements, the entrance slit of the spectrometer was opened until the maximum number of PL counts was obtained. The CCD background was obtained by collecting a spectrum before each measurement, over the same integration time as the eventual measurement, without the laser on. The background was subsequently subtracted from the PL spectra.

The measured PL spectra from the 13 measured locations on WS₂ have peak energies with a mean of 2.00 eV and a standard deviation of 0.021 eV. The PL spectra for WS₂ are shown in Figure 2.7(c). The peak energies are assumed to correspond to the optical bandgap of the material. The observed bandgap non-uniformity of barely 1% of the mean indicates that the material could be usable for constructing complex circuits with consistent performance across many devices. A two-tailed t -test assuming the measured bandgaps to be normally distributed finds that the optical bandgap of the transferred monolayer material is significantly lower ($p < 0.00025$) than the theoretically predicted value [121] of 2.03 eV for an unstrained, isolated monolayer. This slight red-shift is consistent with the effect of the proximity of a SiOx substrate as reported previously [122], or with residual strain induced otherwise in the material [123]. For the MoS₂ samples, meanwhile, PL spectra are illustrated in Figure 2.8(c), and the ten measured monolayer regions yield a mean peak energy of 1.875 eV with a standard deviation of 0.006 eV. As in the case of the transferred WS₂ monolayers, a two-tailed t -test finds that the optical bandgap of the transferred monolayer material is significantly lower ($p < 0.03$) than the theoretically predicted value [121] of 1.88 eV for an unstrained, isolated monolayer. Those regions with any detectable PL signal in PL images (Figures 2.7(b) and

Table 2.3: Raman characteristics of mono- and bilayer MoS₂ and WS₂, from ref. [18]. All entries in units of cm⁻¹ unless noted otherwise.

	Monolayer (1L)			Bilayer (2L)			Sensitivity to thickness difference $\Delta_{1L \rightarrow 2L}$
	E _{2g}	A _{1g}	Difference	E _{2g}	A _{1g}	Difference	
WS₂	356	418	62	355	419	64	3%
MoS₂	385	403	18	383	405	22	22%

2.8(b)) correspond to regions identified from the associated white light reflectance images as containing monolayer material. Thus, although spatial uniformity of the imaged PL within monolayer regions is variable, the observation of PL is a reliable indicator that monolayer material is present.

Samples were treated in bis(trifluoromethane) sulfonimide (TFSI) superacid to determine whether this method could improve the quantum yield, as demonstrated previously for transition metal dichalcogenide monolayers [124]. The chip carrying the samples was treated in a 0.2 mg/mL solution of TFSI, in a mixture composed of dichloroethane and dichlorobenzene in a 10:9 ratio. The chip was submerged in this solution for 10 minutes at room temperature, then removed and dried with a jet of N₂. The superacid treatment increased the quantum yield by at least 25x in the case of WS₂, and at least 100x in the case of MoS₂, as evidenced by the large increases in PL intensity in response to equivalent illumination intensities: results are shown in Figure 2.7(d) (WS₂) and Figure 2.8(d) (MoS₂).

Raman spectroscopy

Raman spectroscopy measurements were performed at 20x and 50x magnification in a Renishaw Raman system (λ : 488 nm, power: 1 mW at sample (50x), spot size: 1 μ m diameter, grating: 2400/mm). In order to characterize large areas, Raman maps were constructed by collecting spectra at each point on a user-specified grid. The grid pitch varied based on magnification and the size of the area of interest. Raman maps and spectra on monolayer MoS₂ and WS₂ are shown in Figures 2.9 and 2.10, respectively. The E_{2g} and A_{1g} peaks were identified using a custom MATLAB script, and the difference in Raman shift between peaks (in units of cm⁻¹) was used to verify material thickness [18]. The Raman results were compared to photoluminescence spectra and images to ensure that both measurements indicated monolayer material in the same locations. The expected inter-peak differences as a function of thickness and material are given in Table 2.3, using data from ref. [18].

Though Raman peak shifts are most pronounced in the transition between one (1L) and two (2L) layers of a TMDC (as opposed to, say, between two and three layers), the total detectable change in inter-peak shift (combining the redshift of the E_{2g} peak and the blueshift of the A_{1g} peak) is only 3% in WS₂. There is no appreciable difference in intensity of the peaks between different thicknesses. Photoluminescence measurements,

MoS₂

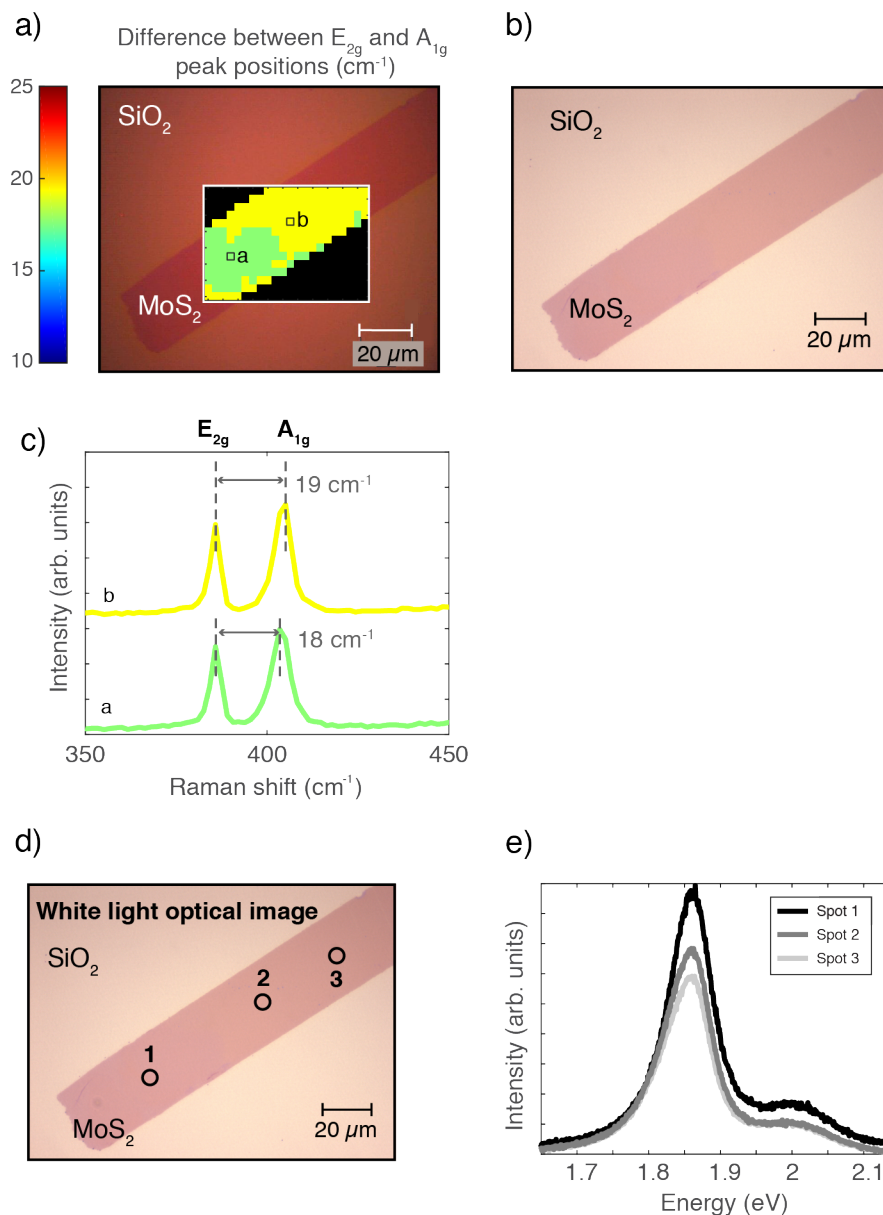


Figure 2.9: (a) Raman map of the E_{2g} and A_{1g} peak separation, indicative of material thickness, over a monolayer chevron of transferred MoS₂. (b) Optical image of the region measured in (a). (c) Spectra from two different regions, *a* and *b*, labeled in the map, showing two inter-peak differences below the expected bilayer peak difference of 22 cm^{-1} . (d) Optical image of the feature mapped with Raman spectroscopy in (a), with points labeled whose photoluminescence spectra were measured. (e) Unnormalized photoluminescence spectra from the three points labeled in (d).

WS₂

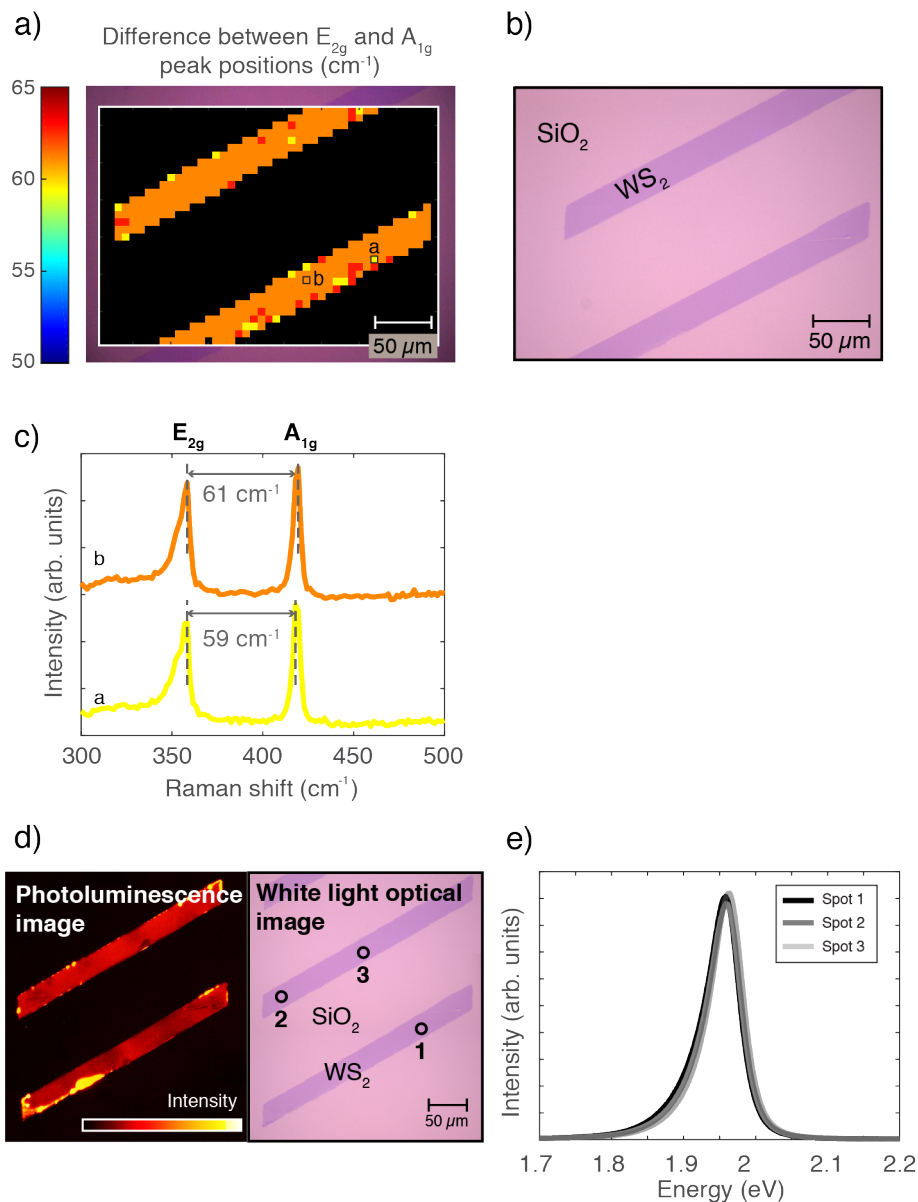


Figure 2.10: (a) Raman map of the E_{2g} and A_{1g} peak separation, indicative of material thickness, over two monolayer chevrons of transferred WS₂. The extent of the map scale is the same as in Figure 2.9. (b) Optical image of the region measured in (a). (c) Spectra from three different regions, *a*, *b*, and *c*, labeled in the map, showing inter-peak differences below the expected bilayer peak difference of 64 cm⁻¹. (d) Photoluminescence image (left) and optical image (right) of the same features mapped with Raman spectroscopy in (a). The readily observed luminescence across both features indicates their monolayer composition. (e) Unnormalized photoluminescence spectra from the three points labeled in (d), showing the consistent luminescence across the features.

on the other hand, offer an orders-of-magnitude difference in intensity between 1L and 2L, with negligible differences in intensity from 2L to 3L and upwards. Thus, PL is a more robust and rapid means of differentiating 1L from 2L.

2.4.2 Electrical characterization

A current issue with mass-produced transistors is excessive power lost to leakage current, a result of electron migration across the extremely small source-drain distance [125, 126]. The leakage current is a function of the electron effective mass of the semiconducting material. Higher effective masses make it more difficult for electrons to travel; commercial transistors use silicon as the semiconducting medium, with a transverse electron effective mass of $0.19m_0$, where m_0 is the free electron mass. Straining the silicon drives down the effective mass, by as much as 80% [127]. By contrast, monolayer molybdenum disulfide has an electron effective mass (along the transport direction) of $0.5m_0$ [128]. Between gate lengths of 3-6 nm, the expected leakage current in monolayer MoS₂ channels is at least six orders of magnitude smaller than the leakage current expected in silicon of a similar thickness [129]. This improved leakage current comes at the expense of mobility: devices made on silicon will switch more quickly than devices made on MoS₂.

Though monolayer TMDCs are unlikely to see adoption in industrial transistors, switching devices are nonetheless useful for assessing the quality of the transferred material: long channel lengths give a statistical aggregation of whether the material has undergone damage in the transfer process. Mechanical damage is a particular concern: previous efforts to remove large monolayers using gold-assisted exfoliation resulted in monolayers with considerable microcracking that rendered several device sites non-functional. Moreover, switching devices are straightforward to produce, requiring only the addition of source and drain contacts (the existing silicon/silicon oxide substrate provides both gate and gate oxide, respectively). Fabrication details may be found in Section section 2.3.3.

A total of 20 devices with functional monolayer MoS₂ channels were measured (Agilent 4155C Semiconductor Parameter Analyzer; Everbeing probe station and chamber) on two separate substrates.

Monolayer MoS₂ is intrinsically *n*-type⁴ [14, 130], as is WS₂ [131]. WSe₂, meanwhile, is *p*-type [132]. (While WSe₂ devices were not fabricated in this work, precedent work [11] implies that a similar method could be applied to WSe₂ exfoliation.) The availability of *n*-type and *p*-type monolayers is promising for the prospect of building *p-n* junctions and CMOS devices.

I_D - V_{GS} characteristics of the MoS₂ devices are shown in Fig 2.11. The average characteristics of devices differ between the two chips: on Chip 1, the on/off current ratio

⁴The structure and doping of the substrate, as well as the nature of the substrate-monolayer interface, play heavily into the apparent doping of the monolayer (whose mass is entirely at its surface). Modifying an SiO₂ substrate with dangling oxygen bonds, for instance, can shift monolayer MoS₂ to *p*-type [130]. This may be useful for single-substrate CMOS device fabrication, if substrate modification can be sufficiently localized. To our knowledge, this concept has not been implemented in practice.

is between 10^4 and 10^6 at the smaller V_{DS} of 50 mV, rising to between 10^5 and 10^7 at $V_{DS} = 1$ V. In Chip 2, however, the corresponding on/off current ratios are between 10^2 and 10^4 at $V_{DS} = 50$ mV, and between 10^3 and 10^5 at $V_{DS} = 1$ V. The fact that there is greater consistency between devices on a given substrate than between the devices on different substrates indicates the possibility of substantial property differences between mined molybdenite crystal specimens. Equally, the differences may result from substrate-to-substrate variability in the transfer process.

Switching characteristics of six WS_2 monolayer devices on a single substrate are shown in Figure 2.12. At $V_{DS} = 50$ mV, the on/off current ratio is at most 10^2 , while at $V_{DS} = 1$ V, the ratio is $\sim 10^3$ to 10^5 .

The devices operate in linear mode up to $V_{GS} = 60$ V (larger values of V_{GS} were not tested). A characteristic I_D - V_{DS} plot, measured on a monolayer MoS_2 device, is shown in Figure 2.6(d).

These back-gated FETs exhibit I_D - V_{GS} characteristics confirming that electrical continuity and semiconducting performance of the monolayers are maintained through the manufacturing process. All devices tested on monolayer material demonstrate switching behavior.

2.4.3 Yield characterization

Yield metrics for nanomanufacturing of van der Waals patterns

To our knowledge, there are no established methods for assessing the yield of an atomic monolayer production process. Thus, two metrics are introduced which capture aspects of the transferred material that are relevant to production at scale: feature yield, and area yield (Figure 2.13). Feature yield refers to the number of features transferred with any material, as a proportion of the total number of features that could possibly have been transferred within a selected area. Areal yield measures, for features that were transferred, the amount of monolayer material in a given feature as a proportion of the total intended feature area. The feature yield is calculated by assessing, by eye, from a white-light optical reflection micrograph whether any material is transferred in each intended feature, summing the number of features where material is transferred, and dividing the total by the number of features that could possibly have been transferred in the region defined by the intersection of the reflectance image's field of view with the boundary of the thermal release tape used. The boundary of the tape was always within that of the source material. Thus, the denominator of the feature yield calculation fairly captures the number of features that one could expect to observe in a 'perfect' transfer process. A single percentage yield is reported for a particular substrate. The areal yield for a particular feature is calculated by determining, through image processing, the bounds of any monolayer regions in that feature, and dividing the total area of any such region(s) by the area of the corresponding intended feature on the photomask used for initial patterning. By considering the set of these ratios for all transferred features on

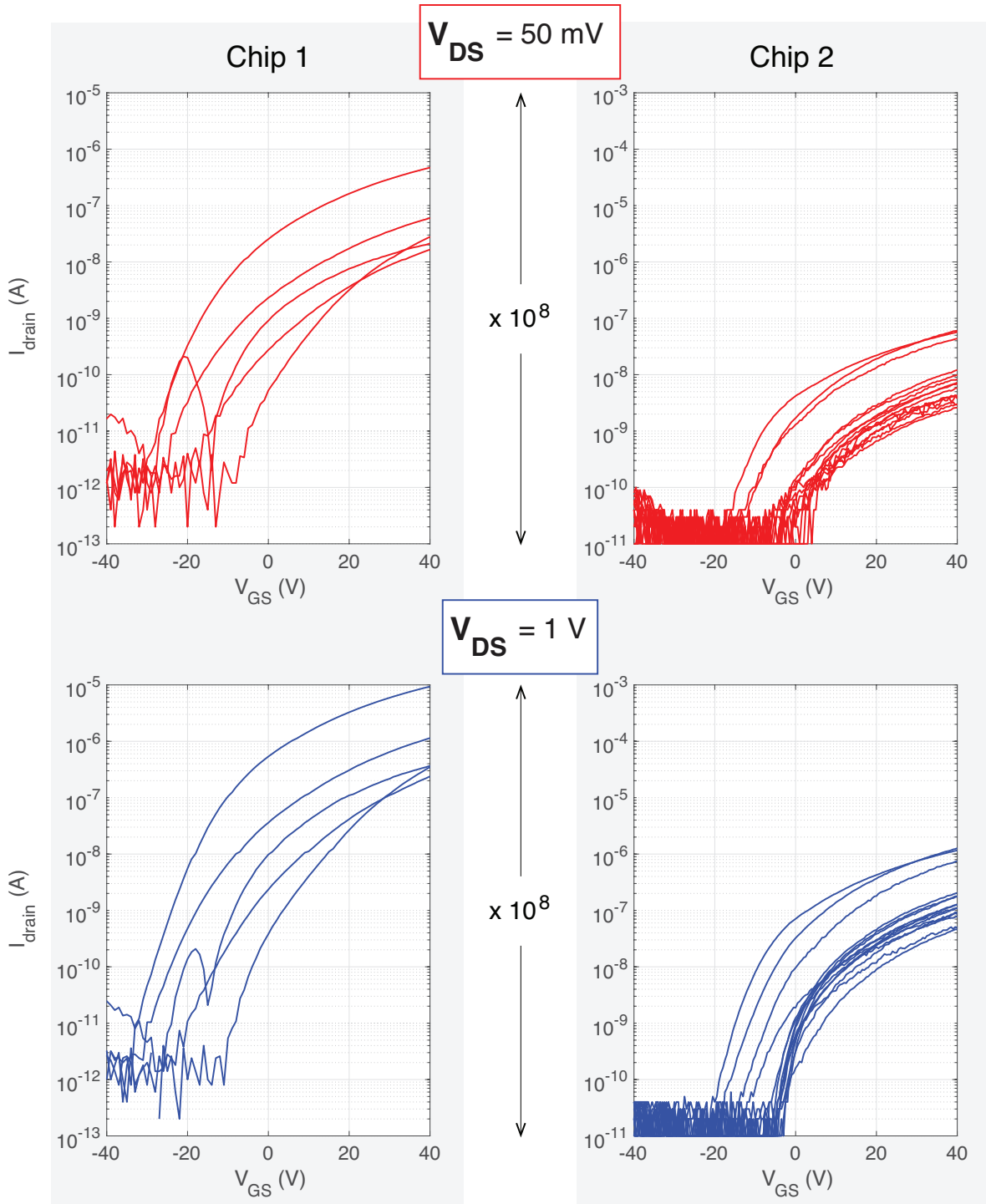


Figure 2.11: Switching characteristics of back-gated MoS₂ devices fabricated on two separate chips, using transferred monolayer MoS₂ channels from two separate initial mined MoS₂ sources. Chip 1 and Chip 2 are from different sources of material; five devices were measured on Chip 1 and 15 devices on Chip 2. All devices demonstrate an on/off current ratio $> 10^3$, with some devices achieving a ratio as high as 10^7 .

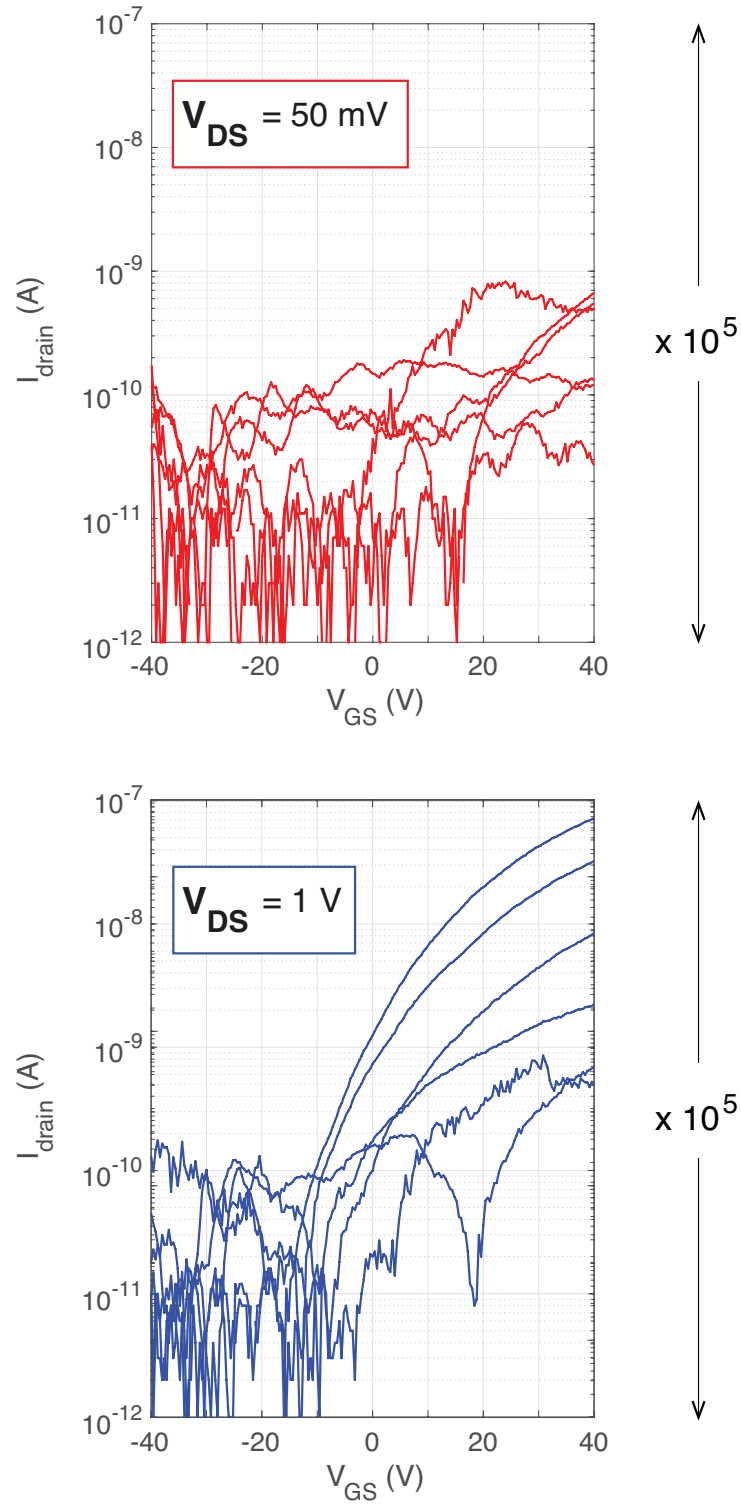


Figure 2.12: Switching characteristics of six back-gated WS_2 devices fabricated from monolayer WS_2 , transferred from a synthetic bulk source. With a source/drain bias of 1V, some devices demonstrated on/off current ratios $> 10^4$.

a given sample, a mean areal yield as well as a standard deviation are reported.

While both measure variations at the level of the entire chip, they reflect different operational scales. The first, feature yield, measures the absolute existence of features appearing on the substrate (and containing *any* monolayer material) relative to how many features were expected, given the chosen pattern. It offers chip-scale commentary about entire blocks—*i.e.*, it reflects whether an entire circuit is likely to be produced. The second, area yield, is a feature-scale metric. It measures the mean and standard deviation of the *connected monolayer* area in each transferred feature⁵. Area yield contains information about whether a sub-component of the circuit is likely to appear. Area yield captures information about mechanical imperfections that may appear stochastically, such as microcracking, and about broader imperfections in the process, such as peeling of the monolayer from the substrate, that may be reduced with proper understanding of the mechanics of processing. Area yield metrics carry implications for device density and circuit design. However, as it does not take into account shape, it cannot inform design which is robust to common material loss regions. .

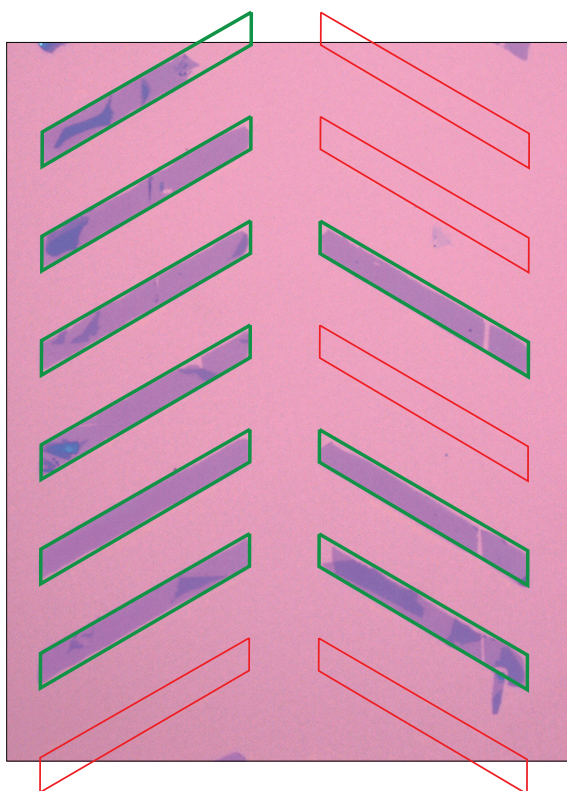
Feature yield was calculated by identifying, by eye, the characteristic color and contrast (relative to the substrate) of monolayer material in a white light optical image. To calculate areal yield, a custom MATLAB script was written to determine the boundaries of monolayer regions from white light optical micrographs. The approach takes advantage of the high contrast between a substrate of 285 nm SiO₂ on Si, and even single monolayers of TMDCs. When a user loads a white light image, the code extracts the intensity in the highest-contrast color channel (red) for each pixel. Currently, the user must seed regions for measurement. Taking advantage of the `grayconnected()` function [133] in MATLAB, which identifies continuous regions of constant intensity (within some user-specified tolerance), the script returns a binary array indicating whether each pixel is in the continuous contrast region. The method is subject to the spatial resolution limits of the image capture optics and the attendant intensity resolution; for instance, small gaps may be undetectable because the increase in intensity associated with exposed substrate is combined with the intensity of existing material within the same pixel. By asking the user the magnification level of the image, the script is able to determine monolayer areas for each feature. Results were manually verified by comparison with PL images, and it was confirmed that identified monolayer regions corresponded to those regions with any appreciable intensity in the PL images. The code is sensitive to step changes in color intensities, and bilayer and thicker regions were consistently identified as non-monolayer. Extracted monolayer areas were also used to generate the histograms in Figure 2.14. The feature and areal yields for three WS₂ and eight MoS₂ samples are shown in Table 2.4. Feature yield ranges up to 67% for WS₂ and up to 54% for MoS₂. Mean areal yields of 63% for WS₂ and 55% for MoS₂ are obtained. Yield from the WS₂ is markedly higher

⁵For the purposes of calculating area yield, non-transferred features are ignored rather than counted as zero-area transfers. The processes which give way to reduced area in transferred features are materially different from those that result in a total loss of material in a position where material was intended to appear.

Feature yield:

Transferred features containing monolayer material

Expected features

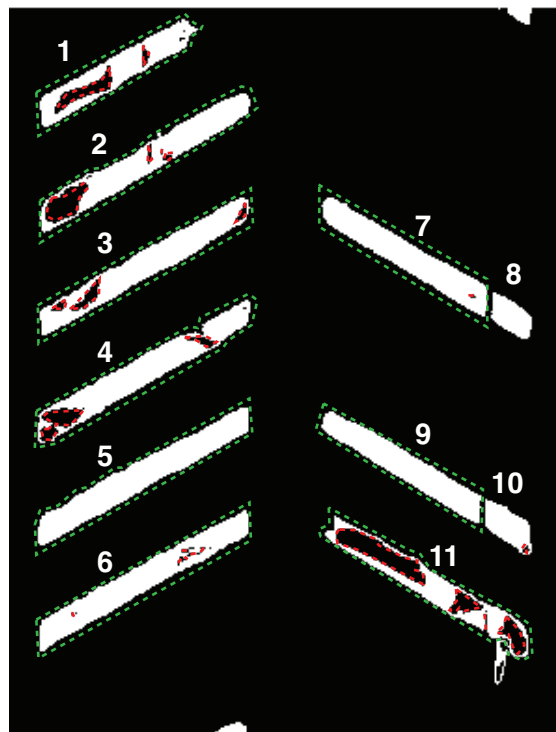


$$\frac{9}{14} = 64.3\%$$

Areal yield:

Mean area of largest contiguous monolayer (■ - ■)

Area of ideal feature



$$\frac{9691 \mu\text{m}^2}{14900 \mu\text{m}^2} = 65.0\%$$

Figure 2.13: Two approaches to yield characterization of transferred monolayer material. Feature yield (left) tabulates the binary appearance of monolayer material within the bounds of expected transferred features in the pattern. This metric is dependent on aspects of the transfer process, like applied exfoliation pressure, exfoliation peel rate, adhesion of the feature to the substrate (substrate pre-processing and transfer pressure and temperature), and forces applied during post-processing, including liquid processing for photoresist and gold removal. Area yield (right) tabulates the mean area of contiguous monolayer material within a transferred feature, as a percentage of the total area of the intended feature, among features including monolayer material. This metric captures aspects of the initial flake quality and the number of exposed layers.

Table 2.4: Feature and areal yield calculations for eight representative MoS₂ and three WS₂ substrates, processed using the technique detailed in Figure 2.5. These substrates include those described by the histograms in Figure 2.14; where applicable, the corresponding histogram label in Figure 2.14 is given in the rightmost column of this table.

	Sample	Feature yield (% features transferred)	Areal yield (% monolayer)		Corresponding histogram in Figure 2.14
			Mean	Sample standard deviation, <i>s</i>	
WS ₂	1	29/119 = 24%	63%	27%	A
	2	52/95 = 55%	28%	18%	B
	3	121/180 = 67%	53%	29%	C
MoS ₂	1	12/24 = 50%	35%	19%	
	2	22/66 = 33%	40%	26%	
	3	13/42 = 31%	25%	19%	
	4	7/65 = 11%	55%	30%	
	5	13/32 = 41%	47%	23%	
	6	14/26 = 54%	31%	19%	D
	7	29/75 = 39%	22%	17%	E
	8	30/136 = 22%	40%	27%	F

than that from the MoS₂, which is attributed to the greater uniformity and flatness of the initial, synthetic, WS₂ source than the natural MoS₂ crystal.

Sources of yield loss

Three processing steps are identified that contribute most significantly to yield loss, and that would therefore be a reasonable focus of future process development. Firstly, in step 5 (as defined in Section 2.3.2), some of the patterned photoresist handles do not adhere to the thermal release tape and therefore remain on the source crystal. This source of defectivity is evident from optical examination of the thermal release tape between steps 5 and 6, in which gaps are visible in the array of features on the tape. Strengthening the binding between the photoresist handles and the adhesive film would help to address this issue, *e.g.* by applying a partially baked photoresist layer to the tape.

Secondly, in some features, the photoresist–gold bond fails during step 5, and the gold and van der Waals layer therefore remain on the source crystal even when the photoresist feature is transferred to the tape. This source of defectivity is again evident from optical examination of the thermal release tape immediately after step 5, in which some of the photoresist features are visible but without the highly reflective gold layer on them. To address this source of yield loss, adhesion of the photoresist to the gold should be enhanced, potentially by adding an O₂ plasma or hexamethyldisilazane (HMDS) treatment between steps 1 and 2.

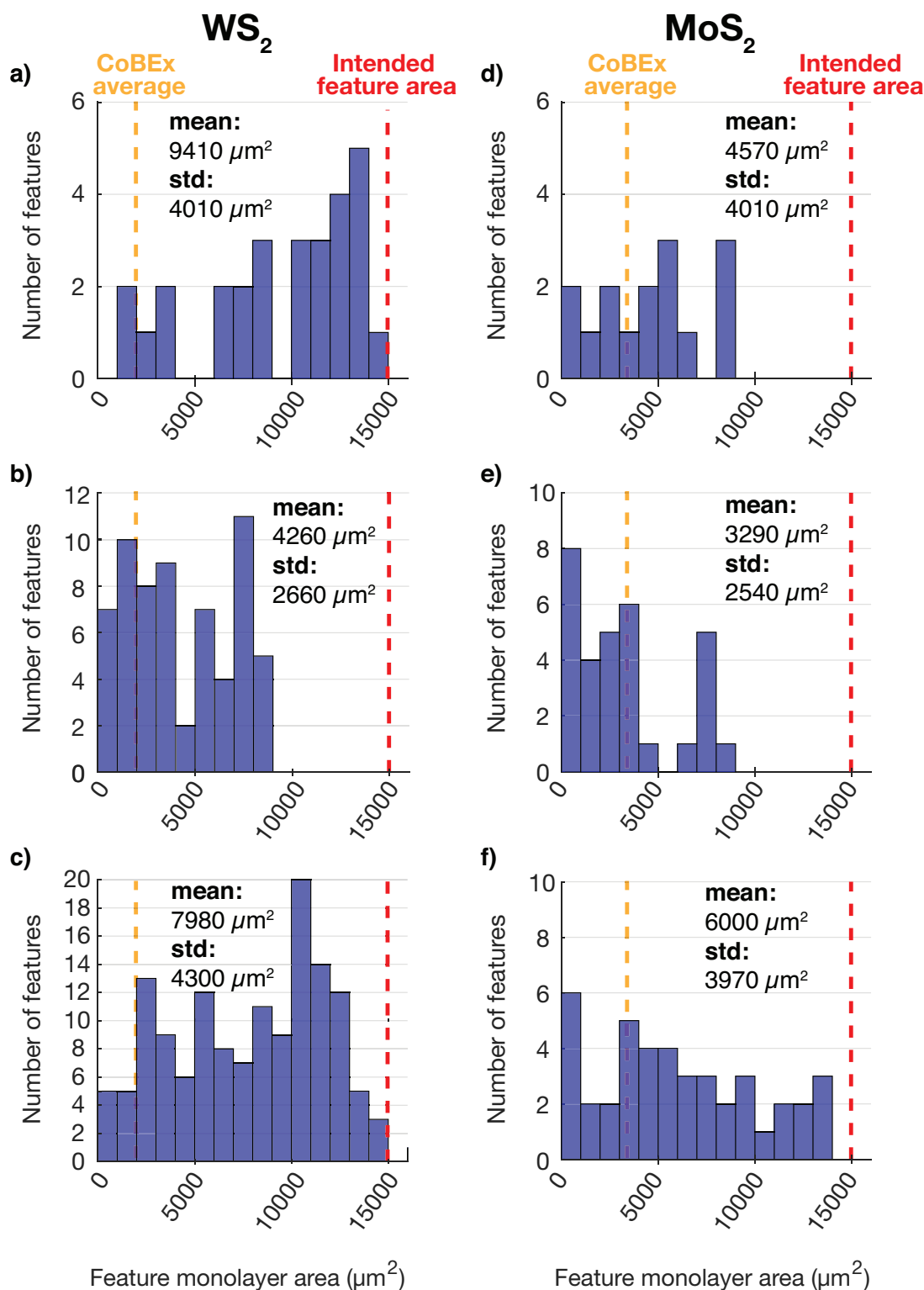


Figure 2.14: Yield results of the exfoliation method. Histograms (blue bars) showing the distributions of the areas of regions of continuous monolayer material transferred to three separate substrates patterned with WS₂ (a–c) and three substrates patterned with MoS₂ (d–f). Samples were all created using the process flow of Figure 2.5, with the exfoliated material being the only variable. The red dashed line indicates the area that would be occupied in a pattern by a full, perfect feature; the yellow dashed line shows the average area of continuous material obtained from many samples using the prior, unpatterned, gold-mediated ‘CoBEx’ method [11].

Thirdly, in some locations where gold polygons are visible on the substrate after step 9, optical reflectance imaging after step 10 shows that the MoS₂ or WS₂ is ultimately absent from those same locations. We attribute this component of yield loss to ingress of KI/I₂ liquid between the van der Waals layer and the substrate during the gold etch of step 10, washing the van der Waals material off the substrate. This explanation is more plausible than earlier failure of the gold–van der Waals material interface, since that interface is formed during the gold evaporation and is known to be strong due to the Au–S bond. We found that limiting the time that elapses between step 9 (exposing the substrate and its contents to O₂ plasma) and step 10 (gold removal in KI/I₂) to below an hour greatly mitigates this third yield limitation, resulting in the yield values reported in Figure 2.14 and Table 2.4. This suggests the surface energy of the substrate is critical; SiO₂ is hydrophilic following O₂ plasma exposure, and gradually becomes hydrophobic thereafter. (The van der Waals materials themselves have a lower surface energy than the SiO₂ substrate, but are partially wetting-transparent; their substrate influences their wettability [134].) Further refining this apparently critical plasma treatment step and/or thermally annealing the substrate before the final gold etch may be beneficial in improving the yield of step 10 beyond the values presently reported.

2.4.4 Atomic force microscopy

While photoluminescence spectroscopy is able to differentiate monolayer TMDCs from thicker material, it is a relative rather than an absolute measure of material thickness. In order to physically verify the thickness of transferred material, atomic force microscopy (AFM) measurements were made.

Atomic force microscopy measurements (Bruker ScanAsyst, tapping mode) confirm that the transferred material regions identified as monolayer material by optical microscopy and photoluminescence spectroscopy are in fact sub-1-nm thick (MoS₂: Figure 2.15; WS₂: Figure 2.16). Additionally, narrow, steep regions are present at the edge of each feature. These may be curled monolayer material, which are observed throughout the feature if the substrate surface is insufficiently hydrophilic during exposure to liquid (KI/I₂ and DI water), driving liquid under the transferred monolayer. In addition to height profiles, phase and tapping-mode (TM) friction measurements were collected from the same topography-mapped regions, on both MoS₂ and WS₂ monolayers. The particles arrayed on both the transferred material and the substrate are approximately 5 nm tall; X-ray photoelectron spectroscopy (XPS) analysis was conducted to determine their composition. In order to determine whether these particles impact the ability to fabricate atomically coupled heterostructures, Raman spectroscopy was performed on “bilayers” created by stacking two successive monolayer transfers with the process described in this work. From an electronic perspective, the demonstrated switching ability of transistors formed using transferred monolayers (see Section 2.4.2) confirms that the remnants do not short devices. At shorter channel lengths, however, the remnants may pose a challenge. Extended KI/I₂ acid treatment of the surface, possibly coupled with one or more of me-

chanical agitation, sonication, and an extended or more vigorous water rinsing protocol afterwards could assist in residue removal.

2.4.5 X-ray photoelectron spectroscopy (XPS) characterization

XPS (Perkin Elmer PHI 5600 ESCA System with neutralizer, spot size: 800 μm diameter, source power: 400 W) was used to identify the materials present on the surface of fabricated arrays of transferred monolayers, and in particular to identify candidate elements for the nanoscale particle residue detected using AFM. XPS was chosen for its sensitivity to surface material, in contrast to typical material identification methods like energy-dispersive X-ray spectroscopy (EDS). An XPS trace from transferred material is shown in Figure 2.17. Several elements were expected to appear in the measurement: tungsten and sulfur (TMDC monolayer), silicon and oxygen (substrate material), and carbon (adventitious carbon [135]). Of the unexpected peaks, the most pronounced corresponds to the 4p3 orbital of gold. Though the gold used in the process is, in theory, removed during a final KI/I₂ etchant exposure (see Section 2.3.2, step 10), it is possible that nanoscale particles remain on both the transferred monolayer and the silicon oxide substrate surfaces.

FET device characterization measurements have confirmed that test devices, which have 10 μm channel lengths, exhibit strong switching behavior. The residues are therefore evidently sparse enough not to inhibit operation of devices at the 10 μm length-scale. Since XPS analysis of the residue indicates that it is gold, it is conceivable that as devices are scaled down, the residue might provide a current-shortening path, but such behavior has not been observed. Another potential concern might be that surface residues could inhibit the formation of planar heterostructures requiring atomically-spaced layers. To examine this possibility, we investigated a planar interface formed between two MoS₂ monolayers that were transferred sequentially, followed by thermal annealing (Section 2.4.6). The XPS evidence that these residues are gold suggests that they could be removed, if necessary, by modification of the final gold etching step, *i.e.* step 10 of the process. Extended KI/I₂ acid treatment of the surface, possibly coupled with one or more of mechanical agitation, sonication, and an extended or more vigorous water or solvent rinsing protocol could assist in residue removal. For the use of this process in combination with traditional silicon electronics, any gold residue would need to be very thoroughly removed.

2.4.6 Confirmation of heterostructure fabrication compatibility

In order to produce functional van der Waals heterostructures, it is critical that joined layers are able to come into intimate contact such that they are able to electronically couple. Raman spectroscopy measures the stiffness of vibration modes and provides a measure of mechanical strength of interlayer coupling. PL spectroscopy, meanwhile, provides a measurement of the electronic strength of interlayer coupling. Mechanical coupling strength in TMDs correlates with electronic coupling strength [136]. In order to deter-

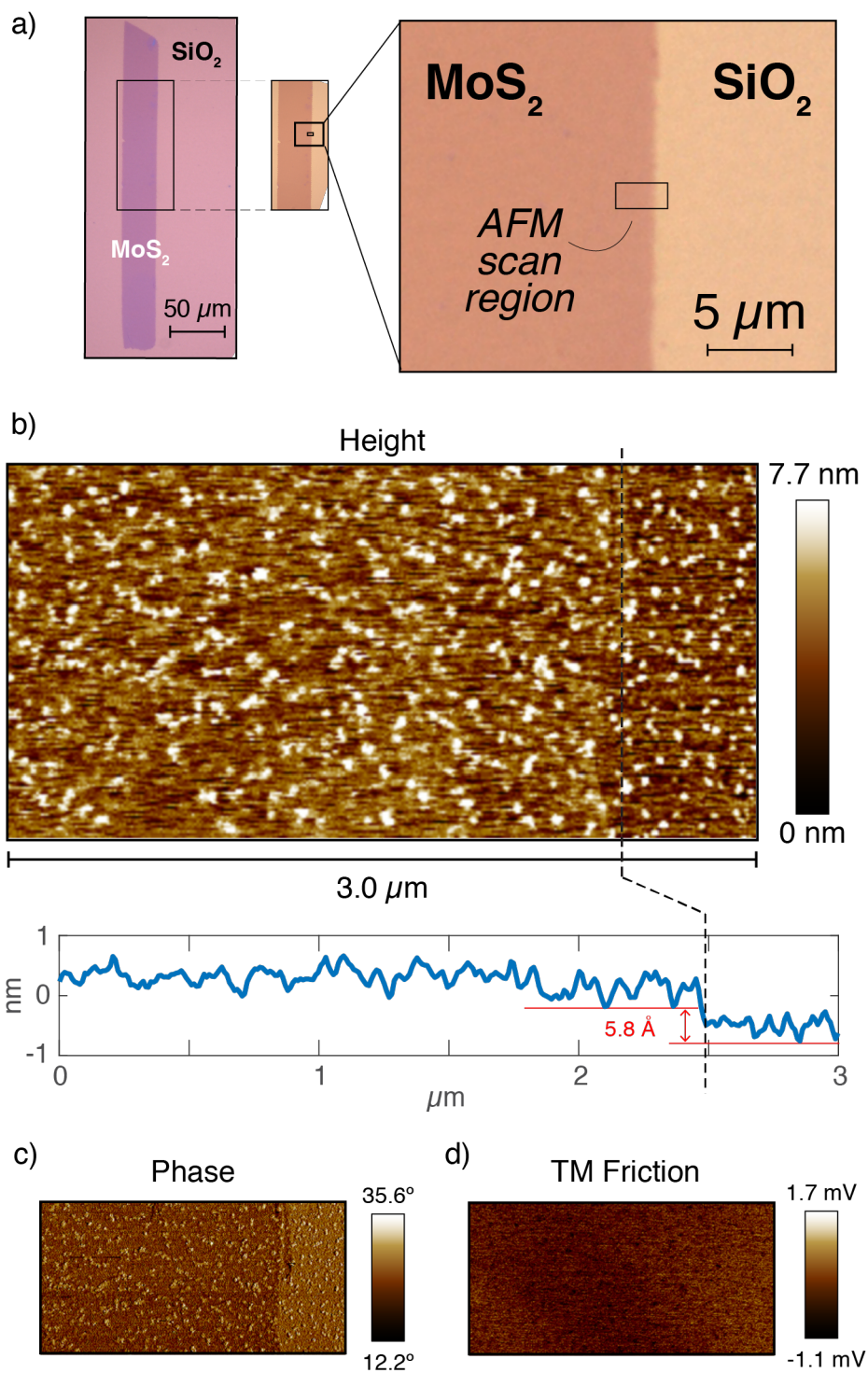


Figure 2.15: (a) White light optical image of the MoS₂ monolayer region measured with atomic force microscopy; (b) topographical map measured by atomic force microscopy in tapping mode, with an averaged trace shown below indicating a ~ 6 Å step height between the substrate and the transferred monolayer; (c) AFM phase lag map and (d) friction map of the same region.

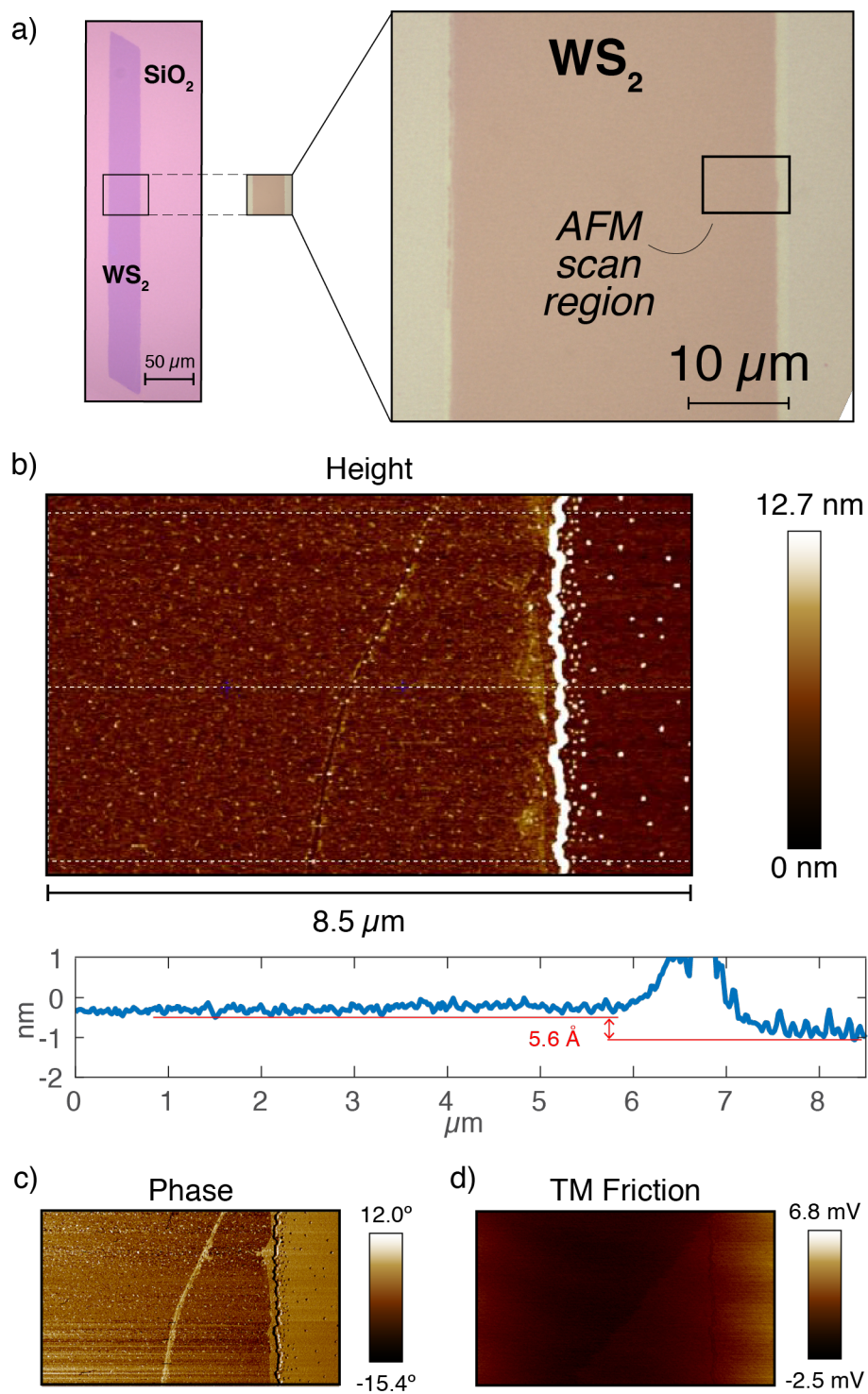


Figure 2.16: (a) White light optical image of the WS_2 monolayer region measured with atomic force microscopy; (b) topographical map measured by atomic force microscopy in tapping mode, with an averaged trace shown below indicating a $\sim 6 \text{ \AA}$ step height between the substrate and the transferred monolayer; (c) AFM phase lag map and (d) friction map of the same region.

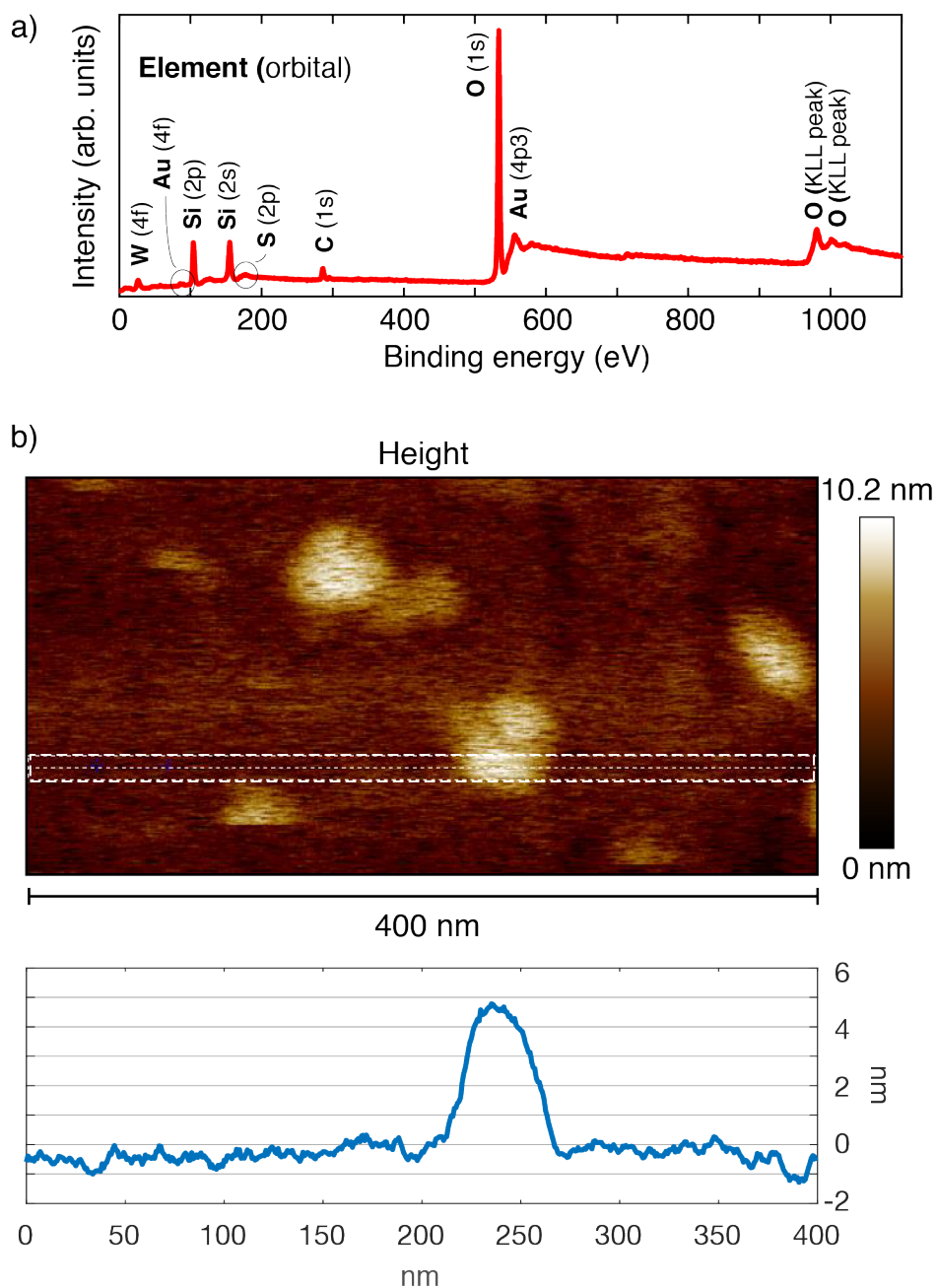


Figure 2.17: (a) XPS characterization of residual particles on WS_2 , indicating the presence of expected substrate elements (Si, O), TMDC elements (W, S), and calibration elements (C). The remaining identified element is Au, which may comprise the residual particles. (b) AFM topography map of the particles. The height of the region in the white dashed box is plotted in the accompanying line-scan, showing that the particles are ~ 50 nm wide and ~ 5 nm tall.

mine the strength of interlayer coupling between stacks of monolayers produced using this method, and thus their fitness for use in van der Waals heterostructures, Raman spectroscopy was used to examine both natural and synthetic bilayers. Two cases were characterized: 1) stacks of two layers, which were in contact in the bulk crystal, once they have been removed to an SiO₂ substrate (“natural” bilayers), and 2) stacks of two layers, manually produced by transferring one monolayer to an SiO₂ substrate, then transferring a separate monolayer (from an arbitrary crystal) overlapping the first (“synthetic” bilayers). A single-material synthetic bilayer of MoS₂ was fabricated by repeating the process described in Section 2.3.2 twice, with the patterned monolayer results of the second transfer overlapping the results of the first.

A region including both overlapped and non-overlapped material was mapped using Raman spectroscopy, in the same configuration described in Section 2.4.1 (Figure 2.18). Initially, a Raman spectrum of the stacked material indicates that the stack behaves as two monolayers (Figure 2.18(a)-(c), data point *b*); however, after brief exposure to heat (3 minutes at 150 °C, followed by 3 minutes at 200 °C), a Raman spectrum collected from stacked material shows an inter-peak distance characteristic of an MoS₂ bilayer (Figure 2.18(d)-(f), data points *d* and *e*). The Raman spectra measured at multiple locations on this constructed bilayer are consistent with bilayer material—and not with two separate monolayers—which indicates that the layers became atomically close after transfer and annealing. Such behavior indicates that residues on top of the first-deposited MoS₂ layer did not inhibit the formation of intimate contact between it and the second-deposited MoS₂ layer. It is probable that the residues are so sparse that a monolayer of a 2D material can easily conform to them. Though preliminary, these measurements indicate that the monolayers can functionally couple despite the gold remnants.

2.4.7 Theory of metal film assisted exfoliation

A key feature of the process is the ability to reliably transfer monolayers using a single, controlled exfoliation step. This exfoliation process begins with the deposition of a thin metallic film (Au in this case) that mediates the process. Experimentally, it has been shown that the Au film can increase the monolayer selectivity of the exfoliation process, and also has the potential to exfoliate large-area samples [11].

A theory has been developed for the exfoliation process⁶ that explains the experimental observations and can be used to design films tailored to the exfoliation of specific materials. In brief, the metallic film does two important things to the exfoliated material. First, it strains only the top layer of the film that is to be exfoliated [65]. This strain leads to two important and sometimes competing effects. The strain changes the effective atomic density of the film. This alters the strength of the van der Waals force (on a per-area basis) between the top and subsurface layers of the crystal. A decreased binding force weakens the interface between these two layers. Second, the strain in the film also changes

⁶Sun, ..., Gramling, *et al.* [66]

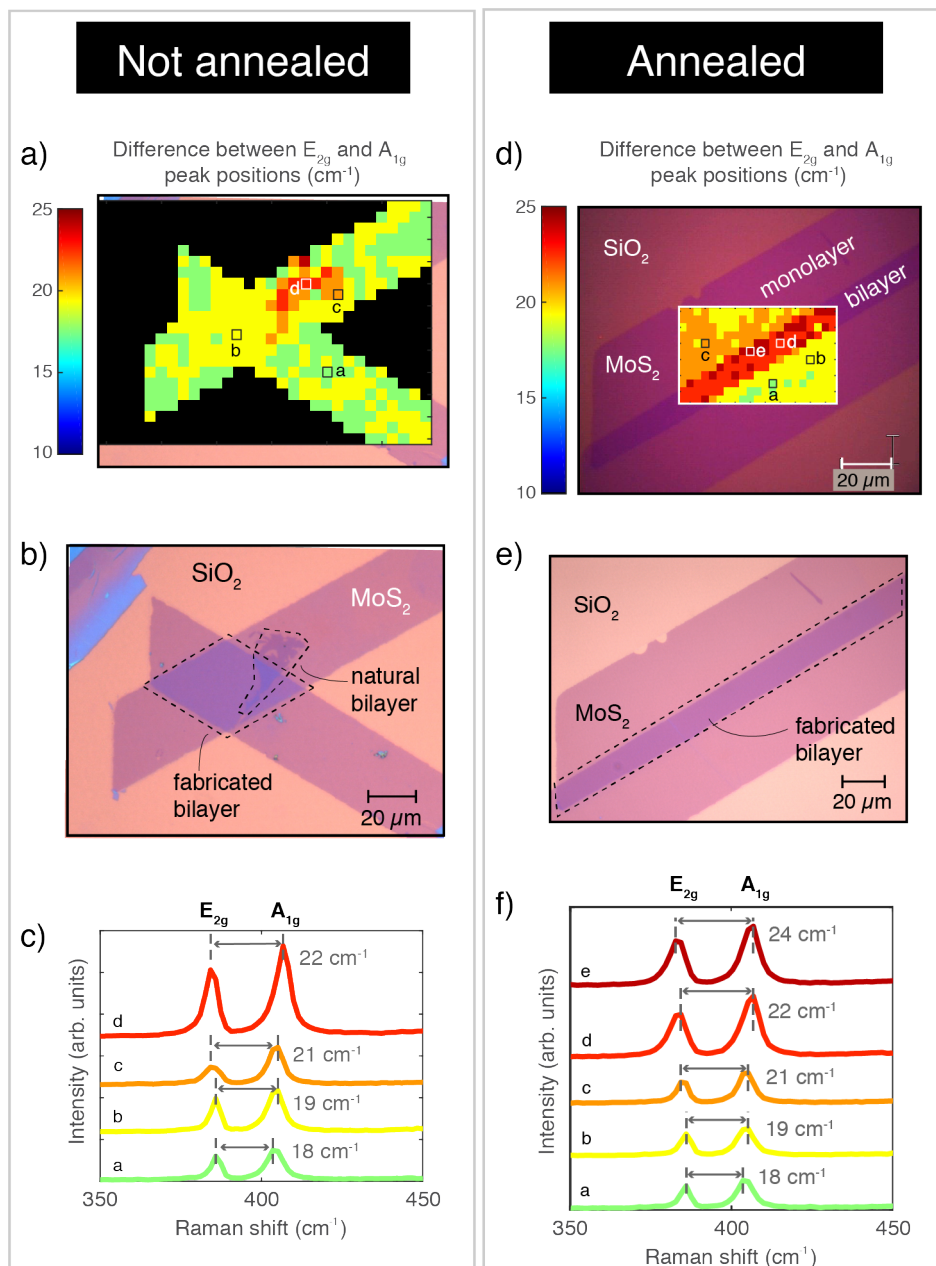


Figure 2.18: (a) Raman map of two crossed MoS₂ monolayer features, whose overlap forms a fabricated MoS₂ bilayer. The inter-peak difference is consistent with monolayer MoS₂, except in the region where a natural bilayer is present, highlighted in (b). (c) Spectra from several points on the Raman map, indicating both monolayer and bilayer material are present. (d) Raman map of two overlapped MoS₂ monolayers, creating a fabricated bilayer, after a brief annealing step. The overlapping region now behaves as an MoS₂ bilayer, as indicated by the increased E_{2g}-A_{1g} peak difference (in cm⁻¹). (e) The region mapped in (d). (f) Spectra from identified points of the region mapped in (d).

the stacking registry of the layer to be exfoliated. Because the lattice parameter of the strained to-be-exfoliated layer differs from that of the layer below, some regions of the exfoliated layer will be in unfavorable stacking positions relative to their initial positions. This weakens the bond between the exfoliated layer and layers beneath. The strain effects of the metallic film are present and play a role even in the exfoliation of nominally infinite monolayers. However, the monolayer-selective exfoliation and transfer of patterned films is further assisted by the additional stiffness of the metallic film.

Based on this understanding, one should be able to design patterned exfoliation processes with enhanced monolayer selectivity for a broad range of 2D van der Waals-bonded materials.

2.5 Conclusions

With this method, we can now simultaneously control interlayer and intralayer fracture in van der Waals solids. While simply blanketing the source material with gold may achieve monolayer selectivity in some regions, such an approach offers no control over where intra-layer fracture events will initiate. We expect that exfoliated material edges would then correspond to naturally occurring layer steps in the crystal structure. By introducing etched steps in the material at the edges of the photoresist handles, it is possible to pre-seed the locations of fracture.

We expect that a key to increasing yield will be to address three particular defect-inducing process steps identified in Section 2.4.3. An additional likely source of defectivity that cannot be attributed to a specific process step is the intersection of patterned gold regions with natural step changes in the height of the source material. These intersections provide opportunities for patterned handles to contact multiple layers and thereby exfoliate multilayer material. Such intersections could be reduced by maximizing grain size relative to the exfoliated feature size.

This significant step forward in 3D spatial control over exfoliation has been demonstrated here for both MoS₂ and WS₂, and in the future could enable complex integrated circuits to be fabricated more easily from van der Waals materials. The technique's ability to transfer monolayer sheets with areas $> 10^4 \mu\text{m}^2$ makes it particularly appealing for the production of complex heterostructure-based circuits. The capability for large-area transfer is emphasized although, in principle, there is no impediment to using the technique to transfer arrays of much smaller regions of material, *e.g.*, to define many individual submicrometer transistor geometries prior to exfoliation and transfer. The challenge in that case would be to ensure a high enough feature yield to be able to construct the desired integrated circuit without missing devices. In contrast, higher functional yields may be achieved by transferring arrays of large monolayer sheets, as demonstrated, and then defining, for instance, conductive interconnect patterns to create one or more whole integrated circuits within each successfully transferred large monolayer region. Although the present process exploits Au–S binding to achieve monolayer selectivity, the basic

mechanism, which hinges on a lattice constant mismatch, is expected to be applicable to other material pairs, and would be a valuable focus of future studies. For instance, nickel has been demonstrated to have an appropriate lattice constant difference to apply in-plane strain to a layer of graphene in bulk graphite [137]. Additionally, metal-mediated exfoliation may find itself used in conjunction with other emerging techniques for epitaxy and transfer of thin films [96, 95, 138] to create semiconductor heterostructures.

Currently, the field of van der Waals monolayer fabrication, and particularly pattern fabrication, lacks yield metrics by which to measure candidate processes, and to gauge progress. Ideally, the use of yield metrics in this work—despite scores far below those required for mass manufacturing—will encourage the authors of future studies to consider and report their own yields, whether using the metrics introduced here, or their own manufacturing-relevant benchmarks.

Chapter 3

Finite element modeling of van der Waals layers in contact with an elastic stamp

3.1 Introduction

We aim to elucidate factors contributing to separation layer selection in layered materials—specifically, in the semiconducting class of van der Waals layered materials called transition metal dichalcogenides, or TMDCs. Existing literature [9, 11], as well as the work in Chapter 2, have shown that inducing compressive, in-plane strain in the top layer of a van der Waals layered material transforms the exfoliation interface location from stochastic to deterministic. Here, we investigate whether other mechanical aspects of the system can similarly exert sufficient control over interlayer separation to make prediction of the exfoliation interface deterministic. Ultimately, manipulating the location of the exfoliation interface is a matter of disproportionately weakening one interface. Metal-assisted exfoliation manipulates the exposed top layer to weaken the top layer/second layer bond. Any boundary could feasibly be manipulated: in addition to the top layer, edges present an opportunity to introduce inhomogeneities in the system.

All dry exfoliation methods rely on some kind of stamp or tape, used to contact and remove the Ångstroms-thick van der Waals layer(s). In the case of patterned exfoliation, like the process described in Chapter 2, the van der Waals features have pre-defined edges. These two aspects of an exfoliation system dovetail to create a scenario in which the details of the stamp’s mechanics can impact the distribution of normal displacement among the layers. When an infinite, unpatterned stamp contacts a continuous van der Waals crystal, without edges, the entirety of the stamp face is loaded during exfoliation: a stamp would not experience variation in its out-of-plane strain, resulting in no curvature on its bottom face. However, the variation in loading on the bottom face of the patterned stamp due to the non-continuous van der Waals features results in out-of-plane deformation of the stamp, as it alternates in space between loaded and unloaded regions. The shape of these deformations is a function of the mechanical properties of the stamp and of the van der Waals crystal, and the geometry of the system. The spatial alternations of the stamp can introduce bending in the van der Waals layers. Bending imposes an energetic cost that competes with the van der Waals binding energies between the layers. This competition between bending and binding not only dictates the interlayer separation, particularly at the edge, but also varies as a function of the bend radius, which is dictated by stamp deformation. In-plane strain imposes an energetic cost and impacts atomic density and thus binding energy; both effects can be neglected when in-plane strain is small.

Thus, we have an opportunity for mechanical manipulation: attempting to use the mechanics of the stamp to manipulate interlayer displacement at edges, which will serve as crack initiation sites. Two factors are investigated to determine their impact on the distribution of displacement between layers and thus on exfoliation interface selection: the Young’s modulus of the stamp, and the geometry of the system—specifically, the lateral distance between van der Waals features, which determines the ratio of loaded to unloaded distances along the stamp’s bottom face.

3.2 Methods

3.2.1 Previous approaches to van der Waals finite element modeling

Molecular dynamics (MD) approaches apply the most basic laws of classical mechanics, Newton’s laws of motion, to the interactions of ensembles of atoms. In this sense, molecular dynamics models are equivalent to running a “computer experiment” on atoms¹, a first step on a bridge between nanoscopic and macroscopic measurement and modeling capabilities. MD software, like the widely-used Large-scale Atomic/Molecular Massively Parallel Simulator ([LAMMPS](#)) package [139], is explicitly designed to handle few, short-range interactions. Tracking and simultaneously solving for a large number of atoms rapidly becomes computationally expensive. While MD methods capture nanoscale effects, they are limited to nano-dimensioned models.

The concept of using Newton’s laws to solve for the displacements in a system is applicable at any scale. Atomic systems have the benefit of offering an obvious discretization scheme. Solving for the local displacements of larger objects requires a method for subdividing the object, and coupling the responses of the individual regions. This is precisely the contribution of the finite element method. Finite element analysis (FEA) is nearly universally used to model macroscale problems, and offers the benefit of accommodating model-specific macroscale physics (for example, beam theory and elasticity theory) when appropriate.

Multi-scale problems present a gap. Scale-up of an MD approach will eventually run into excessive demands on the amount of computational power required. Using FEA, the size of the simulation and the governing mathematics are the choice of the user; nonetheless, the availability of computation power still presents a tradeoff between the overall scale of the model and the ability to resolve the details of interatomic interactions. It is appealing to attempt to bridge the two. Given the flexibility of FEA, the mathematics governing macroscale deformation could be coupled to mathematics approximating nanoscale effects. Particularly if the atoms can be “smeared” without loss of quality—in other words, the locations of individual atoms can be subsumed into an aggregate in a physically meaningful way—and if macroscale deformations are expected to play a critical role in the behavior of the system, an FEA approach presents a feasible path forward.

Ultimately, the matter of a micron-scale stamp with macroscopic mechanical properties, interacting with a series of van der Waals-bonded layers, presents a multi-scale modeling problem of precisely this type. We are then interested in whether the nanoscale effects we intend to simulate can be effectively captured in a finite element model.

Several authors have been interested in elucidating the deformation of large systems with nanoscale features, and particularly systems in which some key interaction is governed by a van der Waals bond. In order to capture both macroscale and microscale

¹In regimes where it is reasonable to neglect quantum effects

physics, the Abaqus finite element package is a popular choice of solver for its compatibility with user-specified interaction routines. The details of the interlayer interactions may be captured in a user subroutine, with the pertinent mechanical information, namely local stress and stiffness, passed back to the main solver. The approaches to using Abaqus vary: both the choice of load used to describe the van der Waals force, and the means of treating the attractive and repulsive parts of the van der Waals interaction have been handled differently by different researchers.

Cho and Park modeled van der Waals contact to attempt to design surfaces to prevent adhesion (stiction) in microelectromechanical (MEMS) devices [140]. They integrated a van der Waals interaction into a specific body force, in order to account for both surface atom interactions and the forces exerted by subsurface atoms. The body force expression as a function of distance was used as an output of the `DLOAD` subroutine in Abaqus, and used to model the pull-off force of an indenter leaving a surface. They compared the results of their finite element model to both MD (nanoscale) and Hertz contact theory (macroscale) predictions, finding good agreement with both. The authors included the repulsive term of the Lennard-Jones potential in their body force calculations, rather than treating the attractive and repulsive components with different model elements. Their use of `DLOAD` with an integrated body force is limited to a single pair of surfaces interacting; Abaqus only passes the coordinates of the current node to `DLOAD`, removing the possibility of calculating interlayer distance for non-fixed layers.

In a similar vein, Bortoleto and co-authors used `DLOAD` in Abaqus to study van der Waals adhesion and material removal during separation between a single pair of surfaces [141]. For their very small (2-10 nm maximum dimension) simulations, they found good agreement to MD results. Their approach models only the attractive part of the Lennard-Jones potential representing the interaction between surfaces, and relies on Abaqus built-in methods for handling contact stress when the bodies are in compressive contact. This requires dynamic addition and removal of a contact constraint in the simulation.

In an attempt to enable larger simulations, Liu and co-authors developed an approach they term the atomic finite element method, or AFEM, which can be used to capture the multiple covalent bonds a single atom may participate in, within a given element [142]. The approach is intended to examine small regions where nanoscale interactions dominate, within a macroscale system which is represented with standard finite elements; modeling an entire macroscale region with AFEM elements was shown to be prohibitively computationally expensive². In order to couple the two approaches and achieve high-fidelity atomic representations with a reasonable computation time, so-called transitional elements must be created. When using the coupled AFEM/FEM approach to model carbon nanotubes, the authors added the van der Waals interactions with the dynamic addition and removal of “strings” acting on the elements, within a given cutoff radius. This approach is ill-suited for situations where large regions of atoms participate in van

²Modeling a single-point displacement of a fixed-end 605 nm long carbon nanotube beam required 24 minutes, albeit with the computing power available on a 2004 CPU.

der Waals interactions.

The Abaqus user subroutine `UINTER` allows a user to specify a set of contact parameters, such as stress, stiffness, and heat flux, as a function of the position and displacement of a *set* of nodes. In contrast to `DLOAD`, which specifies a load on a single surface or body, `UINTER` governs an interaction between multiple bodies, and in doing so provides normal and tangential distances between a pair of surfaces. Due to this adaptability, it has been used to capture and analyze the behavior of different atomic-scale inter-sheet phenomena, such as graphene sheets, including multi-walled carbon nanotubes [143], and lipid bilayers [144]. This approach is suitable either when the precise location of atoms is insignificant, or when the nodes correspond to exact atomic positions. Pantano, Parks, and Boyce modeled concentric layers of carbon nanotubes to understand the bending and buckling behavior of multi-walled nanotubes [143]. In the course of their analysis, they found that the `UINTER` approach to modeling surface-surface van der Waals interactions is appropriate when the radii of curvature of the interacting layers are similar, or very large—an assumption we make in Section 3.2.2.

For exact modeling of systems where the precise locations of atoms is important, it is desirable to couple molecular dynamics (MD) calculations for small regions or features of interest into a finite element engine, which can handle physical calculations for components at larger size scales. This approach, termed the molecular dynamics finite element method (MDFEM), superimposes elements corresponding to each bond, and explicitly solves the nanoscale constitutive equations for each element at each time step. Thus far, the approach has only been demonstrated with graphene, a system composed of a single element. However, Wilmes and Pinho demonstrated graphene MDFEM results with linear scaling, computing twenty incremental strain steps of a single one million atom nanotube in under four hours [145].

The use of Abaqus, with a `UINTER` subroutine deployed to capture the van der Waals interactions between atoms, is a validated means of integrating nanoscale effects into a microscale model. However, prior work has not explicitly considered the behavior of edges³, nor, to the best of our knowledge, attempted to capture the interactions of a macroscale elastic member with a van der Waals-dominated system. Modeling stamp-layer interactions is further complicated by the need to solve the coupled interactions of multiple layers, each of which explicitly interacts with more than one other layer.

Treatment of inter- and intralayer stiffnesses

The interlayer deformation of a van der Waals material is governed by the aggregate of van der Waals bonds between the component atoms. Van der Waals potentials are modeled as a function of atomic separation using a Lennard-Jones potential [146], which pairs a rapidly diminishing ($1/r^{12}$) repulsive term with a more gradually receding ($1/r^6$) attractive term:

³MDFEM approaches, by virtue of considering each bond, do account for the discrepancy in force at edges.

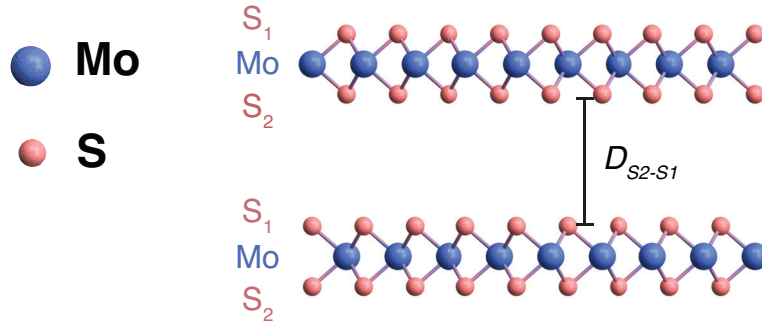


Figure 3.1: Two interacting layers of MoS₂. Each layer consists of two chalcogen sublayers (sulfur atoms) and one transition metal sublayer (molybdenum atoms). The interlayer distance D used throughout this chapter is D_{S2-S1} , the distance between the nearest sublayers of sulfur atoms in adjacent layers.

$$E(r) = 4\varepsilon \left[\left(\frac{\sigma}{r} \right)^{12} - \left(\frac{\sigma}{r} \right)^6 \right], \quad (3.1)$$

where r is the interatomic distance, ε the interaction energy parameter of the potential for a given choice of atoms, and σ the interaction distance parameter for the given atoms.

There are nine interlayer interactions to account for. Each TMDC layer is a suplayer composed of three sublayers: a top chalcogen (sulfur) sublayer, a central metal (molybdenum) sublayer, and a bottom chalcogen sublayer. Between two interacting layers, there are sulfur-sulfur interactions, sulfur-molybdenum interactions, and molybdenum-molybdenum interactions. Table (3.1) contains the Lennard-Jones parameters ε and σ for each atomic pair type.

Liang and co-authors [147] argue that, rather than considering each interatomic interaction type, the contribution of metal-metal interactions (Mo-Mo interactions in MoS₂) is small⁴. Thus, the change in distance between Mo sublayers in this model is not significant, and the strength of the Mo-Mo interaction may be folded into a net potential, given in Table 3.1. They then fit Lennard-Jones parameters as a function of distance between sulfur sublayers closest to the interface ($D = D_{S2-S1}$, Figure 3.1), in order to match empirically measured out-of-plane stiffnesses (C_{33} , normal to the layer surface) of MoS₂, accounting for the stiffness of the layer itself as well as the interlayer stiffness. Using Lennard-Jones parameters for each atomic pair type, the forces and stiffnesses of each interatomic pairing, between two MoS₂ molecules at the equilibrium layer separation, were calculated (Table 3.2). The total force applied by all interatomic pairs besides the two nearest sulfur atoms is 15% of the interatomic force of the nearest sulfur atoms; these atoms are also closest to each other, and thus most sensitive to changes in separation distance. This is evident by the fact that their interatomic stiffness is two orders of magnitude greater than that of

⁴Conversely, within a single covalently bonded layer, Jiang and co-authors find that the Mo-Mo interaction potential is much larger than the S-S potential [148].

Table 3.1: Lennard-Jones parameters for interatomic interactions in MoS₂.

Atom types	ϵ	σ
S-S, fitted to MoS ₂ interlayer stiffness [147]	0.00693 eV	3.13 Å
S-S [149]	0.01187 eV	3.595 Å
Mo-Mo [149]	0.00243 eV	2.719 Å
S-Mo [149]	0.02489 eV	3.157 Å

any other interatomic pairing. Thus, the nearest-neighbor sulfurs dominate the interaction at close-range, and, as the layers are separated, the strength of the nearest-neighbor sulfur interaction falls off later than other interactions. In order to simplify the calculation to one type of atomic pairing, while maintaining mechanical fidelity, the sulfur-sulfur potential provided by Liang and co-authors [147] is used in subsequent calculations.

The within-layer mechanical properties of 2D materials are typically treated equivalently to bulk materials, with stiffness reported as the deformability as a function of force exerted over a given cross-sectional area. Of course, the very premise of “two-dimensional” materials invites the question of how to define cross-sectional area. For graphene, the truly atomically-thin nature of the sheet makes estimation of its thickness a complicated question [150, 151], leading to claims of outstanding stiffness relative to any other (3-dimensional) material measured in the same way [41]. There has been a shift in the field to reports of stiffness in units of force/extension (comparable to spring stiffness). However, for the purposes of finite element modeling, the layers are treated as 3D objects with a finite thickness, which is more straightforward to determine in the case of multi-atomic-layer MoS₂ monolayers. Thus, the elastic properties are reported in standard units of Pa. The values used are given in Table 3.3.

3.2.2 Assumptions

The layers are expected to experience a large bend radius. Thus, relative tangential displacements between layers are neglected, and a constant interlayer displacement is assumed over the extent of the area associated with a given node. Interlayer shear friction is commonly neglected in van der Waals layer deformation studies [152, 143, 153, 154], and the same is done in this work. No translation is prescribed in the x - y plane, and the small expected shear strains and large bending radii indicate that shear displacements will be small.

Though the full elastic tensor of the layers is included in the model, and the Poisson’s effect will be included in Abaqus’s solution, the interlayer distance calculations assume no change in layer thickness due to the Poisson’s effect as the layer experiences in-plane-strain. The elastic properties of the layers are also assumed to be constant throughout the deformation. Similarly, assuming small in-plane strains, the atomic density per unit area is assumed to be constant. These assumptions were validated once the model was

Table 3.2: Initial forces and stiffnesses between two nearest-neighbor MoS₂ molecules in adjacent layers. Positive forces are attractive, while negative forces are repulsive. Atom layer labels are shown in Figure 3.1. Stacking order is considered. Of note, the values listed are interatomic forces for select atoms, not interlayer forces, and thus do not sum to zero. For instance, the S₂-S₁ force appears disproportionately large compared to the positive forces; considering a given S₂ atom, only the interaction with its nearest S₁ atoms will be negative, whereas the contributions from additional S₁ atoms will be attractive, as they are further away.

Top layer atom	Bottom layer atom	Distance at equilibrium (Å)	Force at equilibrium (eV/Å)	Stiffness at equilibrium (eV/Å ²)
S ₁	S ₁	6.41	0.0013	0.0013
	Mo	7.74	0.0004	0.0003
	S ₂	9.50	0.0001	0.0001
Mo	S ₁	4.56	0.0078	0.0025
	Mo	6.41	0.0013	0.0013
	S ₂	7.74	0.0004	0.0003
S ₂	S₁	3.49	-0.1355	-0.6723
	Mo	4.56	0.0078	0.0025
	S ₂	6.41	0.0013	0.0013

Table 3.3: Within-layer elastic constants used for shell elements of MoS₂, originally reported in N/m, from ref. [19]. Values were converted to GPa using a single-layer thickness value of 6.1 Å, and ultimately implemented in units of J/μm³. All unlisted constants are zero.

Elastic constant	N/m	GPa
$C_{1111} = C_{2222}$	134.1	220.0
C_{1122}	34.4	56.4
$C_{1133} = C_{2233}$	0.5	0.8
C_{3333}	0.2	0.3
C_{1212}	14.3	23.4
$C_{1313} = C_{2323}$	0.2	0.3

run: in the worst case, that of the softest stamp, the in-plane shear strain achieved a maximum value of 0.00002.

3.2.3 Defining interlayer interactions

We are interested in the case of a layer of particles interacting with the layer(s) below, which, in the case of a bulk material, are effectively semi-infinite in number. In the case of a layer interacting with the remainder of the bulk, whether to model the layers below as a single layer or a semi-infinite body is a first consideration.

Fundamentally, there is a loss of precision when many layers are lumped together to capture the fact that there is an entire body acting on the layer. An assumption of constant interlayer distance is required.

Van der Waals attractive forces — the dominant component of the interaction — fall off as $\frac{1}{r^6}$, meaning an atom at distance $2d$ has less than 2% the energetic contribution of an atom at distance d . However, the inverse dependence on distance is not nearly as steep for the body force operating over many atoms, which scales as $\frac{1}{r^4}$ (derivation in Appendix). Consider three layers at the top of a bulk stack. Small discrepancies in interlayer distance between the first and third layers, due to displacement of the first layer, have approximately $\frac{1}{16}$ the impact on force as discrepancies in interlayer distance at the interface, between the top/first layer and the second/adjacent layer. We call the second layer a nearest-neighbor layer to the first layer. The third layer, and all layers below it, are non-adjacent to the first layer. Choosing to integrate over the entire body would capture the 7.6% force contribution of all non-adjacent layers on the first layer⁵. However, it would involve neglecting the $\frac{1}{16}$ impact of any variations in interlayer distance by assuming constant interlayer distance in the remainder of the body. The approach also runs into practical issues: the inter-body contact stresses reported back to the main Abaqus solver from the UINTER user subroutine must be symmetric stresses, equal-and-opposite between interacting positions on two layers. For pairs of interacting layers deep within the body, this is acceptable: both layers are being acted on by semi-infinite bodies, either above or below. It is the boundary case, however, of layers close to the stamp, with which we are concerned. Examining the case of the very top layer of the van der Waals solid, interacting with the second layer, it is clear that symmetric stresses are not physical. While the top layer is being acted on by a semi-infinite body below it, the second layer is only being acted on from above by the top layer. Including the 7.6% contribution of the rest of the semi-infinite body imagines material that is not physically present, ignoring the very boundary condition that may prove interesting. Prescribing specific interlayer interactions and

⁵Relative contribution of non-interface layers: $\frac{\sum_{n=2}^{\infty} \frac{1}{n^4}}{\sum_{n=1}^{\infty} \frac{1}{n^4}}$, where n is the layer number ($n = 1$ is the nearest layer).

accounting for the stress as a function of interaction area, rather than volume, captures only physically present interactions. This approach has the drawback of imposing an artificial cutoff, in the sudden loss of interaction beyond some prescribed number of non-adjacent interlayer interactions. It also increases the number of calculations, as each layer participates in multiple individually-defined interlayer interactions. However, it facilitates easy inclusion of multiple sublayer interactions (see Figure 3.8).

3.2.4 Interlayer interaction derivation

We are interested in determining the local normal traction and stiffness as a function of the layers' separation. Starting from the Lennard-Jones potential describing the interatomic energy as a function of distance, we consider the case of a region of one layer, the layer of interest, interacting with an adjacent sheet which is infinite in lateral extent (Figure 3.2). We consider a single sublayer-sublayer interaction. The sublayer has particle density ρ_s (atoms/m²). The interlayer force is the multiple of the single-particle force by the number of particles in a given area. This direct multiplication, ignoring the lateral offsets of the individual atoms, is valid, as each atom interacts with the same infinite sheet. Thus, as long as the interlayer distance remains constant, all atoms experience the same traction. The Lennard-Jones interatomic potential for a single atom-atom interaction is given in Eqn. 3.1. For a layer in an x - y plane interacting with a sheet, also in an x - y plane, at normal distance D , we consider an annulus of interacting atoms of width dx , as x increases, to write the energy per unit area as:

$$\begin{aligned} w_{\text{center}}(D) &= 8\pi\rho_s^2 \int_{x=0}^{x=\infty} \varepsilon x \left[\left(\frac{\sigma}{\sqrt{D^2 + x^2}} \right)^{12} - \left(\frac{\sigma}{\sqrt{D^2 + x^2}} \right)^6 \right] dx \\ &= Q \left[\frac{\sigma^6}{D^{10}} \left(\frac{\sigma^6}{10} - \frac{D^6}{4} \right) \right], \end{aligned} \quad (3.2)$$

where the constants have been collected in $Q = 8\pi\rho_s^2\varepsilon$. Taking the derivative of the net potential in z , we find the normal component of force (per unit area) that governs the interlayer interaction:

$$F_{\text{center}}(D) = -\frac{\partial w}{\partial D} = -Q \left(\frac{\sigma^6}{D^{11}} \right) (D^6 - \sigma^6). \quad (3.3)$$

The specific stiffness at a given node, then, is:

$$k_{\text{center}}(D) = \frac{\partial F}{\partial D} = -Q \left(\frac{\sigma^6}{D^{12}} \right) (11\sigma^6 - 5D^6). \quad (3.4)$$

Though we are only interested in the normal components, by symmetry, the transverse component nonetheless cancels when the interacting layer may be treated as infinite. We address the case of edges in subsection 3.2.4.

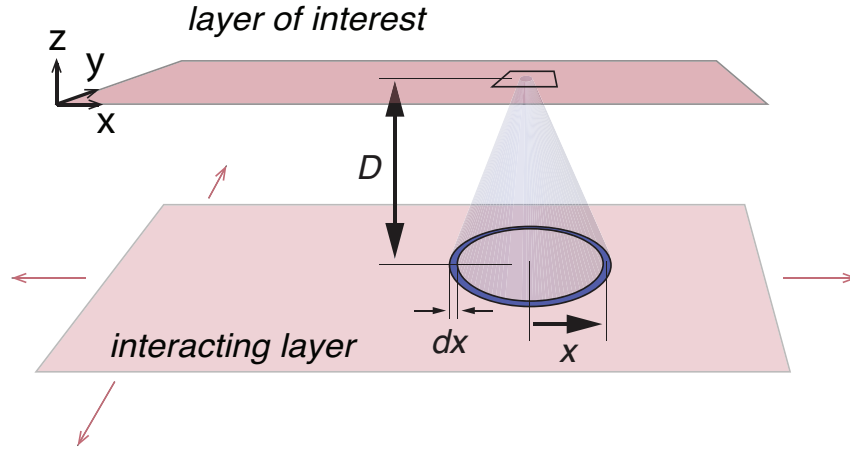


Figure 3.2: The traction produced as a result of the interlayer interaction is the sum of the tractions produced by atoms in the adjacent layer, at interlayer distance D , whose individual contributions can be determined by summing the contributions from atoms within an annulus of increasing radius x and infinitesimal width dx .

To determine the number of non-adjacent interlayer interactions to consider, we examine the tradeoff between the relative contribution of including an additional layer in the calculation and the penalty in terms of additional computational power. Matrix inverse operations scale as $\mathcal{O}(n^2)$. We compare the results of a simple model where varying numbers of interlayer interactions are considered⁶. In this simple model, the layers remain flat, and the combined energetic contributions of all van der Waals bonds (S-S, Mo-S, and Mo-Mo) are minimized. We calculate the interlayer separation, in a case with no load, and under a 1 GPa load. This system where every interlayer action is considered, the complete case, can be used to determine the fidelity of a model where fewer interlayer interactions are considered. In the case where only nearest-neighbor layer interactions are considered, the unloaded interlayer distances differ from those in the complete case by up to 0.13%, and differ from those in the case loaded to 1 GPa up to 1.25%. A case which considers second-nearest-neighbor interactions differs from the complete case by a maximum of 0.02% in an unloaded scenario, and 0.13% in a loaded scenario (Figure 3.3). In both the unloaded and loaded cases, considering second-nearest-neighbor interactions offers an order of magnitude improvement in fidelity to the complete case.

Thus, we consider up to the second-nearest-neighbor interactions in the model. Because each layer participates in interactions above and below, this cap allows us to account for a given layer's individual interactions with four other layers, which are in turn affected by their own nearest- and second-nearest neighbor layers.

⁶Many thanks to Haoye Sun for creating this model.

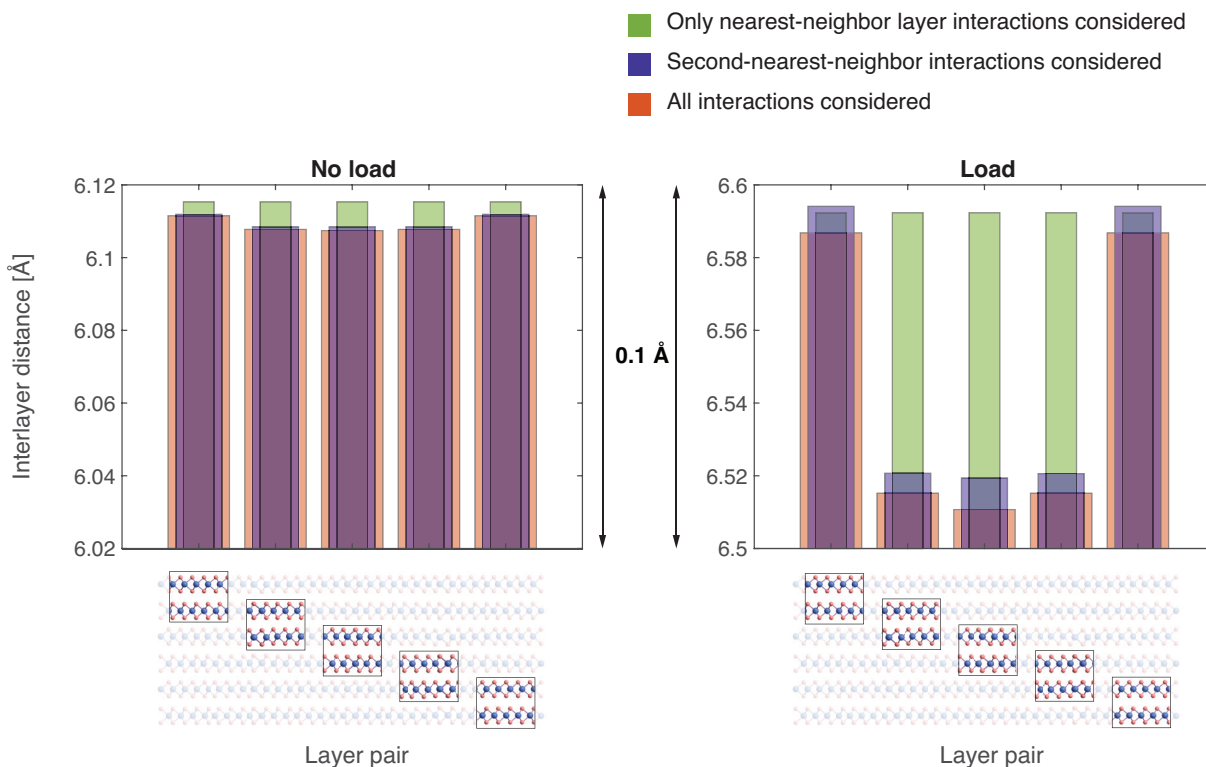


Figure 3.3: The differences in interlayer distance as the number of interlayer interactions considered, in a model which minimizes the sum of S-S, Mo-S, and Mo-Mo interaction energies as flat van der Waals layers move apart. The orange bars show the interlayer distances in the case where all fifteen interlayer interactions are considered (complete case). Two limited cases are calculated: (1) one in which only the five nearest-neighbor layer interactions considered (green bars), and (2) one in which both first- and second-nearest-neighbor layer interactions are considered, for a total of nine interactions (blue bars). Case (2) shows an order of magnitude closer match to the complete case, relative to case (1), even when the layers experience a 1 GPa load and undergo displacement.

Edge definition

For nodes within a certain distance of the x -direction edge of a layer, the interlayer force in the z -direction is reduced, relative to the body force on a central node. To determine the size of the edge region, we calculate the dependence of the force on the radius of interacting atoms considered.

It is necessary to determine the distance from the edge at which a node stops “seeing” an infinite plane, and becomes sensitive to the limited lateral extent of the adjacent layers. The force on a point in the x - y plane can be split into the sum of the interactions acting from the $-x$ direction, and the sum of the interactions in the $+x$ direction (the blue and orange semi-circles, respectively, in Figure 3.4). For a point nearing an edge in the $+x$ direction, we consider the $-x$ extent of the adjacent layers semi-infinite, and the force contribution in the z -direction may be determined by halving the force on a central region (Eqn. (3.3)). However, in the $+x$ direction, the point is now interacting with a sheet of finite extent. We repeat the integration used to arrive at Eqn. (3.2), restricting the lateral (x -) extent of the sheet to R rather than ∞ :

$$\begin{aligned}
 w_{\text{edge}}(D) &= 8\pi\rho_s^2\varepsilon \int_{x=0}^{x=R} x \left[\left(\frac{\sigma}{\sqrt{D^2+x^2}} \right)^{12} - \left(\frac{\sigma}{\sqrt{D^2+x^2}} \right)^6 \right] dx \\
 &= Q \left[\frac{-\sigma(2\sigma^6 - 5(x^2 + D^2)^3)}{20(x^2 + D^2)^5} \right]_0^R \\
 &= Q \frac{\sigma^6}{20} \left[2\sigma^6 \left(\frac{1}{D^{10}} - \frac{1}{(R^2 + D^2)^5} \right) + \frac{5}{(R^2 + D^2)^2} - \frac{5}{D^4} \right], \quad (3.5)
 \end{aligned}$$

where, again, the constants are collected in $Q = 8\pi\rho_s^2\varepsilon$, composed of terms for the number of interacting atoms per unit area in the acting layer, $2\pi\rho_s$, the scaled energy parameter ε of Lennard-Jones potential for the given interatomic pairing (here, sulfur-sulfur), and the density of atoms in the layer being acted upon, ρ_s . This gives stress and stiffness:

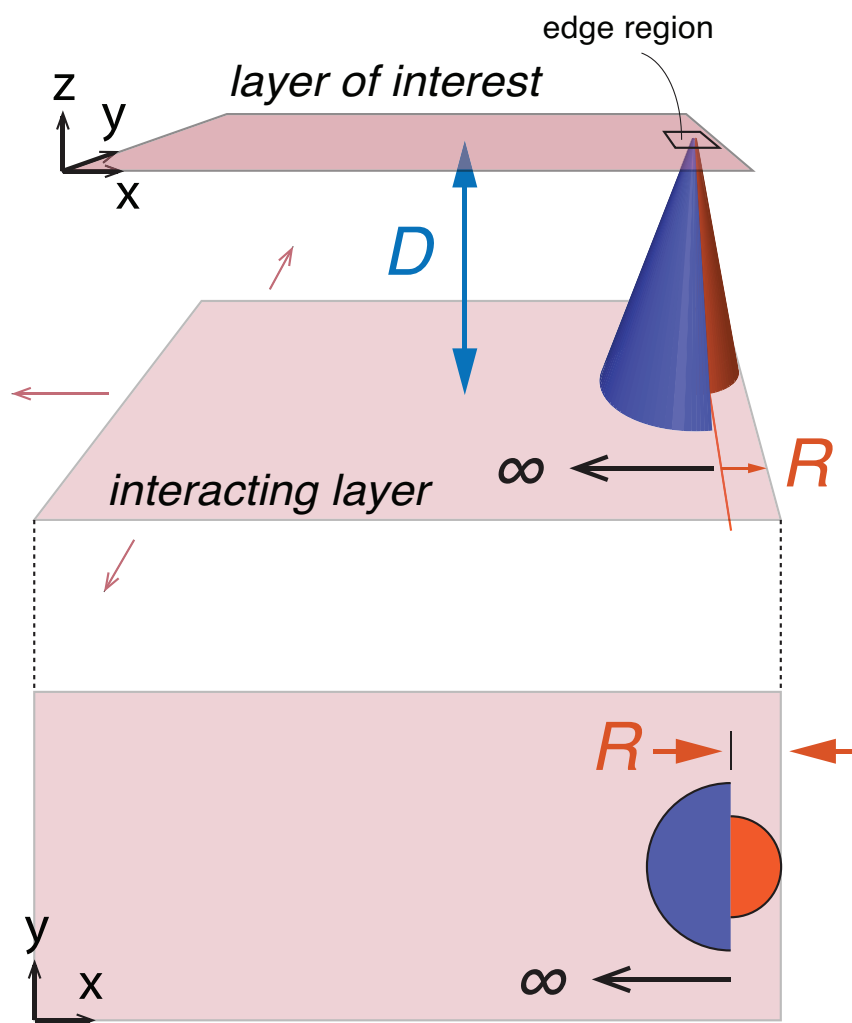


Figure 3.4: The force on an edge region is decomposed into two contributions: one from the semi-infinite radius of atoms towards the center of the layer, shown in blue, and one from the finite radius R of atoms from the region to the boundary of the layer, shown in orange.

$$F_{\text{edge}}(D) = -\frac{\partial w}{\partial D} = -Q \sigma^6 \left[\sigma^6 \left(\frac{D}{(R^2 + D^2)^6} - \frac{1}{D^{11}} \right) - \frac{D}{(R^2 + D^2)^3} + \frac{1}{D^5} \right] \quad (3.6)$$

$$k_{\text{edge}}(D) = \frac{\partial F}{\partial D} = -Q \sigma^6 \left[\sigma^6 \left(\frac{-12D^2}{(R^2 + D^2)^7} + \frac{1}{(R^2 + D^2)^6} + \frac{11}{D^{12}} \right) - \frac{1}{(R^2 + D^2)^3} + \frac{6D^2}{(R^2 + D^2)^4} - \frac{5}{D^6} \right], \quad (3.7)$$

Eqns. 3.5-3.7 are simply the edge component; the total interlayer force and stiffness acting on a node at the edge of a layer are $F = \frac{1}{2}(F_{\text{center}} + F_{\text{edge}})$ and $k = \frac{1}{2}(k_{\text{center}} + k_{\text{edge}})$, respectively.

3.2.5 Model definition in Abaqus

Material definitions

For the purposes of this model, the elastic properties of single-layer MoS₂ were chosen from a [centralized database](#)⁷ of material properties calculated using density functional theory (DFT) [19]. Values were converted from the reported units of N/m to GPa by assuming a thickness for the single MoS₂ layer. The legitimacy of this approach depends on the validity of the model assumption that there is no appreciable change in the layer's thickness during deformation. The values used in the model are given in Table 3.3. A summary of reported elastic constants for monolayer MoS₂, from both density functional theory (DFT) calculations and experiments, can be found in Table 3 of ref. [155]. Of note, experimentally reported values of the in-plane stiffness—used in lieu of elastic modulus—are substantially (50%) larger than predicted values. Because the material is orthotropic, all off-diagonal elastic constants other than C_{1122} , C_{1133} , C_{2233} , and their symmetric counterparts are zero⁸.

The stamp material was assumed to be orthotropic and homogeneous. Its Young's modulus was varied as a parameter of study, from 100 kPa to 100 MPa, while its Poisson's ratio was fixed at 0.3.

⁷<https://www.ctcms.nist.gov/~knc6/JVASP.html>

⁸The following constants are zero-valued: C_{1123} , C_{1131} , C_{1112} , C_{2223} , C_{2231} , C_{2212} , C_{3323} , C_{3331} , C_{3312} , C_{2331} , C_{2312} , C_{3112} .

Table 3.4: Dimensions of the model components.

		Layer(s)	Stamp
Dimensions	Length (x)	1.0 μm	1.5 μm or 3 μm
	Depth (y)	100 nm	100 nm
	Height (z)	3.2 \AA	15 μm
	Initial spacing (z)	2.9 \AA	—
Element type		S4	C3D8R

Elements and meshing

To model thin layers, Abaqus offers both membranes and shell elements. Shell elements were chosen, as membranes cannot sustain bending moments. The bending stiffness of the van der Waals layers is an important component of the problem: as the stamp imposes a deflection on the top layer, the response of subsequent layers is ultimately a balance between the binding energies it experiences in relation to other layers, and the energetic penalty imposed on deflection by the layer’s own bending stiffness. Shell elements may be prescribed a thickness, which gives the elements a commensurate bending stiffness calculated from the elasticity tensor of the associated material.

The stamp was meshed with linear 8-node 3D stress linear brick elements (C3D8R), and the layers were meshed with linear 4-node 3D shell elements capable of sustaining finite membrane strains (S4). The shell section associated with the layers was assigned three thickness integration points. In order to account for the difference in force acting on edges, the node-to-node pitch is reduced at the x -direction edge of features (see Figure 3.7, detail in the following section), and the mesh density on the bottom face of the stamp was varied along x to mimic the mesh density of the contacting layer surface.

Dimensions of each component of the model are given in Table 3.4 and Figure 3.9. The stamp thickness is chosen based on the description of the thickness of the pressure-deformable thermal release layer in Nitto REVALPHA[®] thermal release tape, which has a “preferable” lower thickness bound of 15 μm [115].

Contact force definition and interaction boundary conditions

Discussion to this point has assumed a fully three-dimensional model. While three-dimensional elements were chosen, y -direction edges are neglected, approximating a 2D case. The stamp/layer geometry and the boundary conditions reinforce this: the stamp and layers have the same y -extent (Table 3.4 and Figure 3.9), and the layer edges along the x -axis are prescribed to undergo no rotation about the x -axis, implying continuity (Figure 3.9). Since there is no variation in the y -direction, the choice of y -depth is arbitrary, and is small (100 nm) to minimize computation time.

Because forces are reported back to Abaqus per unit area, the interlayer force is treated as an evenly distributed stress over the area associated with the node.

It is necessary to know the width of the edge region in order to ensure a sufficiently fine mesh at the edge. Center regions may be meshed more coarsely, which reduces the computational power and run time of the model. The width of the edge region was determined by considering a single atom interacting with a disk of atoms in an adjacent layer, with radius R (Figure 3.4). As R approaches ∞ , the edge case converges to the case of a central atom. The force on the atom was calculated using Eqn. 3.6. This force is also a function of the current interlayer distance, D . Starting from the initial, equilibrium interlayer separation, the variation of edge force with radius was considered at several interlayer displacements up to a nearest-neighbor sulfur sublayer distance of 3.9 Å, a 1.0 Å extension from equilibrium, at which point the variation with interlayer distance was negligible (Figure 3.6(a-b)). Because the direction of the interatomic force switches from repulsive to attractive as a function of distance, a small disk radius R at close range D will experience an initial repulsive force, which may switch to attractive as more atoms are considered (increasing radius R) so long as the interlayer distance D is large enough. As seen in Figure 3.6(a), an edge with interlayer displacement $D = 3.2$ Å (equilibrium displacement + 0.3 Å) experiences a repulsive force when R is small, which switches to a net attractive force as the radius widens to include sufficient atoms in the adjacent layer exerting an attractive pull on the edge atom. For all interlayer distances $D \geq$ equilibrium, the force on an edge atom has reached at least 99.99% of the force a central atom experiences at $R = 2.02$ nm, (Figure 3.6(b)). In the model, the node spacing in the edge region is prescribed to be 1 nm, so that the gradation of force within the 2 nm edge region may be resolved over multiple nodes (Figure 3.7).

The application of Eqns. 3.6-3.7 assumes that the area associated with each node is small compared with the size of the edge region (effectively, that each point in the region is equally close to the edge). This assumption is worth investigating. Each edge element, 1 nm wide, has four integration points, but the `UINTER` subroutine responsible for calculating edge forces is called only at the nodes. By integrating the forces observed at the edge node and at the 1 nm node across the element, the strength of the repulsive force that would be experienced by the ~two atoms⁹ spaced between 0-1 nm from the edge will be underestimated. However, the direction of the net force at the node will be correct, at all interlayer spacings (the integral of each curve in Figure 3.6(b), from 0 to 1 nm, has the same directionality as an integral which only considers the 0 nm and 1 nm data points). Critically, interlayer stiffness converges more rapidly than interlayer force, and the integration error is even less pronounced.

The radius of interacting atoms to consider when calculating the force and stiffness at a given edge node is determined by the absolute x location of the node. The radius R is then the distance from the node to the original boundary of the layer. This setup assumes very large bend radii at the edges—effectively, a small angle assumption—such that the deformed and undeformed edge x -positions are not significantly different. Only

⁹Along the so-called zig-zag edge of MoS₂, the within-layer sulfur-sulfur spacing is 3.15 Å, giving four sulfur atoms within 1 nm in each sublayer.

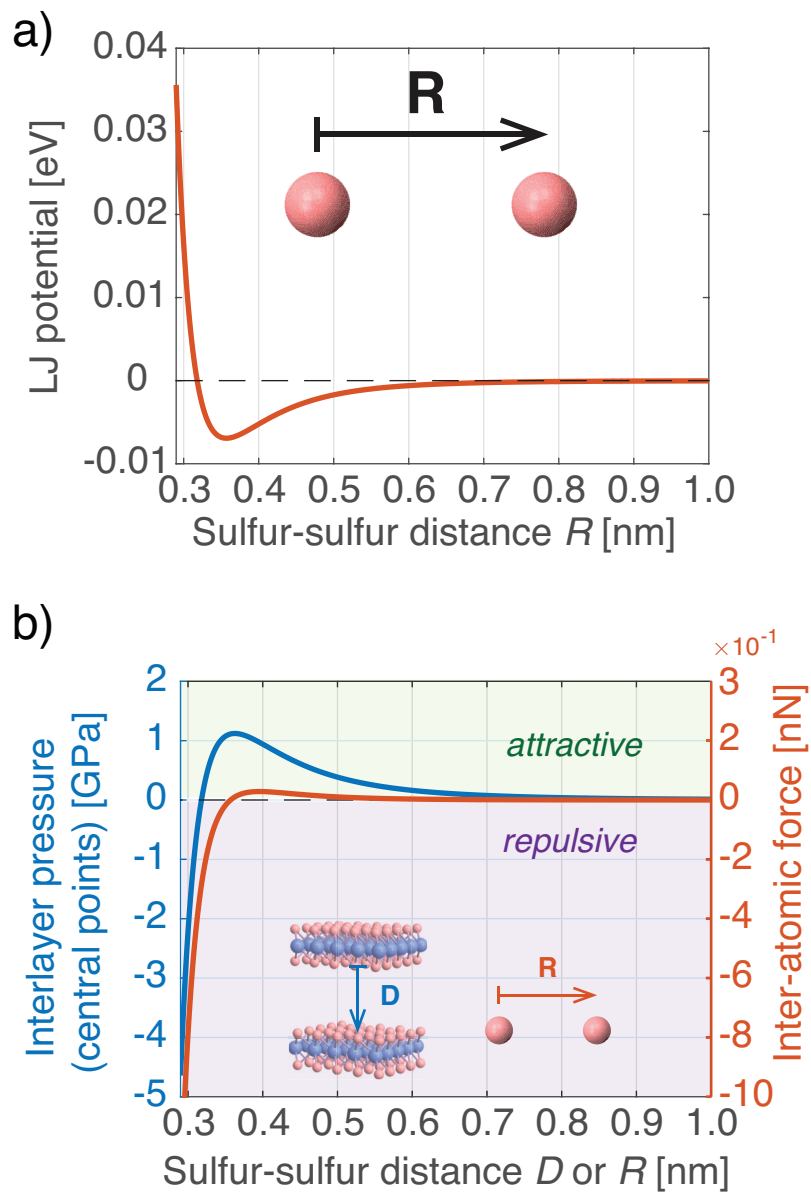


Figure 3.5: (a) The van der Waals potential energy between two sulfur atoms as a function of their distance, as described by a Lennard-Jones (LJ) potential. (b) The interlayer force per unit area as a function of the interlayer distance between two MoS₂ layers, left axis, and the van der Waals force between two sulfur atoms as a function of their distance, right axis.

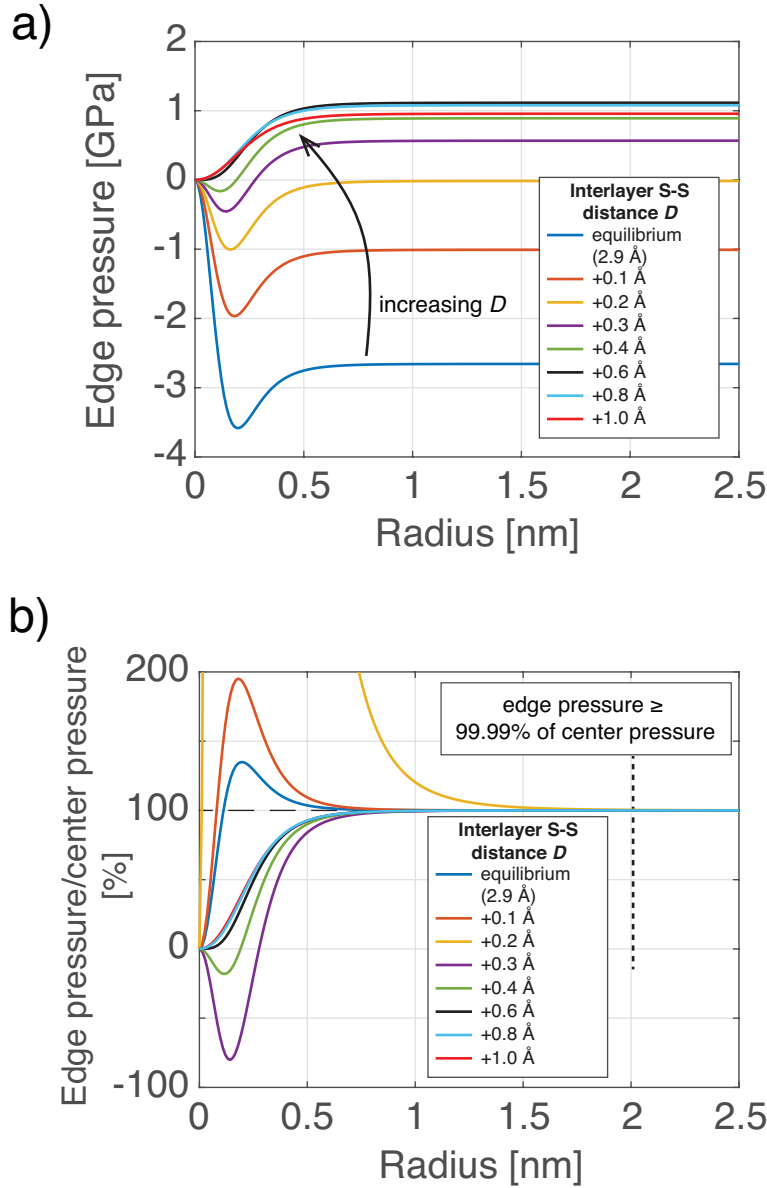
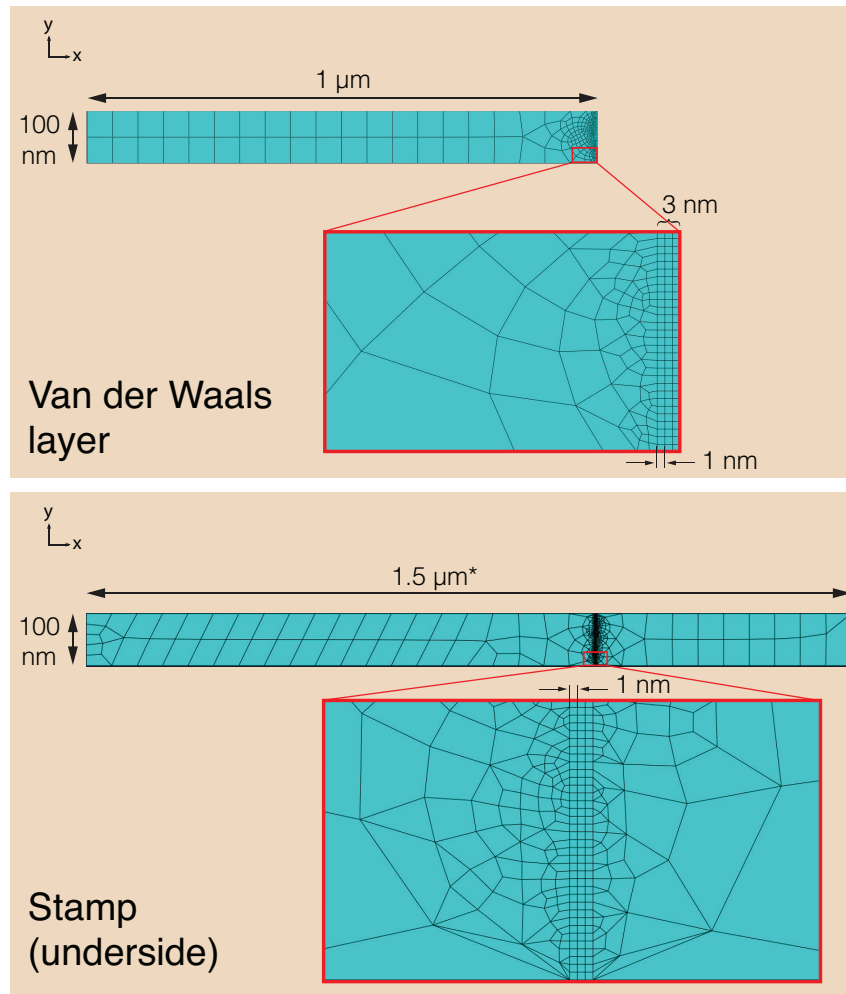


Figure 3.6: (a) The changing pressure that an edge region experiences as it interacts with an increasing radius of atoms in the adjacent layer. The different lines correspond to different interlayer displacements, starting from the equilibrium separation of $6.1 \text{ \AA} \text{ Mo-Mo} = 2.9 \text{ \AA} \text{ S-S}$. Negative pressures are repulsive, while positive forces are attractive. (b) The same data shown in (a), here shown as a percentage of the pressure that a non-edge atom, interacting with a radius of atoms of $R = \infty$, experiences. In all cases, the force on an edge interacting with a circle of atoms of radius $R = 2.02 \text{ nm}$ has achieved 99.99% of the force on a central atom. Note that at interlayer S-S displacements of equilibrium + 0.3 \AA and equilibrium + 0.4 \AA , the directionality of the pressure switches from repulsive to attractive as additional atoms are considered.



*1.5 μm corresponds to 1 μm interfeature spacing.
 This dimension is 2.0 μm or 3.0 μm when interfeature spacing is larger.

Figure 3.7: Meshes on the van der Waals layer (top) and the underside of the stamp (bottom). The mesh density is increased at the edge of the van der Waals layer so that rapidly varying forces may be resolved over the short (~ 2 nm) region which may be considered the edge. The mesh on the stamp mimics the mesh on the layer in this region to prevent warping—the top van der Waals layer is tied to the stamp.

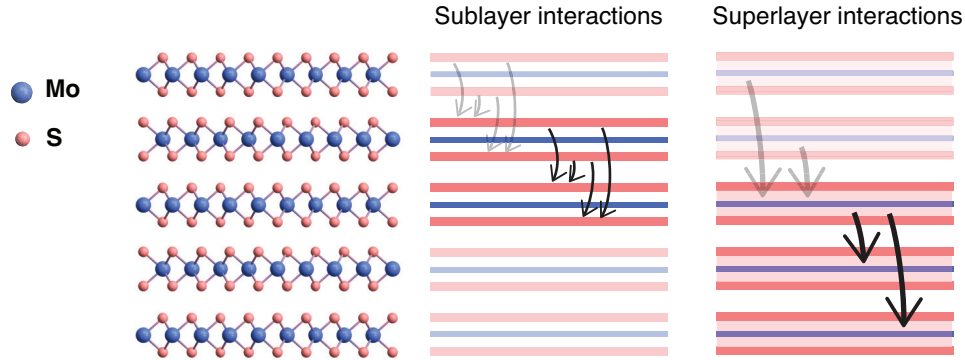


Figure 3.8: Interlayer interactions included in the model. Between a given pair of superlayers, all four chalcogen sublayer interactions are considered (left). Each superlayer interacts with up to four other layers, two above and two below, depending on the position of the layer (right). The top superlayer, for instance, only interacts with the two layers below it.

half the force on an edge node is calculated from the node position using a finite radius (Eqn. 3.6); the other half is the contribution from the semi-infinite sheet (Eqn. 3.3).

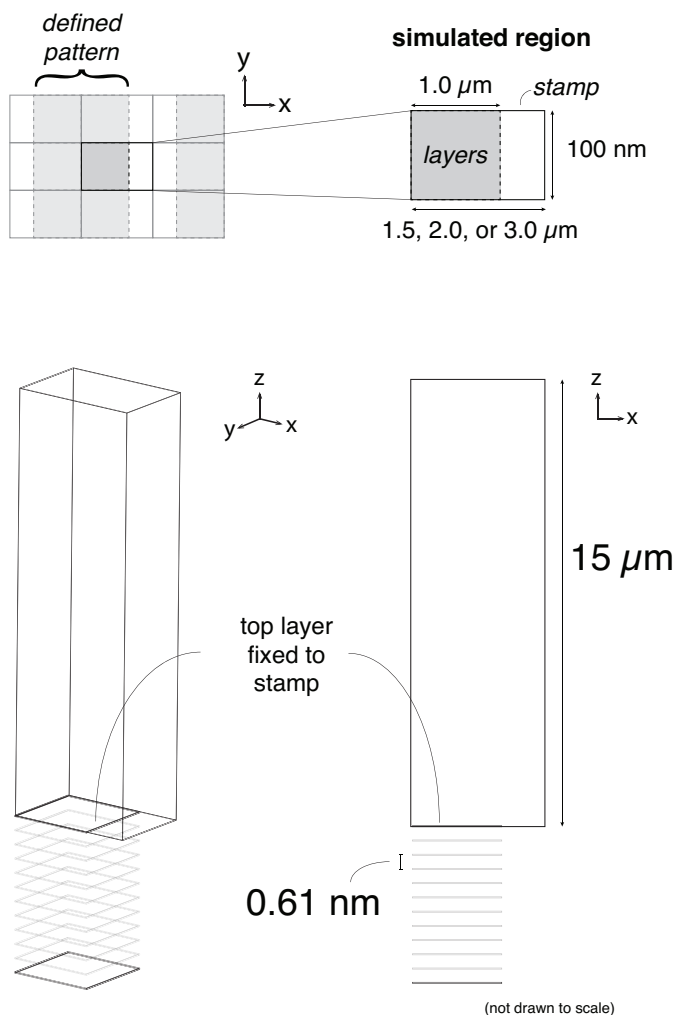
The shell elements representing the van der Waals layers have a finite thickness, and possess both a bottom and top surface. Here, bottom surfaces serve as masters, and top surfaces as slaves, as the interactions are prescribed from the top layer downwards. Because the interlayer stresses are symmetric, both master and slave surfaces experience the same stress magnitude due to a given interaction. The surfaces are, effectively, the locations of the chalcogen sublayers. Interlayer distances are calculated using the surface-surface master-slave distance, the distance between the nearest chalcogen sublayers in the two distinct layers. The interatomic interactions considered are not limited to the nearest chalcogen sublayers. Each interlayer interaction is composed of four separate chalcogen (sulfur) interactions (see Figure 3.8). Their contributions are not screened and may be linearly superimposed. Knowing the distance of the nearest-chalcogen-sublayers is sufficient to calculate all four interactions, assuming no elastic expansion in the thickness of the layers themselves.

System boundary conditions

The study of edge effects becomes particularly relevant, and interesting, in the case of patterned layers of van der Waals material, where the edge shape and location may be dictated during the patterning process. Simulating an entire patterned array is unnecessary and computationally expensive; because we are concerned with the behavior of a single edge, we may restrict the simulation size and impose boundary conditions that reflect the physical reality of a patterned system.

The deformation of the components is constrained so that the periodicity of the assembly is retained. To ensure the stamp is continuous, the slope of the stamp displacement

a) Dimensions



b) Boundary conditions

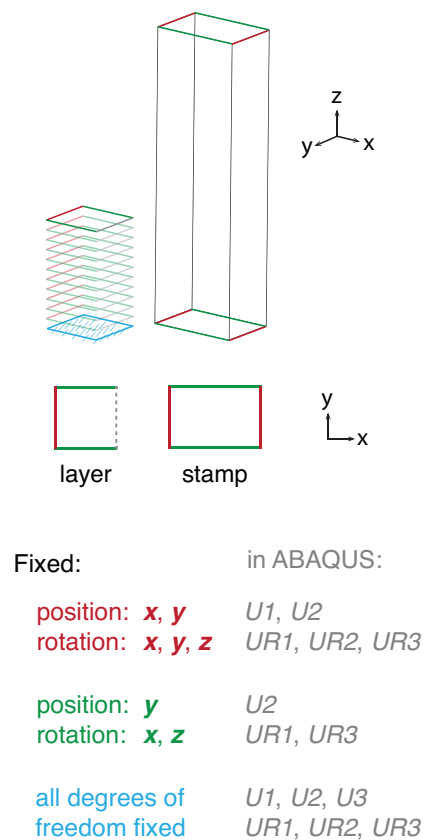


Figure 3.9: Dimensions and boundary conditions of the model. Individual subsections of the model are tiled (a) to mimic periodic strips of multilayer van der Waals stacks. The tiling is achieved by prescribing boundary conditions (b) that ensure continuity at the edges of the model. Further, the bottom van der Waals layer is fixed in its initial position, as a mounted piece of bulk material would be in experimental conditions. The top van der Waals layer is fixed to the stamp (in other words, perfect adhesion is assumed).

is required to be zero in all directions at the boundaries¹⁰. This is achieved by fixing the rotation of the boundary edges in the x - y plane at zero. The van der Waals layers are only partially continuous. The system is modeled such that the van der Waals layers have three edges in common with the stamp (Figure 3.9). The edges of the van der Waals layers flush with edges of the stamp are also constrained in rotation. The remaining edge is free to rotate about its axis, corresponding to a bend in the layer (Figure 3.9(b)). Finally, the top and bottom van der Waals layers are further restricted: the bottom van der Waals layer is completely fixed, representing mechanical fixturing of the to-be-exfoliated stack. Perfect adhesion between the top van der Waals layer and the stamp is assumed, resulting in a tie constraint between the top layer’s top surface and the bottom surface of the stamp. The displacement of the top van der Waals layer is equivalent to and coincident with the deformation of the bottom of the stamp. The boundary conditions are illustrated in Figure 3.9.

3.2.6 Validation with molecular dynamics

Because of the difficulty of validating a model involving sub-Å displacements experimentally, validation of the model is performed by comparison to a more computationally expensive, physically robust model, composed solely of van der Waals layers. Specifically, the exfoliation pressure in the finite element model was compared to the exfoliation pressure observed in a molecular dynamics model.

In molecular dynamics simulations, run in LAMMPS at 0 K, consisting of eight layers with periodic boundary conditions, the exfoliation pressure was observed to be $0.006 \text{ eV}/\text{Å}^3 = 0.961 \text{ GPa}$. A finite element model was constructed consisting only of van der Waals layers. Edge effects were not considered. The bottom layer was fixed and the top layer pulled away in a displacement-controlled manner. At each step, the contact pressures experienced by each layer were noted. The pressures increased, then fell, with additional top layer displacement. The largest observed contact pressure was 1.22 GPa. This corresponds to the exfoliation pressure of the system, and represents a 27% difference from LAMMPS results, indicating moderate correspondence between the finite element model and the molecular dynamics model, the latter of which accounts for each interatomic interaction.

Of note, in a gradually stepped finite element model controlled by the displacement of a stamp, and now considering edges, the contact pressure observed immediately before failure was $9.565 \times 10^{-10} \text{ J}/\text{m}^3 = 0.9565 \text{ GPa}$. This 0.5% difference from LAMMPS results indicates superb correspondence between the finite element and molecular dynamics models.

¹⁰While y - and z -edges must have zero slope to preserve continuity, the limitation on the x -edge is unique to a 2D simulation. The x -axis deflection of the stamp would be expected if the layer possessed an edge along x as well as along y .

3.3 Results

Ultimately, we are concerned with layer selectivity. Exfoliation is a crack initiation and propagation event, and determining the number of layers exfoliated is a matter of identifying at which interface this crack propagation occurs. Therefore, the failure criterion is crack initiation. Once an interface reaches an interlayer displacement sufficiently large that the layers may be considered separated at that precise location, a crack will preferentially propagate between those two layers. This can be understood in terms of energetic favorability, akin to achieving a critical energy release rate G_C using Griffith's criterion. The bulk Griffith's criterion balances surface energy against elastic energy; here, both are the van der Waals energy. The surface energy of a layer is equivalent to half the minimum total van der Waals energy of two layers in contact, while the elastic energy of the bond is its van der Waals potential. The crack expands once additional interlayer displacement (in other words, cracking) reduces the free energy of the system.

The differential energy per unit separation between layers is the interlayer force, which is a scalar multiple of the pressure shown in the blue curve in Figure 3.5(b). Once a region of one layer is slightly past the interlayer distance of maximum attraction, it will strictly separate further; the interlayer stiffness has become negative. This threshold occurs at a sulfur-sulfur interlayer distance of 3.61 Å, which is 0.7 Å larger than in MoS₂'s equilibrium state. We concern ourselves only with nearest-neighbor layers to determine this threshold: once nearest layers have entered the monotonically-decreasing attractive regime, all other interlayer interactions acting on a given layer have not only entered this regime but are considerably weaker. Thus, the nearest layer distance acts as a critical condition.

When the stamp is displaced upwards (+ z), the interlayer stiffness of the van der Waals layers exerts a downwards (- z) force on a portion of the stamp's bottom face. The fact that the downwards force only acts on a portion of the stamp's bottom surface is critical: the curvature of the stamp's bottom surface between the loaded and free regions induces a bend in the layers. This bend shape is influenced by the free distance between loaded regions, thus the inter-feature spacing in the pattern is expected to play a role. Due to the tie constraint between the top van der Waals layer and the region of the stamp's bottom surface it contacts, the shape of the top layer perfectly matches the bottom of the stamp. We are then interested in how this bending deformation is distributed between layers. Each layer faces a tradeoff between its bending and binding energies, and the binding energy varies nonlinearly with distance (Figure 3.5(a),(b)).

3.3.1 Displacement of layers as a function of stamp modulus

Three values of the stamp's Young's modulus and two values of inter-feature spacings were tested. The details of the experimental parameters are given in Table 3.5. The range of stamp moduli span possible stamp stiffnesses, which are typically on the order of 1 MPa. Each combination of stamp stiffness and spacing was subjected to a displacement-controlled step, induced by a prescribed quasi-static 5 nm displacement of the top surface

of the stamp. A displacement-controlled configuration was chosen in order to examine the distribution of displacements between layers. The choice of stamp displacement is meant to capture behavior on the cusp of exfoliation. Across all combinations of moduli and spacings tested, a 5 nm stamp displacement sits in the pre-exfoliation regime, and in some cases exfoliation occurs just after the stamp displacement has passed 6 nm.

Critically, interlayer stiffness decreases as a function of distance. The interlayer interface identified as largest at the 5 nm displacement step is also weakest. This interface requires the least energy to separate and are thus where exfoliation will occur.

In all cases, the top layer/second layer interface experiences the largest interlayer distance, and the bottom layer/second-to-bottom layer interface experiences the second-largest displacement. This implies that, in all cases tested, a 0 K experiment would be expected to produce crack propagation and interface failure between the top and second layers, resulting in monolayer exfoliation. However, there are different degrees of selectivity: in all cases, a softer stamp produces the most pronounced difference between the top/second layer interlayer distance and all other interlayer distances. The selectivity, determined by the difference between the first layer/second layer gap size and the second-largest interlayer gap size, is shown in Figure 3.10. The different interlayer distances at each combination of interfeature spacing and stamp modulus are shown in Figure 3.12.

The layer-to-layer variation in interlayer distances, which we expect to dictate exfoliation interface, is superimposed with thermal fluctuations. Under no load, the thermal fluctuations, which are uncoupled layer-to-layer, result in a sulfur sublayer position uncertainty of $\pm 0.07 \text{ \AA}$ out-of-plane. The magnitude of the fluctuations increases when the layers are placed under a normal load. The interlayer distance discrepancy resulting from a load on the stamp is $< 0.02 \text{ \AA}$. At a single point along the edge, the layer selectivity introduced by the stamp is overridden by the interlayer distance variations resulting from thermal fluctuations. However, thermal fluctuations are uncoupled, and the disparate phases of each atom's fluctuation means these fluctuations will not result in a net displacement of the edge.

3.3.2 Displacement of layers as a function of interfeature spacing

The impact of interfeature spacing could be expected to asymptotically approach the case of infinite interlayer spacing, suggesting that sensitivity to interlayer spacing is nonlinear with increases in spacing. Ultimately, the different stamp moduli sit in different sensitivity regions, as measured by the variation in the total stack displacement as a function of interfeature spacing. Large decreases in the total stack displacement as spacing increases indicates higher sensitivity to interfeature spacing. The stiffest stamp is most sensitive. As the interfeature distance increases from $1 \mu\text{m}$ to $4 \mu\text{m}$, both the 100 kPa and 1 MPa stamp models exhibit a decrease in the total van der Waals stack edge displacement of $< 0.01\%$. The total stack displacement under a 100 MPa stamp decreases 0.26% over the same range of interfeature spacings. The selectivity variation as a function of interfeature spacing is shown in Figure 3.11. From a qualitative standpoint, the out-

Table 3.5: Parameters tested. Each combination of modulus and interfeature spacing was modeled.

Young's moduli	Inter-feature spacings (feature:spacing ratio)
100 kPa	1 μm (1:2)
1 MPa	2 μm (1:1)
100 MPa	4 μm (2:1)

of-plane displacement variations along the stamp bottom surface increase in amplitude with increasing interfeature spacings, translating into larger z -direction displacements at the edges of the layers.

However, ultimate sensitivity is different from top interface sensitivity; these small changes may be disproportionately concentrated in the top interface. Though this appears to be the case, the differences still amount to a negligible effect. 100 kPa and 1 MPa stamps show a small increase in sensitivity as interfeature spacing increases, but this increase amounts to only a 0.01% difference between the top interface distance and a center interface distance. Though suggesting larger interfeature spacings are preferable, this sensitivity increase is small. A stiffer stamp, much smaller interfeature spacings, or a combination thereof would amplify the sensitivity to interfeature spacing.

3.4 Conclusions

A softer stamp appears strictly preferable for inducing a larger marginal interlayer displacement between the first and second van der Waals layers. This preference is absolute at 0 K. Increasing temperature introduces an increasing noise floor due to thermal fluctuations. Thermal fluctuations are one of several extrinsic factors that will impact whether the effect of the stamp stiffness is observed empirically. Crystal defects, the direction of loading relative to the local orientation of the crystal planes, and topographical inconsistencies in the bulk crystal will all impact the ability of the stamp to transmit stress and thus interlayer strain in the manner of the idealized system modeled here.

Though their deformability is desirable for producing bending in van der Waals layers, soft stamps pose manufacturing difficulties for the production of patterned van der Waals features. As discussed in Chapter 2, the modulus of the stamp is one factor dictating the onset of roof collapse, when the surface of the stamp deforms across an intentional cavity. The cavity may be used to offset the stamp from unpatterned regions of material. Thus, a tradeoff exists between the desirability of a stiffer stamp to prevent roof collapse; the ability to produce a larger offset, or cavity, making roof collapse more difficult; and the usefulness of a soft stamp in introducing interlayer discrepancies that may facilitate monolayer exfoliation. A variable apparent Young's modulus could be achieved by taking advantage of the viscoelasticity of the stamp: a high strain rate could be applied when a high Young's modulus is desirable, and vice versa. Viscoelasticity is already leveraged

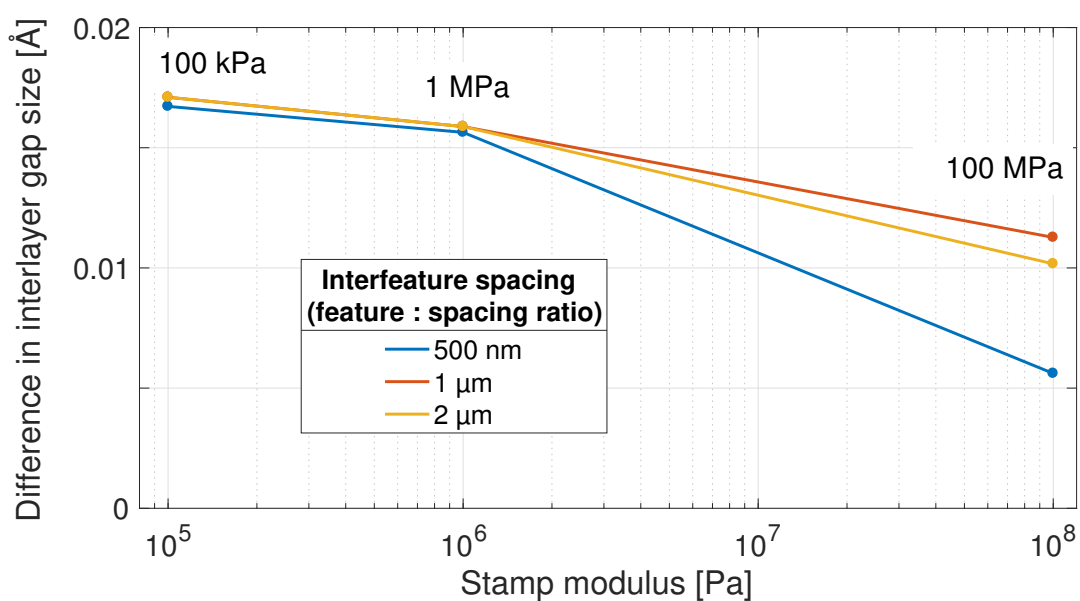


Figure 3.10: Exfoliation interface selectivity as a function of the Young's modulus of the stamp. In each case, the top layer/second layer interface had the largest interlayer distance, at the edge of the layer. The selectivity, then, is the difference between this (largest) interlayer distance, and the interlayer distance of the second-largest layer-layer gap. In all case, this second-largest gap occurred between the second-to-bottom and bottom van der Waals layers. Across all interfeature spacings, a softer stamp offers the greatest selectivity and is thus preferable.

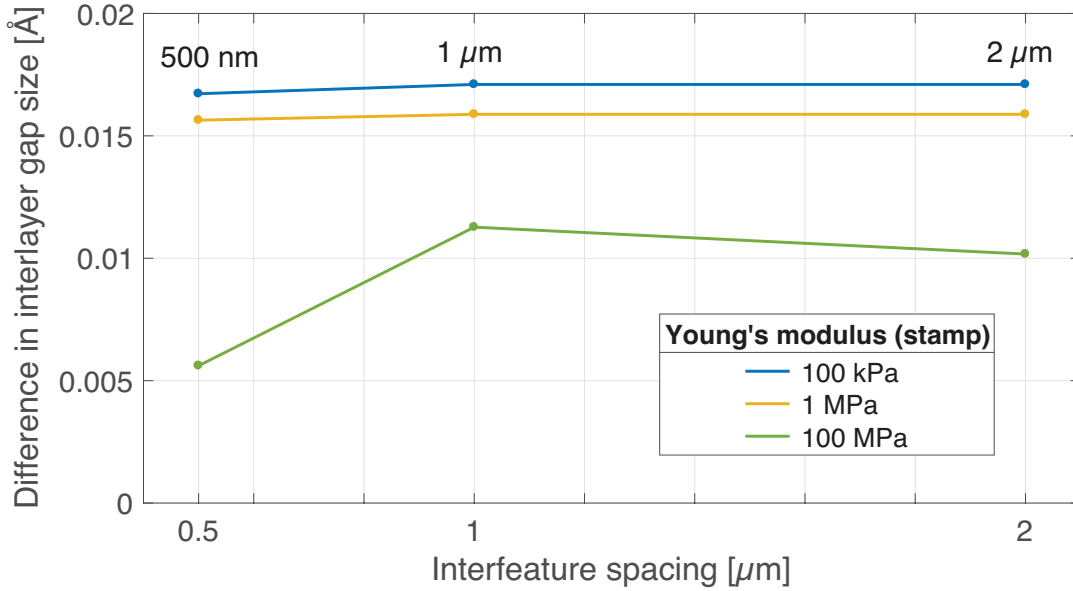


Figure 3.11: Exfoliation interface selectivity as a function of the lateral spacing between features in the van der Waals layers. The variation in selectivity is clearly miniscule for both 100 kPa and 1 MPa modulus stamps (blue and yellow lines), though larger interfeature spacings offer slightly more selectivity.

to switch the adhesive properties of the stamp during transfer, in order to both pick up a van der Waals layer from a stack and deposit the van der Waals layer on a substrate [118].

The results of this study seem to indicate that arbitrary layer selection is yet unachievable. For instance, a larger interlayer gap could not be preferentially introduced between, say, the third and fourth layers. The van der Waals attraction between the layers and the stamp was neglected in this model. A sufficiently strong van der Waals attraction could alter the displacement of the non-top layers. As yet, Lennard-Jones parameters for the constituent interatomic interactions between, say, a polydimethylsiloxane (PDMS) molecule and sulfur atoms are not readily available.

The edge region is nanometers wide. Thus, features on the order of 100 nm wide or larger are much wider than the edge region, and the feature size itself is unlikely to play a role. However, the effect of interfeature spacing is slight, but apparent. It is not known how the dependence on interlayer distance distribution with interfeature spacing scales. Much smaller interfeature spacings could significantly exacerbate the observed trend, of decreasing interlayer selectivity with decreasing interfeature spacing. However, larger interfeature spacings appear more desirable, as they induce a greater discrepancy between the top layer/second layer interlayer distance and all other interlayer distances.

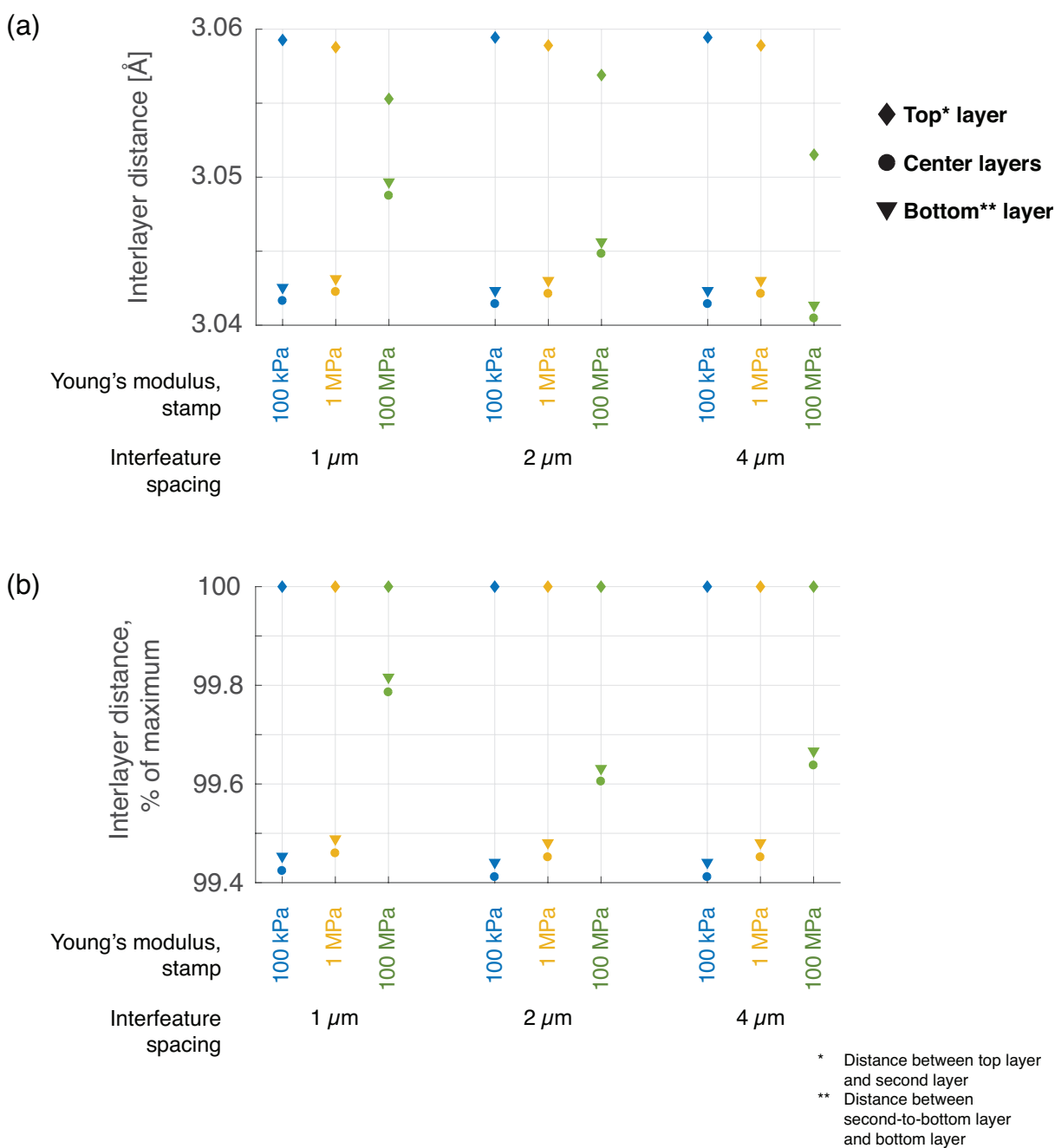


Figure 3.12: Van der Waals interlayer distances, when the top of the stamp is displaced 5 nm, as a function of both the spacing between features and the modulus of the stamp, plotted on both (a) absolute and (b) relative scales. The discrepancy in center interlayer distances is negligible. In all cases, the top layer/second layer interface experiences the largest interlayer distance, and the bottom layer/second-to-bottom layer interface experiences the second-largest displacement.

Chapter 4

Conclusions and Future Work

4.1 Contributions of this work

While single molecule layers of van der Waals materials can be grown and patterned on a substrate, the future fabrication of van der Waals heterostructures will require the ability to select and deposit pre-patterned arrays of van der Waals monolayers, ideally from stacks of arbitrary thickness. This work introduces a method for doing so, which was previously unachievable. Already, the process developed in Chapter 2 has been deployed to produce arrays of multi-material van der Waals heterostructures, with feature yields up to 45%. Though the yield metrics introduced in this work are simple, they provide a benchmark against which to measure process improvement and progress in the realm of monolayer pattern fabrication, and fix an eye on future mass production of van der Waals heterostructures. Though the work reported is the first demonstration of direct exfoliation of semiconducting van der Waals monolayer patterns, currently, yield of the process does not achieve the standard of mass-manufacturability. Improvements to transfer, substrate preparation, and liquid processing steps are needed. Moreover, though the process relies on existing techniques and materials in a standard CMOS-fabrication cleanroom, the method is cumbersome and lengthy. There are opportunities for the process to be streamlined; for instance, perhaps a more elegant process could eliminate the need for both photoresist handles and a transfer stamp by combining the two.

The introduction of a model which couples the nanoscale, non-linear behavior of van der Waals materials to the deformation of macroscale systems provides a means of examining multi-scale interactions, between both different length scales and different stiffness scales. Given the ubiquity of stamping methods in current van der Waals device production, and the necessity of material transfer in creating heterostructures, such a model could be deployed to uncover simple design rules for nanofabrication of van der Waals arrays. This model is a further step in the nascent and limited body of work on the influence of stamp mechanics on the yield of van der Waals transfer processes. The insights offered by the model carry manufacturing implications about the choice of stamp, and highlight a tradeoff between the desirability of a soft stamp for monolayer selection and a stiff stamp for the prevention of roof collapse.

4.2 Future directions

4.2.1 Future fabrication of van der Waals monolayer arrays

The monolayer pattern production method presented in this work is intended to eventually enable the mass production of van der Waals heterostructures. The road to accomplishing high-yield heterostructure fabrication will require several further refinements of the method. Though not an exhaustive list, these steps include:

- Demonstrating the method with non-chalcogenide materials and with metals other than gold, establishing the versatility of the method and its viability with conducting

and insulating van der Waals materials;

- Improving the yield of the method, including through control of the exfoliation parameters;
- Scaling to sub-micron feature sizes, and mitigating the relatively larger effect of dimensional variation due to etch steps;
- Demonstrating functional devices which rely on the inter-operation of multiple transferred features.

Future implementations of the monolayer pattern production process described in Chapter 2 would benefit from automation, particularly during the exfoliation step. Presently, manual adherence of the stamp to the photoresist/patterned van der Waals bulk stack, followed by manual removal, adversely affects yield. The pressure applied to the stack is inconsistent, and the gentle pressure required to adhere the stamp to the photoresist handles without excessive deformation of the stamp is difficult to achieve. Further, the angle and rate of peeling as the stamp is removed, ideally carrying photoresist-and-gold-capped monolayers with it, are not controlled. A robust study of the influence of pressures, peeling rates, and peeling angles will be needed to access further improvements in yield and repeatability. In particular, the rate dependence of exfoliation merits study. The materials commonly used as adhesives, or stamps, are viscoelastic; their variable stiffnesses as a function of strain rate have already been shown to impact exfoliation behavior [118]. Varying the stamp stiffness in time, perhaps as the exfoliation process moves from crack initiation to crack propagation, could prove interesting. Moreover, the interplay of stamp stiffness and peel angle is, to our knowledge, as-yet uninvestigated.

The manufacturability of van der Waals heterostructures could be enhanced with improved metrology. Determination of monolayer layer boundaries from white light optical micrographs could be augmented with interference reflection microscopy (IRM). Already, initial results using IRM to observe MoS₂ monolayers, as well as both naturally-occurring and synthetic MoS₂ bilayers, show that 450 nm illumination is able to distinguish between naturally-occurring bilayers, and fabricated bilayers before annealing. This method, therefore, could be used to verify the physical coupling of van der Waals heterostructures, which implies electronic coupling [136], while simple contrast methods like those currently used could rapidly report yield metrics.

Creating new scalable exfoliation methods invites creative re-application of ideas from other fields, and despite the multiscale mechanical challenges, there is room for relatively simple solutions. For instance, the application of pressure and the exfoliation parameters (peel rate, peel angle, *etc.*) are currently uncontrolled and manually executed. As discussed in Chapter 2, roof collapse of the stamp is *not* desirable when a flexible adhesive layer is being used to exfoliate patterned van der Waals layers from bulk. However, roof collapse could be used to engineer specific peeling rates and angles, potentially with good repeatability and low cost. The entirety of the stamp face could be fixed to offsets. Pressure is applied to deflect the adhesive bottom surface of the stamp onto the photoresist

pillars; this amounts to “collapsing” the roof of the stamp. When pressure is removed, the stamp face will recoil as a function of the adhesion to the contacted surface, the viscoelastic properties of the stamp, and the height and width of the cavity. Retraction (or delamination) will proceed from the edges to the center, resulting in a peeling motion. The mathematics of roof collapse are well understood from work in microfluidics [110].

Finally, the constituent enabling technologies of the monolayer pattern production process presented in this work may prove independently valuable, once well-understood. The metal layer used to induce compression in the top van der Waals layer supports the monolayer film, resisting strain and preventing deformation or breakage of the film; this effect surely contributes to the yield numbers reported in Chapter 2, and is particularly apparent in the fact that microcracking was not observed. This role of the metal film has not been investigated in its own right, though it implies applications for metal-assisted exfoliation beyond monolayer selectivity. In particular, platinum diselenide (PtSe_2) is of interest to researchers for its potential applications in mid-infrared optoelectronics, but it is anecdotally difficult to exfoliate large regions. The layer breaks into small areas during the exfoliation process. A properly engineered metal epitaxy process could feasibly improve yield. This is particularly important as bulk production methods, like chemical vapor transport, followed by exfoliation, are currently preferable to single-layer production methods for creation of high-quality PtSe_2 monolayers [156]: high-quality few-to-monolayer films can only be isolated by an exfoliation step, which currently precludes the fabrication of large areas.

4.2.2 Further study of van der Waals material-stamp mechanics

The model described in Chapter 3 uses boundary conditions to limit the effects of shear. However, interlayer shear has been used in the production of van der Waals layers, in particular by the “Nanoimprint-Assisted Shear Exfoliation” process [8]. Shear strain in a stamp, even resulting from simple normal displacement, could feasibly be transferred to the layers. The weak interlayer bonds make layer-to-layer transfer of shear strain difficult [66]. An extended model which examines the interlayer transfer of shear strain in microscale and larger features, and its impact on layer selectivity, could yield insights that suggest new manufacturing processes. With the addition of shear, other, more brittle van der Waals materials, including PtSe_2 , could be studied; these may provide insight about tradeoffs between intra-layer and inter-layer fracture.

Future studies could use explicit finite element methods, available in ABAQUS, to probe applications of stamp viscoelasticity. The model could be extended to include unpatterned bulk, enabling the modeling of both stamp attachment processes and the stamp removal (exfoliation) processes currently studied. Combinations of interfeature spacing, stamp application pressures and strain rates, and stamp removal strain rates could be examined to uncover the mechanical design space for an optimal stamp.

Bibliography

- [1] Xiaogan Liang, Zengli Fu, and Stephen Y. Chou. Graphene Transistors Fabricated via Transfer-Printing In Device Active-Areas on Large Wafer. *Nano Letters*, 7(12):3840–3844, December 2007.
- [2] Xiaogan Liang, Valentina Giacometti, Ariel Ismach, et al. Roller-style electrostatic printing of prepatterned few-layer-graphenes. *Applied Physics Letters*, 96(1):013109, January 2010.
- [3] Xiaogan Liang, Allan S. P. Chang, Yuegang Zhang, et al. Electrostatic Force Assisted Exfoliation of Prepatterned Few-Layer Graphenes into Device Sites. *Nano Letters*, 9(1):467–472, January 2009.
- [4] Hongsuk Nam, Sungjin Wi, Hossein Rokni, et al. MoS₂ Transistors Fabricated via Plasma-Assisted Nanoprinting of Few-Layer MoS₂ Flakes into Large-Area Arrays. *ACS Nano*, 7(7):5870–5881, July 2013.
- [5] X. Liang, H. Nam, S. Wi, and M. Chen. Plasma-assisted printing and doping processes for manufacturing few-layer MoS₂-based electronic and optoelectronic devices. In *25th Annual SEMI Advanced Semiconductor Manufacturing Conference (ASMC 2014)*, pages 365–369, May 2014.
- [6] Dongsheng Li, Wolfgang Windl, and Nitin P. Padture. Toward Site-Specific Stamping of Graphene. *Advanced Materials*, 21(12):1243–1246, March 2009.
- [7] Da Li, Sungjin Wi, Mikai Chen, Byunghoon Ryu, and Xiaogan Liang. Nanoimprint-assisted shear exfoliation plus transfer printing for producing transition metal dichalcogenide heterostructures. *Journal of Vacuum Science & Technology B, Nanotechnology and Microelectronics: Materials, Processing, Measurement, and Phenomena*, 34(6):06KA01, November 2016.
- [8] Mikai Chen, Hongsuk Nam, Hossein Rokni, et al. Nanoimprint-Assisted Shear Exfoliation (NASE) for Producing Multilayer MoS₂ Structures as Field-Effect Transistor Channel Arrays. *ACS Nano*, 9(9):8773–8785, September 2015.
- [9] Gábor Zsolt Magda, János Pető, Gergely Dobrik, et al. Exfoliation of large-area transition metal chalcogenide single layers. *Scientific Reports*, 5(1), December 2015.

- [10] Hannah M. Gramling, Clarissa M. Towle, Sujay B. Desai, et al. Spatially Precise Transfer of Patterned Monolayer WS₂ and MoS₂ with Features Larger than 10⁴ μm² Directly from Multilayer Sources. *ACS Applied Electronic Materials*, 1(3):407–416, March 2019.
- [11] Sujay B. Desai, Surabhi R. Madhvapathy, Martin Amani, et al. Gold-Mediated Exfoliation of Ultralarge Optoelectronically-Perfect Monolayers. *Advanced Materials*, 28(21):4053–4058, June 2016.
- [12] Matěj Velický, Gavin E. Donnelly, William R. Hendren, et al. Mechanism of Gold-Assisted Exfoliation of Centimeter-Sized Transition-Metal Dichalcogenide Monolayers. *ACS Nano*, September 2018.
- [13] Jaewoo Shim, Sang-Hoon Bae, Wei Kong, et al. Controlled crack propagation for atomic precision handling of wafer-scale two-dimensional materials. *Science*, page eaat8126, October 2018.
- [14] B. Radisavljevic, A. Radenovic, J. Brivio, V. Giacometti, and A. Kis. Single-layer MoS₂ transistors. *Nature Nanotechnology*, 6(3):147–150, March 2011.
- [15] Melina K. Bles, Arthur W. Barnard, Peter A. Rose, et al. Graphene kirigami. *Nature*, 524(7564):204–207, August 2015.
- [16] Jonghyun Choi, Hoe Joon Kim, Michael Cai Wang, et al. Three-Dimensional Integration of Graphene via Swelling, Shrinking, and Adaptation. *Nano Letters*, 15(7):4525–4531, July 2015.
- [17] Takashi Nogi and Takahisa Kato. Influence of a Hard Surface Layer on the Limit of Elastic Contact—Part I: Analysis Using a Real Surface Model. *Journal of Tribology*, 119(3):493–500, July 1997.
- [18] R Saito, Y Tatsumi, S Huang, X Ling, and M S Dresselhaus. Raman spectroscopy of transition metal dichalcogenides. *Journal of Physics: Condensed Matter*, 28(35):353002, September 2016.
- [19] Kamal Choudhary, Gowoon Cheon, Evan Reed, and Francesca Tavazza. Elastic properties of bulk and low-dimensional materials using van der Waals density functional. *Physical Review B*, 98(1):014107, July 2018.
- [20] K. S. Novoselov, A. K. Geim, S. V. Morozov, et al. Electric Field Effect in Atomically Thin Carbon Films. *Science*, 306(5696):666–669, October 2004.
- [21] Kin Fai Mak, Changgu Lee, James Hone, Jie Shan, and Tony F. Heinz. Atomically Thin MoS₂ : A New Direct-Gap Semiconductor. *Physical Review Letters*, 105(13), September 2010.

- [22] Dinh Loc Duong, Seok Joon Yun, and Young Hee Lee. van der Waals Layered Materials: Opportunities and Challenges. *ACS Nano*, 11(12):11803–11830, December 2017.
- [23] Yunzhou Xue, Yupeng Zhang, Yan Liu, et al. Scalable Production of a Few-Layer MoS₂/WS₂ Vertical Heterojunction Array and Its Application for Photodetectors. *ACS Nano*, 10(1):573–580, January 2016.
- [24] Jorge M. García, Rui He, Mason P. Jiang, et al. Multilayer graphene grown by precipitation upon cooling of nickel on diamond. *Carbon*, 49(3):1006–1012, March 2011.
- [25] Seongjun Park. The puzzle of graphene commercialization. *Nature Reviews Materials*, 1:16085, October 2016.
- [26] Saptarshi Das, Joshua A. Robinson, Madan Dubey, Humberto Terrones, and Mauricio Terrones. Beyond Graphene: Progress in Novel Two-Dimensional Materials and van der Waals Solids. *Annual Review of Materials Research*, 45(1):1–27, 2015.
- [27] K. S. Novoselov, A. Mishchenko, A. Carvalho, and A. H. Castro Neto. 2D materials and van der Waals heterostructures. *Science*, 353(6298):aac9439, July 2016.
- [28] Yuan Liu, Nathan O. Weiss, Xidong Duan, et al. Van der Waals heterostructures and devices. *Nature Reviews Materials*, 1(9):16042, September 2016.
- [29] Yuan Cao, Valla Fatemi, Shiang Fang, et al. Unconventional superconductivity in magic-angle graphene superlattices. *Nature*, 556(7699):43–50, April 2018.
- [30] Chul-Ho Lee, Gwan-Hyoung Lee, Arend M. van der Zande, et al. Atomically thin p–n junctions with van der Waals heterointerfaces. *Nature Nanotechnology*, 9(9):676–681, September 2014.
- [31] Nicolas Mounet, Marco Gibertini, Philippe Schwaller, et al. Two-dimensional materials from high-throughput computational exfoliation of experimentally known compounds. *Nature Nanotechnology*, 13(3):246, March 2018.
- [32] Qing Tang, Zhen Zhou, and Zhongfang Chen. Innovation and discovery of graphene-like materials via density-functional theory computations. *Wiley Interdisciplinary Reviews: Computational Molecular Science*, 5(5):360–379, September 2015.
- [33] Houlong L. Zhuang, Yu Xie, P. R. C. Kent, and P. Ganesh. Computational discovery of ferromagnetic semiconducting single-layer CrSnTe₃. *Physical Review B*, 92(3):035407, July 2015.

- [34] Kirby K. H. Smithe, Chris D. English, Saurabh V. Suryavanshi, and Eric Pop. Intrinsic electrical transport and performance projections of synthetic monolayer MoS₂ devices. *2D Materials*, 4(1):011009, 2017.
- [35] Kibum Kang, Saien Xie, Lujie Huang, et al. High-mobility three-atom-thick semiconducting films with wafer-scale homogeneity. *Nature*, 520(7549):656–660, April 2015.
- [36] Young Duck Kim and James Hone. Materials science: Screen printing of 2D semiconductors. *Nature*, 544(7649):167–168, April 2017.
- [37] Stefan Wachter, Dmitry K. Polyushkin, Ole Bethge, and Thomas Mueller. A microprocessor based on a two-dimensional semiconductor. *Nature Communications*, 8:14948, April 2017.
- [38] A. K. Geim and I. V. Grigorieva. Van der Waals heterostructures. *Nature*, 499(7459):419–425, July 2013.
- [39] Yung-Chang Lin, Chun-Chieh Lu, Chao-Huei Yeh, et al. Graphene Annealing: How Clean Can It Be? *Nano Letters*, 12(1):414–419, January 2012.
- [40] Simone Bertolazzi, Jacopo Brivio, and Andras Kis. Stretching and Breaking of Ultrathin MoS₂. *ACS Nano*, 5(12):9703–9709, December 2011.
- [41] Changgu Lee, Xiaoding Wei, Jeffrey W. Kysar, and James Hone. Measurement of the Elastic Properties and Intrinsic Strength of Monolayer Graphene. *Science*, 321(5887):385–388, July 2008.
- [42] Stephen J. McDonnell and Robert M. Wallace. Atomically-thin layered films for device applications based upon 2D TMDC materials. *Thin Solid Films*, 616:482–501, October 2016.
- [43] Heung-Yeol Cho, Tri Khoa Nguyen, Farman Ullah, et al. Salt-assisted clean transfer of continuous monolayer MoS₂ film for hydrogen evolution reaction. *Physica B: Condensed Matter*, 532:84–89, March 2018.
- [44] Giovanni A. Salvatore, Niko Münzenrieder, Clément Barraud, et al. Fabrication and Transfer of Flexible Few-Layers MoS₂ Thin Film Transistors to Any Arbitrary Substrate. *ACS Nano*, 7(10):8809–8815, October 2013.
- [45] C. R. Dean, A. F. Young, I. Meric, et al. Boron nitride substrates for high-quality graphene electronics. *Nature Nanotechnology*, 5(10):722–726, October 2010.
- [46] Donglin Ma, Jianping Shi, Qingqing Ji, et al. A universal etching-free transfer of MoS₂ films for applications in photodetectors. *Nano Research*, 8(11):3662–3672, November 2015.

- [47] Xuelei Liang, Brent A. Sperling, Irene Calizo, et al. Toward Clean and Crackless Transfer of Graphene. *ACS Nano*, 5(11):9144–9153, November 2011.
- [48] Luca Banszerus, Michael Schmitz, Stephan Engels, et al. Ultrahigh-mobility graphene devices from chemical vapor deposition on reusable copper. *Science Advances*, 1(6):e1500222, July 2015.
- [49] Mingguang Chen, Dejan Stekovic, Wangxiang Li, et al. Sublimation-assisted graphene transfer technique based on small polyaromatic hydrocarbons. *Nanotechnology*, 28(25):255701, 2017.
- [50] A. Z. AlZahrani. First-principles study on the structural and electronic properties of graphene upon benzene and naphthalene adsorption. *Applied Surface Science*, 257(3):807–810, November 2010.
- [51] Atsushi Matsumoto, Keisuke Jono, Munetaka Akita, and Michito Yoshizawa. Side-Chain-Directed Dispersion of MoS₂ Nanosheets by V-Shaped Polyaromatic Compounds. *Chemistry – An Asian Journal*, 12(22):2889–2893, 2017.
- [52] Haydn T. Mitchell, Merry K. Smith, Nicholas D. Belloch, Douglas W. Van Citters, and Katherine A. Mirica. Polycyclic Aromatic Hydrocarbons as Sublimable Adhesives. *Chemistry of Materials*, 29(7):2788–2793, April 2017.
- [53] Sugkyun Cha, Minjeong Cha, Seojun Lee, Jin Hyoun Kang, and Changsoon Kim. Low-Temperature, Dry Transfer-Printing of a Patterned Graphene Monolayer. *Scientific Reports*, 5(1), November 2016.
- [54] Jing Zhao, Hua Yu, Wei Chen, et al. Patterned Peeling 2D MoS₂ off the Substrate. *ACS Applied Materials & Interfaces*, 8(26):16546–16550, July 2016.
- [55] T. Björkman, A. Gulans, A. V. Krasheninnikov, and R. M. Nieminen. van der Waals Bonding in Layered Compounds from Advanced Density-Functional First-Principles Calculations. *Physical Review Letters*, 108(23):235502, June 2012.
- [56] Jorge Torres, Yisi Zhu, Pei Liu, Seong Chu Lim, and Minhee Yun. Adhesion Energies of 2D Graphene and MoS₂ to Silicon and Metal Substrates. *physica status solidi (a)*, 215(1):1700512, January 2018.
- [57] Xuezhi Ma, Qiushi Liu, Da Xu, et al. Capillary-Force-Assisted Clean-Stamp Transfer of Two-Dimensional Materials. *Nano Letters*, 17(11):6961–6967, November 2017.
- [58] Robert G. Parr. Density Functional Theory of Atoms and Molecules. In Kenichi Fukui and Bernard Pullman, editors, *Horizons of Quantum Chemistry*, Académie Internationale Des Sciences Moléculaires Quantiques / International Academy of Quantum Molecular Science, pages 5–15. Springer Netherlands, 1980.

- [59] Chun-Hu Chen, Kongara M Reddy, and Nitin P Padture. Site-specific stamping of graphene micro-patterns over large areas using flexible stamps. *Nanotechnology*, 23(23):235603, June 2012.
- [60] Anton N. Sidorov, Mehdi M. Yazdanpanah, Romaneh Jalilian, et al. Electrostatic deposition of graphene. *Nanotechnology*, 18(13):135301, 2007.
- [61] Mikai Chen, Hossein Rokni, Wei Lu, and Xiaogan Liang. Scaling behavior of nanoimprint and nanoprinting lithography for producing nanostructures of molybdenum disulfide. *Microsystems & Nanoengineering*, 3:17053, September 2017.
- [62] Yuan Huang, Eli Sutter, Norman N. Shi, et al. Reliable Exfoliation of Large-Area High-Quality Flakes of Graphene and Other Two-Dimensional Materials. *ACS Nano*, 9(11):10612–10620, November 2015.
- [63] Lin Yuan, Jun Ge, Xianglin Peng, et al. A reliable way of mechanical exfoliation of large scale two dimensional materials with high quality. *AIP Advances*, 6(12):125201, December 2016.
- [64] Li Song, Lijie Ci, Wei Gao, and Pulickel M. Ajayan. Transfer Printing of Graphene Using Gold Film. *ACS Nano*, 3(6):1353–1356, June 2009.
- [65] Yuzhi Zhou, Daisuke Kiriya, E. E. Haller, et al. Compliant substrate epitaxy: Au on MoS₂. *Physical Review B*, 93(5):054106, February 2016.
- [66] Haoye Sun, Eric W. Sirott, James Mastandrea, et al. Theory of thin-film-mediated exfoliation of van der Waals bonded layered materials. *Physical Review Materials*, 2(9):094004, September 2018.
- [67] Benjamin J. Carey, Jian Zhen Ou, Rhiannon M. Clark, et al. Wafer-scale two-dimensional semiconductors from printed oxide skin of liquid metals. *Nature Communications*, 8:14482, February 2017.
- [68] Paul Z. Hanakata, Zenan Qi, David K. Campbell, and Harold S. Park. Highly stretchable MoS₂ kirigami. *Nanoscale*, 8(1):458–463, 2016.
- [69] Tongwei Han, Fabrizio Scarpa, and Neil L. Allan. Super stretchable hexagonal boron nitride Kirigami. *Thin Solid Films*, 632:35–43, June 2017.
- [70] Bohayra Mortazavi, Aurélien Lherbier, Zheyong Fan, et al. Thermal and electronic transport characteristics of highly stretchable graphene kirigami. *Nanoscale*, 9(42):16329–16341, 2017.
- [71] Yushun Zhao, Chao Wang, Jianyang Wu, et al. Carbon nanotubes kirigami mechanical metamaterials. *Physical Chemistry Chemical Physics*, 19(18):11032–11042, May 2017.

- [72] Paul Z. Hanakata, Ekin D. Cubuk, David K. Campbell, and Harold S. Park. Accelerated Search and Design of Stretchable Graphene Kirigami Using Machine Learning. *Physical Review Letters*, 121(25):255304, December 2018.
- [73] Zhao Qin, Gang Seob Jung, Min Jeong Kang, and Markus J. Buehler. The mechanics and design of a lightweight three-dimensional graphene assembly. *Science Advances*, 3(1):e1601536, January 2017.
- [74] James Annett and Graham L. W. Cross. Self-assembly of graphene ribbons by spontaneous self-tearing and peeling from a substrate. *Nature*, 535(7611):271–275, July 2016.
- [75] Z. Guguchia, A. Kerelsky, D. Edelberg, et al. Magnetism in Semiconducting Molybdenum Dichalcogenides. November 2017.
- [76] Jonghyun Choi, Jihun Mun, Michael Cai Wang, et al. Hierarchical, Dual-Scale Structures of Atomically Thin MoS₂ for Tunable Wetting. *Nano Letters*, 17(3):1756–1761, March 2017.
- [77] Siwei Luo, Guolin Hao, Yiping Fan, et al. Formation of ripples in atomically thin MoS₂ and local strain engineering of electrostatic properties. *Nanotechnology*, 26(10):105705, 2015.
- [78] Michael Cai Wang, SungGyu Chun, Ryan Steven Han, et al. Heterogeneous, Three-Dimensional Texturing of Graphene. *Nano Letters*, 15(3):1829–1835, March 2015.
- [79] Jannik C. Meyer, A. K. Geim, M. I. Katsnelson, et al. The structure of suspended graphene sheets. *Nature*, 446(7131):60–63, March 2007.
- [80] A. Fasolino, J. H. Los, and M. I. Katsnelson. Intrinsic ripples in graphene. *Nature Materials*, 6(11):858–861, November 2007.
- [81] Hongwei Bao, Yuhong Huang, Zhi Yang, et al. Tensile loading induced phase transition and rippling in single-layer MoS₂. *Applied Surface Science*, 404:180–187, May 2017.
- [82] Minsu Kim, Pilgyu Kang, Juyoung Leem, and SungWoo Nam. A stretchable crumpled graphene photodetector with plasmonically enhanced photoresponsivity. *Nanoscale*, 9(12):4058–4065, March 2017.
- [83] Christian Martella, Carlo Mennucci, Eugenio Cinquanta, et al. Anisotropic MoS₂ Nanosheets Grown on Self-Organized Nanopatterned Substrates. *Advanced Materials*, 29(19), May 2017.

- [84] Jorge Quereda, Pablo San-Jose, Vincenzo Parente, et al. Strong Modulation of Optical Properties in Black Phosphorus through Strain-Engineered Rippling. *Nano Letters*, 16(5):2931–2937, May 2016.
- [85] F. K. Perkins, A. L. Friedman, E. Cobas, et al. Chemical Vapor Sensing with Monolayer MoS₂. *Nano Letters*, 13(2):668–673, February 2013.
- [86] Andrey A. Kistanov, Yongqing Cai, Kun Zhou, Sergey V. Dmitriev, and Yong-Wei Zhang. Large Electronic Anisotropy and Enhanced Chemical Activity of Highly Rippled Phosphorene. *The Journal of Physical Chemistry C*, 120(12):6876–6884, March 2016.
- [87] Jiang-Bin Wu, Huan Zhao, Yuanrui Li, et al. Monolayer Molybdenum Disulfide Nanoribbons with High Optical Anisotropy. *Advanced Optical Materials*, 4(5):756–762, 2016.
- [88] Michael G. Stanford, Philip D. Rack, and Deep Jariwala. Emerging nanofabrication and quantum confinement techniques for 2D materials beyond graphene. *npj 2D Materials and Applications*, 2(1):20, July 2018.
- [89] Swapnil Chandratre and Pradeep Sharma. Coaxing graphene to be piezoelectric. *Applied Physics Letters*, 100(2):023114, January 2012.
- [90] Hanyu Zhu, Yuan Wang, Jun Xiao, et al. Observation of piezoelectricity in free-standing monolayer MoS₂. *Nature Nanotechnology*, 10(2):151–155, February 2015.
- [91] Toby Hallam, Amir Shakouri, Emanuele Poliani, et al. Controlled Folding of Graphene: GraFold Printing. *Nano Letters*, 15(2):857–863, February 2015.
- [92] Gertjan S. Verhoeven, Martin Dienwiebel, and Joost W. M. Frenken. Model calculations of superlubricity of graphite. *Physical Review B*, 70(16):165418, October 2004.
- [93] He Li, Jinhuan Wang, Song Gao, et al. Superlubricity between MoS₂ Monolayers. *Advanced Materials*, 29(27):1701474, July 2017.
- [94] Jiarui Yang, Ze Liu, Francois Grey, et al. Observation of High-Speed Microscale Superlubricity in Graphite. *Physical Review Letters*, 110(25):255504, June 2013.
- [95] Hua Yu, Zhengzhong Yang, Luojun Du, et al. Precisely Aligned Monolayer MoS₂ Epitaxially Grown on h-BN basal Plane. *Small*, 13(7):1603005, February 2017.
- [96] Yumeng Shi, Wu Zhou, Ang-Yu Lu, et al. van der Waals Epitaxy of MoS₂ Layers Using Graphene As Growth Templates. *Nano Letters*, 12(6):2784–2791, June 2012.

- [97] Deyi Fu, Xiaoxu Zhao, Yu-Yang Zhang, et al. Molecular Beam Epitaxy of Highly Crystalline Monolayer Molybdenum Disulfide on Hexagonal Boron Nitride. *Journal of the American Chemical Society*, 139(27):9392–9400, July 2017.
- [98] Mervin Zhao, Yu Ye, Yimo Han, et al. Large-scale chemical assembly of atomically thin transistors and circuits. *Nature Nanotechnology*, 11(11):954–959, November 2016.
- [99] Abraham Ulman. Formation and Structure of Self-Assembled Monolayers. *Chemical Reviews*, 96(4):1533–1554, January 1996.
- [100] Hannu Häkkinen. The gold–sulfur interface at the nanoscale. *Nature Chemistry*, 4(6):443–455, June 2012.
- [101] Daisuke Kiriya, Yuzhi Zhou, Christopher Nelson, et al. Oriented Growth of Gold Nanowires on MoS₂. *Advanced Functional Materials*, 25(39):6257–6264, October 2015.
- [102] Emily E. Hoffman and Laurence D. Marks. Soft Interface Fracture Transfer in Nanoscale MoS₂. *Tribology Letters*, 64(1):16, September 2016.
- [103] Jiantong Li, Mikael Östling, Jiantong Li, and Mikael Östling. Scalable Fabrication of 2D Semiconducting Crystals for Future Electronics. *Electronics*, 4(4):1033–1061, December 2015.
- [104] Xi Ling, Yuxuan Lin, Qiong Ma, et al. Parallel Stitching of 2D Materials. *Advanced Materials*, 28(12):2322–2329, March 2016.
- [105] Gwan-Hyoung Lee, Young-Jun Yu, Xu Cui, et al. Flexible and Transparent MoS₂ Field-Effect Transistors on Hexagonal Boron Nitride-Graphene Heterostructures. *ACS Nano*, 7(9):7931–7936, September 2013.
- [106] Hongsuk Nam, Sungjin Wi, Hossein Rokni, et al. MoS₂ Transistors Fabricated via Plasma-Assisted Nanoprinting of Few-Layer MoS₂ Flakes into Large-Area Arrays. *ACS Nano*, 7(7):5870–5881, July 2013.
- [107] Seung Ryul Na, Ji Won Suk, Li Tao, et al. Selective Mechanical Transfer of Graphene from Seed Copper Foil Using Rate Effects. *ACS Nano*, 9(2):1325–1335, February 2015.
- [108] Andrea Splendiani, Liang Sun, Yuanbo Zhang, et al. Emerging Photoluminescence in Monolayer MoS₂. *Nano Letters*, 10(4):1271–1275, April 2010.
- [109] C. Y. Hui, A. Jagota, Y. Y. Lin, and E. J. Kramer. Constraints on Microcontact Printing Imposed by Stamp Deformation. *Langmuir*, 18(4):1394–1407, February 2002.

- [110] Yonggang Y. Huang, Weixing Zhou, K. J. Hsia, et al. Stamp Collapse in Soft Lithography. *Langmuir*, 21(17):8058–8068, August 2005.
- [111] Emmanuel Delamarche, Heinz Schmid, Bruno Michel, and Hans Biebuyck. Stability of molded polydimethylsiloxane microstructures. *Advanced Materials*, 9(9):741–746, January 1997.
- [112] N. I. Muskhelishvili. *Some Basic Problems of the Mathematical Theory of Elasticity*. Springer Netherlands, 1977.
- [113] Hayden Taylor, Duane Boning, Ciprian Iliescu, and Bangtao Chen. Computationally efficient modelling of pattern dependencies in the micro-embossing of thermoplastic polymers. *Microelectronic Engineering*, 85(5):1453–1456, May 2008.
- [114] Kenneth Langstreth Johnson, Kevin Kendall, and A. D. Roberts. Surface energy and the contact of elastic solids. *Proc. R. Soc. Lond. A*, 324(1558):301–313, September 1971.
- [115] Kazuki Soejima, Takamasa Hirayama, Daisuke Shimokawa, Masaaki Sato, and Yukio Arimitsu. Heat-peelable pressure-sensitive adhesive sheet for cutting laminated ceramic sheet and method for cut-processing laminated ceramic sheet, September 2013.
- [116] W. C. Oliver and G. M. Pharr. An improved technique for determining hardness and elastic modulus using load and displacement sensing indentation experiments. *Journal of Materials Research*, 7(6):1564–1583, June 1992.
- [117] Min Hwan Jeon, Chisung Ahn, HyeongU Kim, et al. Controlled MoS₂ layer etching using CF₄ plasma. *Nanotechnology*, 26(35):355706, 2015.
- [118] Andres Castellanos-Gomez, Michele Buscema, Rianda Molenaar, et al. Deterministic transfer of two-dimensional materials by all-dry viscoelastic stamping. *2D Materials*, 1(1):011002, 2014.
- [119] A Castellanos-Gomez, N Agraït, and G Rubio-Bollinger. Optical identification of atomically thin dichalcogenide crystals. *Applied Physics Letters*, 96(21):213116, May 2010.
- [120] Hai Li, Jumiati Wu, Xiao Huang, et al. Rapid and Reliable Thickness Identification of Two-Dimensional Nanosheets Using Optical Microscopy. *ACS Nano*, 7(11):10344–10353, November 2013.
- [121] Julia Gusakova, Xingli Wang, Li Lynn Shiau, et al. Electronic Properties of Bulk and Monolayer TMDs: Theoretical Study Within DFT Framework (GVJ-2e Method). *physica status solidi (a)*, 214(12):1700218, December 2017.

- [122] Bo Liu, Weijie Zhao, Zijing Ding, et al. Engineering Bandgaps of Monolayer MoS₂ and WS₂ on Fluoropolymer Substrates by Electrostatically Tuned Many-Body Effects. *Advanced Materials*, 28(30):6457–6464, August 2016.
- [123] Hiram J. Conley, Bin Wang, Jed I. Ziegler, et al. Bandgap Engineering of Strained Monolayer and Bilayer MoS₂. *Nano Letters*, 13(8):3626–3630, August 2013.
- [124] Martin Amani, Der-Hsien Lien, Daisuke Kiriya, et al. Near-unity photoluminescence quantum yield in MoS₂. *Science*, 350(6264):1065–1068, November 2015.
- [125] Scott E. Thompson and Srivatsan Parthasarathy. Moore’s law: the future of Si microelectronics. *Materials Today*, 9(6):20–25, June 2006.
- [126] Meikei Jeong, Bruce Doris, Jakub Kedzierski, Ken Rim, and Min Yang. Silicon Device Scaling to the Sub-10-nm Regime. *Science*, 306(5704):2057–2060, December 2004.
- [127] Mohammed Bouhassoune and Arno Schindlmayr. Electronic structure and effective masses in strained silicon. *Physica Status Solidi (c)*, 7(2):460–463, February 2010.
- [128] Darshana Wickramaratne, Ferdows Zahid, and Roger K. Lake. Electronic and thermoelectric properties of few-layer transition metal dichalcogenides. *The Journal of Chemical Physics*, 140(12):124710, March 2014.
- [129] Sujay B. Desai, Surabhi R. Madhvapathy, Angada B. Sachid, et al. MoS₂ transistors with 1-nanometer gate lengths. *Science*, 354(6308):99–102, October 2016.
- [130] Kapildeb Dolui, Ivan Rungger, and Stefano Sanvito. Origin of the *n*-type and *p*-type conductivity of MoS₂ monolayers on a SiO₂ substrate. *Physical Review B*, 87(16):165402, April 2013.
- [131] Namphung Peimyoo, Jingzhi Shang, Chunxiao Cong, et al. Nonblinking, Intense Two-Dimensional Light Emitter: Monolayer WS₂ Triangles. *ACS Nano*, 7(12):10985–10994, December 2013.
- [132] Hui Fang, Steven Chuang, Ting Chia Chang, et al. High-Performance Single Layered WSe₂ *p*-FETs with Chemically Doped Contacts. *Nano Letters*, 12(7):3788–3792, July 2012.
- [133] MATLAB Image Processing Toolbox, 2017.
- [134] Meenakshi Annamalai, Kalon Gopinadhan, Sang A. Han, et al. Surface energy and wettability of van der Waals structures. *Nanoscale*, 8(10):5764–5770, March 2016.
- [135] Tery L. Barr and Sudipta Seal. Nature of the use of adventitious carbon as a binding energy standard. *Journal of Vacuum Science & Technology A*, 13(3):1239–1246, May 1995.

- [136] Kaihui Liu, Liming Zhang, Ting Cao, et al. Evolution of interlayer coupling in twisted molybdenum disulfide bilayers. *Nature Communications*, 5:4966, September 2014.
- [137] Jeehwan Kim, Hongsik Park, James B. Hannon, et al. Layer-Resolved Graphene Transfer via Engineered Strain Layers. *Science*, 342(6160):833–836, November 2013.
- [138] Yunjo Kim, Samuel S. Cruz, Kyusang Lee, et al. Remote epitaxy through graphene enables two-dimensional material-based layer transfer. *Nature*, 544(7650):340–343, April 2017.
- [139] Steve Plimpton. Fast Parallel Algorithms for Short-Range Molecular Dynamics. *Journal of Computational Physics*, 117(1):1–19, March 1995.
- [140] Sung-San Cho and Seungho Park. Finite element modeling of adhesive contact using molecular potential. *Tribology International*, 37(9):763–769, September 2004.
- [141] Eleir M. Bortoleto, Erika F. Prados, Vanessa Seriacopi, et al. Numerical modeling of adhesion and adhesive failure during unidirectional contact between metallic surfaces. *Friction*, 4(3):217–227, September 2016.
- [142] B. Liu, Y. Huang, H. Jiang, S. Qu, and K. C. Hwang. The atomic-scale finite element method. *Computer Methods in Applied Mechanics and Engineering*, 193(17):1849–1864, May 2004.
- [143] Antonio Pantano, David M. Parks, and Mary C. Boyce. Mechanics of deformation of single- and multi-wall carbon nanotubes. *Journal of the Mechanics and Physics of Solids*, 52(4):789–821, April 2004.
- [144] Yuye Tang, Guoxin Cao, Xi Chen, et al. A Finite Element Framework for Studying the Mechanical Response of Macromolecules: Application to the Gating of the Mechanosensitive Channel MscL. *Biophysical Journal*, 91(4):1248–1263, August 2006.
- [145] André A. R. Wilmes and Silvestre T. Pinho. A coupled mechanical-charge/dipole molecular dynamics finite element method, with multi-scale applications to the design of graphene nano-devices. *International Journal for Numerical Methods in Engineering*, 100(4):243–276, 2014.
- [146] Jones J. E. and Chapman Sydney. On the determination of molecular fields. —II. From the equation of state of a gas. *Proceedings of the Royal Society of London. Series A, Containing Papers of a Mathematical and Physical Character*, 106(738):463–477, October 1924.

- [147] Tao Liang, Simon R. Phillpot, and Susan B. Sinnott. Parametrization of a reactive many-body potential for Mo–S systems. *Physical Review B*, 79(24):245110, June 2009.
- [148] Jin-Wu Jiang, Harold S. Park, and Timon Rabczuk. Molecular dynamics simulations of single-layer molybdenum disulphide (MoS_2): Stillinger-Weber parametrization, mechanical properties, and thermal conductivity. *Journal of Applied Physics*, 114(6):064307, August 2013.
- [149] A. K. Rappe, C. J. Casewit, K. S. Colwell, W. A. Goddard, and W. M. Skiff. UFF, a full periodic table force field for molecular mechanics and molecular dynamics simulations. *Journal of the American Chemical Society*, 114(25):10024–10035, December 1992.
- [150] F. Scarpa, S. Adhikari, and A. Srikantha Phani. Effective elastic mechanical properties of single layer graphene sheets. *Nanotechnology*, 20(6):065709, January 2009.
- [151] Y. Huang, J. Wu, and K. C. Hwang. Thickness of graphene and single-wall carbon nanotubes. *Physical Review B*, 74(24):245413, December 2006.
- [152] C. Q. Ru. Effect of van der Waals forces on axial buckling of a double-walled carbon nanotube. *Journal of Applied Physics*, 87(10):7227–7231, April 2000.
- [153] Jae-Ung Lee, Sungjong Woo, Jaesung Park, et al. Strain-shear coupling in bilayer MoS_2 . *Nature Communications*, 8(1):1370, November 2017.
- [154] K. Komvopoulos. Finite Element Analysis of a Layered Elastic Solid in Normal Contact With a Rigid Surface. *Journal of Tribology*, 110(3):477–485, July 1988.
- [155] Qing Peng and Suvranu De. Outstanding mechanical properties of monolayer MoS_2 and its application in elastic energy storage. *Physical Chemistry Chemical Physics*, 15(44):19427–19437, 2013.
- [156] Xuechao Yu, Peng Yu, Di Wu, et al. Atomically thin noble metal dichalcogenide: a broadband mid-infrared semiconductor. *Nature Communications*, 9(1):1545, April 2018.

Appendix A

Derivation of van der Waals body force

Following the work of Israelachvili¹, we ignore the repulsive component of the Lennard-Jones potential. For a single interatomic interaction, the energy can be expressed as

$$w(r) = \frac{-C}{r^n} \quad (\text{A.1})$$

where r is the interatomic distance, n is an exponent chosen based on the model used to capture the interatomic behavior, and C is a constant specific to the given atomic or molecular pair. In a Lennard-Jones parameterization of a van der Waals interaction, the attractive component of the interatomic energy is written as

$$U(r) = 4\varepsilon \left[- \left(\frac{\sigma}{r} \right)^6 \right] \quad (\text{A.2})$$

where ε and σ are constants specific to the pairing. Thus $C = 4\varepsilon\sigma^6$, and $n = 6$. The energy of a single particle (atom or molecular) interacting with a semi-infinite planar body whose surface is at distance D from the particle is then written as

$$w(D) = \frac{-\pi C \rho}{6D^3} \quad (\text{A.3})$$

where ρ is the density of atoms in the semi-infinite planar body. The body force, then, is

$$F(D) = \frac{\pi C \rho}{2D^4} \quad (\text{A.4})$$

¹J. Israelachvili, *Intermolecular and Surface Forces*, 3rd ed. San Diego: Elsevier Academic Press, 2011, pp. 205-222.